5-2017

High-Throughput Functional System for Encapsulated Networks of Model Cell Membranes

Mary-Anne Kim Anh Nguyen
University of Tennessee, Knoxville, mnguyen8@vols.utk.edu

To the Graduate Council:

I am submitting herewith a dissertation written by Mary-Anne Kim Anh Nguyen entitled "High-Throughput Functional System for Encapsulated Networks of Model Cell Membranes." I have examined the final electronic copy of this dissertation for form and content and recommend that it be accepted in partial fulfillment of the requirements for the degree of Doctor of Philosophy, with a major in Biomedical Engineering.

Stephen A. Sarles, Major Professor

We have read this dissertation and recommend its acceptance:

C. Patrick Collier, Scott Lenaghan, Paul Dalhaimer, Eric Freeman

Accepted for the Council:

Dixie L. Thompson

Vice Provost and Dean of the Graduate School

(Original signatures are on file with official student records.)

High-Throughput Functional System for Encapsulated Networks of Model Cell Membranes

A Dissertation Presented for the
Doctor of Philosophy
Degree
The University of Tennessee, Knoxville

Mary-Anne Kim Anh Nguyen
May 2017

DEDICATION

To my parents

Tai and Yen Nguyen

my two sisters and brother

Mary, Jasmine, and Paul

and my fiancé

Steven Powell

ACKNOWLEDGEMENTS

First and foremost, thank you to my advisor and mentor, Andy Sarles. None of this would be possible without his guidance, expertise, and patience. Andy has positively influence my life in the lab and personally. He has helped me grow to be a better researcher by improving my writing skills and public speaking, pushing me to think out side the box, and constantly stay up to date on literature. I am forever grateful for the opportunities and mentorship Andy has given me.

I also want to thank my current and former labmates and colleagues, Graham Taylor, Guru Venkatesan, and Nima Tamaddoni. They welcomed me into the lab and have since become my lifetime friends. To my fellow women engineers, Tayler Schimel and Emily Morin, thanks for being there for me throughout this journey.

The work describe herein would not be possible without the advice and assistance from several key individuals. I want to acknowledge Pat Collier, Scott Lenaghan, Eric Freeman, Paul Dalhaimer, Scott Retterer, and Bernadeta Srijanto for their support. Thanks to Air Force Office of Scientific Research (AFOSR) Basic Research Initiative Grant number FA9550-12-1-0464 for financial support. Also, thanks to the Center for Nanophase Materials Sciences, which is a DOE Office of Science User Facility where all the device fabrication was conducted.

ABSTRACT

Synthetic lipid bilayers provide models of cell membranes to study biomolecular interactions and signal transduction. The droplet interface bilayer (DIB) is a highly versatile technique for assembling planar lipid membranes between water droplets in oil. The DIB method thus provides a unique capability for developing digital, droplet-based membrane platforms for rapid membrane characterization, drug screening and ion channel recordings. In this work, a new microfluidic system is presented that automates droplet generation, sorting, and sequential trapping in designated locations to enable rapid assembly of arrays of DIBs along with *in situ* electrical measurements. This platform provides repeatable processes for forming long-lasting bilayer arrays for numerous membrane-based applications. Studies on asymmetric lipid membranes are performed to understanding the effects of peptides on the disruption of asymmetric lipid membranes and intramembrane potential. In addition, an automated microfluidic array is applied to isolate and transform single cells to improve the ability to study gene transformation on an individual cell basis, with greater spatial and temporal resolution of each cell's response.

TABLE OF CONTENTS

LIST OF TABLES

LIST OF FIGURES

CHAPTER 1
INTRODUCTION AND LITERATURE REVIEW

The overarching goal of this work is to develop a high throughput microfluidic system in order to investigate numerous basic lipid bilayer studies and membrane-mediated processes with greater efficiency and statistical significance. With a high-throughput system, we can gain a better understanding of mechanisms governing biological functions leading to new insight to aide in membrane based applications such as studies of basic membrane characterization, membrane-mediated processes, ion channel recordings, and rapid drug screening assays. Not only can this platform be applied to synthetic systems, studies utilizing live cells can benefit as well. This dissertation presents a step towards developing an automated high-throughput droplet generation and arrangement system to create an array of DIBs or cells, which can be electrically interrogated, in an enclosed substrate.

This chapter begins with a description of cell membranes followed by methods to form and characterize synthetic models of cell membranes. Topics of microfluidics and lipid asymmetry are also discussed. From the literature review, gaps and goals are defined for the work presented in this dissertation.

1.1 Cell membrane

The cell membrane is a biological bilayer that works as a fluid barrier in all cells, separating the interior of the cell from the extracellular matrix [1, 2]. Proteins [3], enzymes [4], cholesterols [5], and ions transfer [6, 7], across the membrane help the intracellular matrix to communicate with the extracellular matrix. The key components of these semipermeable membranes are phospholipids. As shown in Figure 1, the phospholipid structure contains a polar hydrophilic (i.e., water-seeking) head group and a hydrophobic (water-repelling) tail group [8]. Lipid

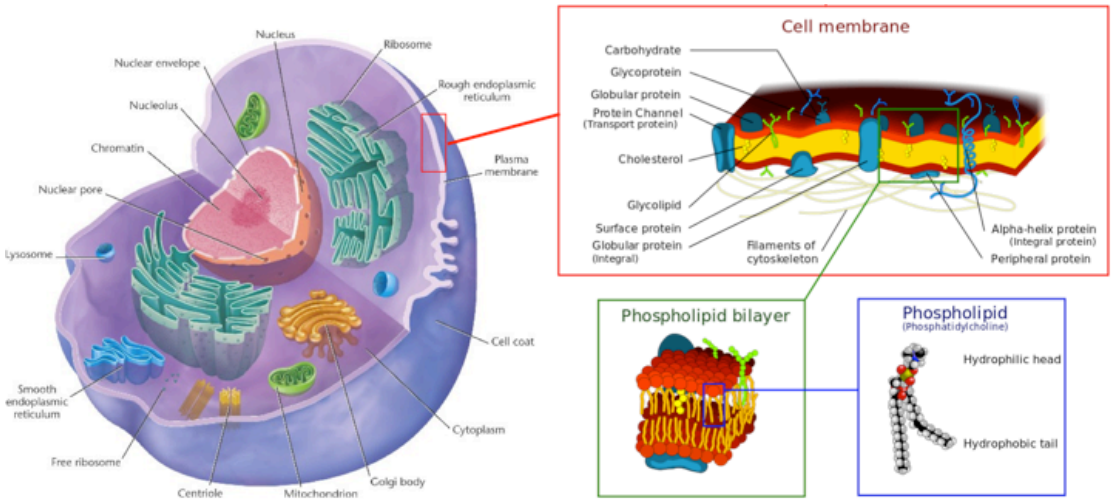

Figure 1. Cell membrane acts as a barrier separating the interior of the cell from the extracellular matrix. The key components of these semipermeable membranes are phospholipids. Reproduced from [2].

bilayers form through the self-assembly of lipids, amphiphilic molecules with hydrophilic and hydrophobic regions, placed in aqueous environments.

Membrane proteins are often found inserted into or through the hydrophobic core of membranes in cells, and these membrane proteins perform specific microscopic functions that affect overarching macroscopic physiological functions. Membrane proteins can be generally grouped into two categories: integral proteins span the entire thickness of the lipid bilayer while peripheral proteins are primarily associated with either an inserted integral membrane protein or the polar headgroup region of only one leaflet of the bilayer [9]. The bilayer-like amphiphilicity of certain proteins drive or maintain protein positioning relative to the membrane (note: protein amphiphilicity is affected by the polarity of the amino acid chain sidegroups positioned along the length of the peptide). Membrane proteins often perform tasks or functions [10]. For instance, transporter membrane proteins perform roles in moving soluble and insoluble species across the membrane. Examples include ion pumps, ion channels, and even transporters of larger molecules like sugar molecules, nucleic acids, or lipid

headgroups [10]. Ion pumps actively expend energy to pump ions across the membrane while channels act as passive pores that allow the passage of solutes through the membrane. It should be noted that some channels form constantly open static pores while others only form pores in the presence of sufficient electrical potential (“voltage-gated”), mechanical strain (“mechanosensitive”), or the appropriate soluble ligands (“ligand gated”). Floppases and flippases, other examples of transport proteins, are integral membrane proteins that aide in transporting the polar headgroups of lipids from one side of the membrane to the other in order to help maintain desired lipid composition asymmetry [9].

A number of studies have investigated the electrical [11, 12], and mechanical [13] properties of cell membranes; however, the complexity of natural membranes and the fact that they may contain multiple membrane proteins and various types of lipids makes them difficult to work with and to characterize them in detail; the techniques required to investigate natural membranes are also labor-intensive and time consuming. To overcome these challenges, many researchers have taken up the study of synthetic lipid bilayers, investigating a wide range of phenomena, including protein insertion [14, 15] and the permeability of cell membrane [16-18]. To study the cell membrane, synthetic lipid bilayers that mimic natural cell membrane structures are formed in-vitro [19-21] to be able to study the characteristics of these membranes.

1.2 Droplet interface bilayer as model cell membranes

Given the importance and significance of membranes to greater physiological function, there are benefits of technologies that allow assembly and creation of model membranes that mimic the composition, organization, and function of natural membranes. A means of constructing and accessing physical model membranes could provide the ability to study membrane and membrane- protein mediated processes to improve our understanding of membrane related biological and biophysical processes. There are various methods for forming

these synthetic bilayers that have been developed. This included lipid vesicles [22, 23], black lipid membranes (BLM) [24], supported lipid bilayers (SLB) [25, 26], tethered bilayer lipid membranes (t-BLM) [27], and droplet interface bilayers (DIBs) [20], which the technique used in the research presented herein.

The droplet interface bilayer (DIB) is highly versatile technique for constructing model cell membranes (i.e. lipid bilayers) between lipid-coated water droplets in oil (Figure 2) [20, 28, 29]. The dissolved lipids begin to self-assemble at the oil-water interface surrounding an aqueous droplet placed into oil, and the droplets can be brought together after only a few minutes without coalescing and becoming one single droplet. Instead, the opposing monolayers on two adjacent droplets will spontaneously fuse and form a bimolecular layer of lipids due to a reduction in free energy of the system and the entropy driven exclusion of solvent from the otherwise constraining acyl chains of the newly formed bilayer [30]. The resulting interfacial film is stabilized by a balance of intermolecular forces (van der Waals, electrostatic, and steric interactions) [31]. As a result in spontaneous adhesion allow the system to reduce the total free energy and the reduction of free energy of the system can be shown in equation below:

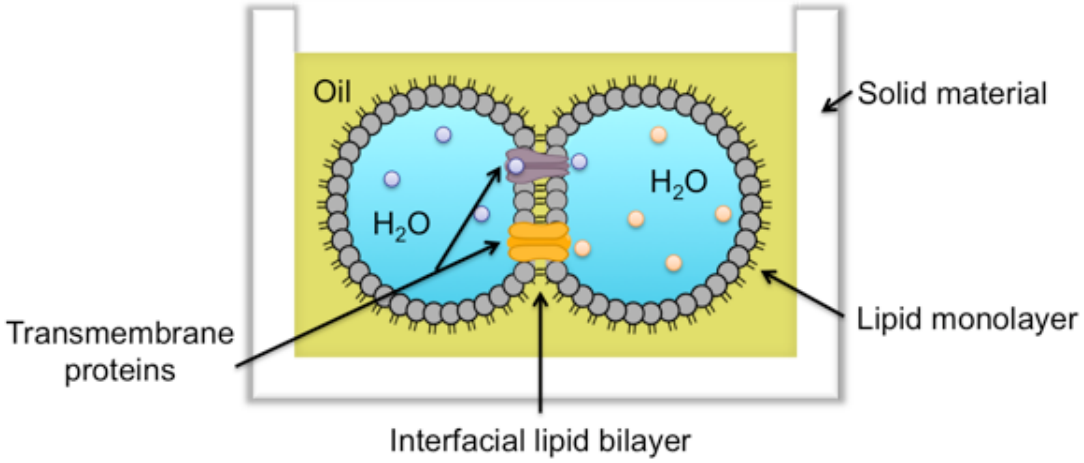

Figure 2. Side schematic of a droplet interface bilayer.

$$\Delta F = 2\gamma_m(\cos\theta - 1) \quad (1)$$

where the γ_m is the monolayer tension and θ is the contact angle of adhered droplets (Figure 3). The resulting ~3-5 nm thick lipid bilayer [32, 33] is an experimentally accessible model for cell membranes. Importantly, DIBs are formed quickly, easily, and are durable.

Methods for DIB formation provide the ability to control symmetry of biomolecules, salt concentration, pH, or other factors included on each side of the lipid bilayer [34]. DIB assemblies provide a suitable environment for studying many aspects of membrane transport including antimicrobial peptide or pore-forming protein insertion and gating [20, 29, 35]. DIB systems have also been employed recently to use biomolecular functionality for sensing [36-38], actuation [39], and energy conversion [40, 41] applications. Figure 4 shows a few examples of studies that utilize DIBs including studies on membrane properties and protein activation, and development of hair cell sensors.

Bioinspired material systems utilize principles and functionalities found in nature to benefit the development of engineered systems. In recent years, the use of biological molecules such as phospholipids, transmembrane proteins, and ion channels have contributed to the development of new types of membrane-based

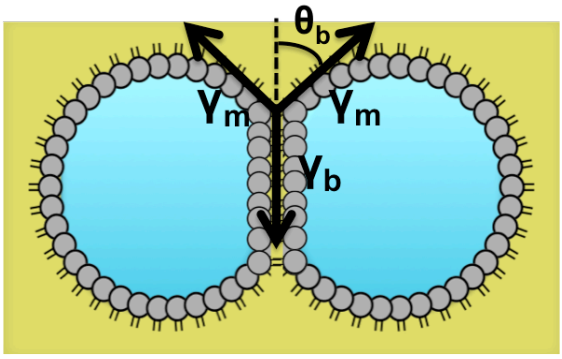

Figure 3. DIB systems are stabilized by tensions of the monolayer, γ_m, and the bilayer, γ_b. θb is the contact angle of adhered droplets.

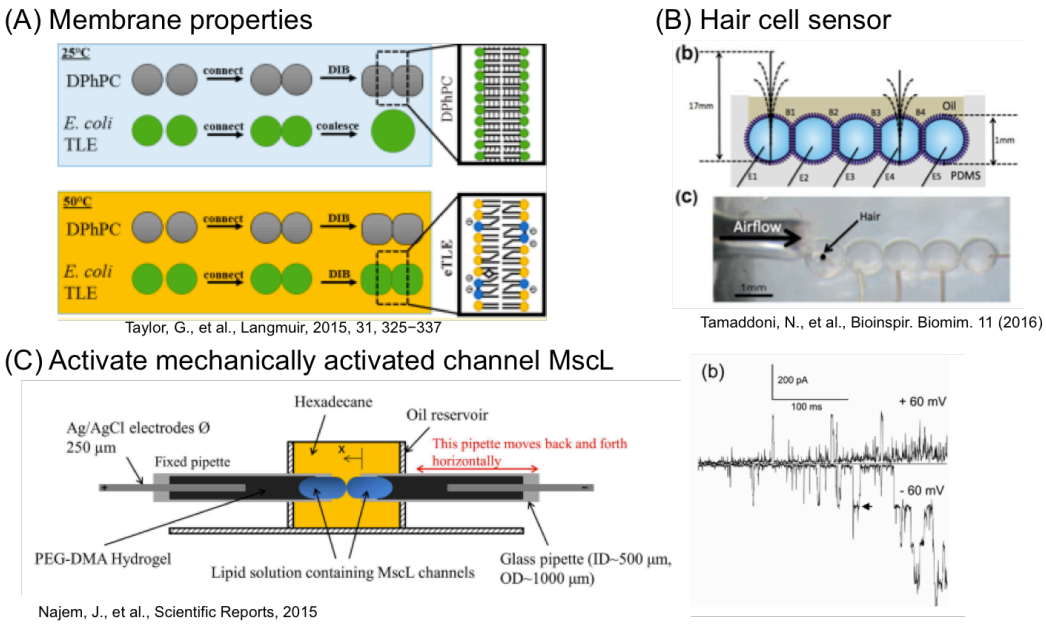

Figure 4. DIB systems used to study and employ biomolecular functionality. Examples include (A) membrane properties such as the effect with temperature and other lipid types, (B) a hair cell sensor and (C) to activate protein channel such as MscI a mechanically activated channel.

assemblies that are able to autonomously [42] and even collectively [42, 43] respond to internal or external physical stimuli. The development of these material systems utilizes a synthetic lipid membrane to house biological molecules that attribute specific functionality to the system [38, 44-46].

There are several reported methods for forming lipid-coated droplets in oil to form DIBs. Common techniques include positioning droplets within the fixed geometry of a rigid, solid substrate [29], moving droplets via electrodes attached to micromanipulators [28], using mechanical force to control the compression of the solid substrate containing the droplets, thereby regulating contact between adjacent droplets [35, 47], and droplet manipulation using electric fields (i.e. dielectrophoresis and electrowetting on dielectrics) [48, 49], light-induced heating [50], magnetic fields [51], and even inkjet printing of droplets at defined positions [52]. While these methods are repeatable, most are not well suited for quickly

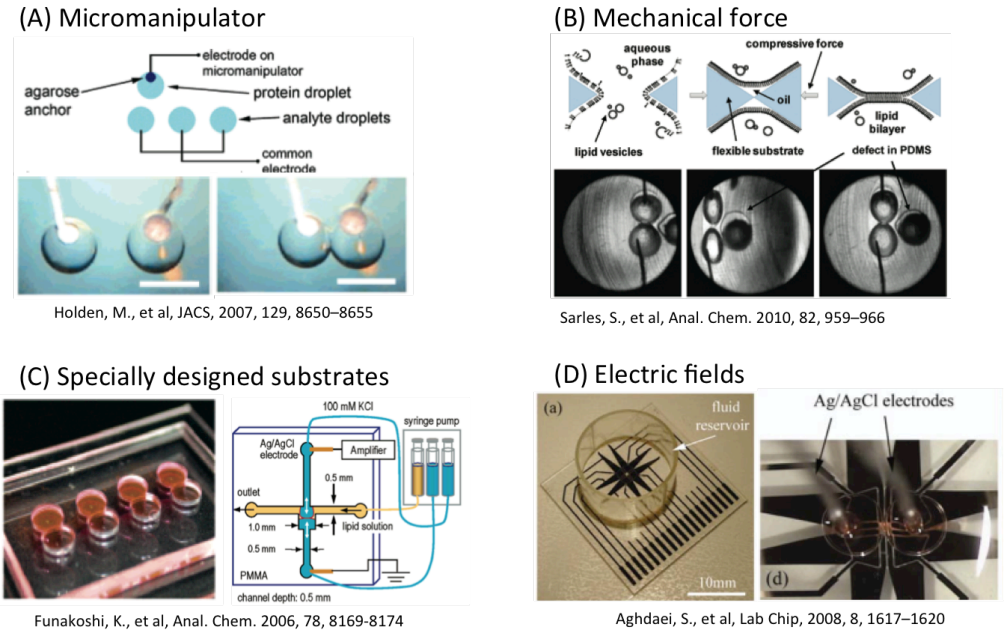

Figure 5. Common methods to form DIBs include (A) micromanipulator to bring into contact individual droplets, (B) a mechanical force on the surrounding substrate to either promote or inhibit droplets contact, (C) a specially designed substrates that use fixed geometry, and (D) electric fields in the form of dielectrophoresis and electrowetting.

assembling large numbers of DIBs. Additionally, most of these techniques also require manual dispensing of droplets using micropipettes, which is suitable only for creating DIBs with large droplets (>100 μm diameter, >50 nL in volume) due to the minimum volume that can be readily pipetted in this manner.

1.2.1 Electrical characterization of synthetic cell membranes

A number of techniques exist that have been used to characterize lipid bilayer structure and properties (neutrons, x-ray, anisotropy, permeability). However, this dissertation focuses largely on electrical measurements with planar bilayers which are advantageous due to the ability to directly access both sides of the membrane and measure electrical and physical properties.

The electrical behavior of a lipid bilayer can be most simply represented as a parallel RC circuit [47, 53]. Figure 6A shows the electrical circuit configurations for a droplet interface bilayer where *R* is the membrane resistance, *C* is the membrane capacitance, and R_{es} is the resistance of the aqueous droplets. It should be noted that the electrical properties of the lipid bilayer, R and C, represent physical aspects of the structure of the membrane. For instance, membrane resistance represents the portion of the membrane that acts as a barrier to ion transport. Alternatively, membrane capacitance stems from the layered structure of the membrane and the dielectric hydrophobic region, which provides a means of storing charge or generating and propagating capacitive signals.

The complex impedance of a DIB, $Z_M(\omega)$, has been derived elsewhere and is given by [53]:

$$Z_M(\omega) = \frac{R}{1 + j\omega RC} + R_e \tag{2}$$

Equation 2 yields an impedance spectrum such as that shown in Figure 6B (here assuming *R* = 10 GΩ, *C* = 100 pF, *Re* = 10k Ω). The circuit is comprised of three basic elements (electrode-electrolyte resistance, membrane resistance, and membrane capacitance), and current through the membrane is frequency

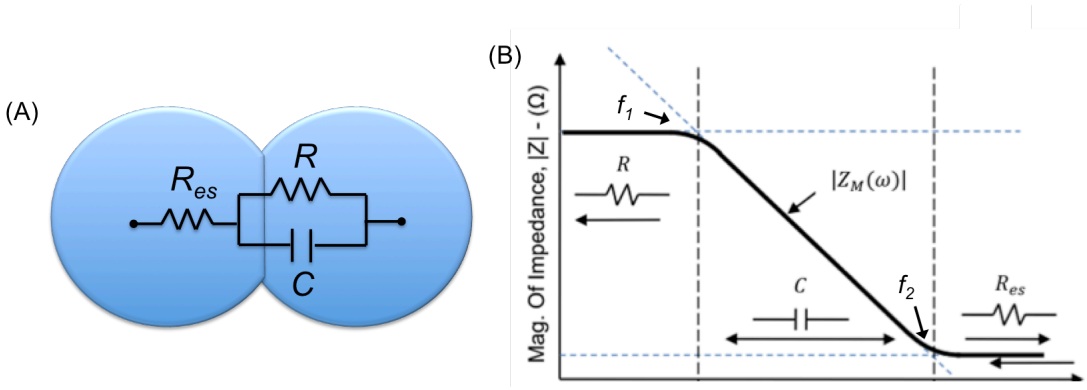

Figure 6. (A) Equivalent electrical circuit of a DIB. (B) The complex frequency dependent impedance of a bilayer. Modified from [52].

dependent whereby current follows the path of least resistance shown in Figure 6B. Application of zero-frequency dc voltage essentially leads to an open-circuit condition for the path involving membrane capacitance; dc current passes through the electrodes, the electrolyte, and the resistive portion of the membrane. Given that bilayer resistance, often on the order of gigaohms, is significantly higher than that of the electrode-electrolyte resistance (typically, $R_e \leq 10$ kΩ), current is determined via Ohm's law and the membrane resistance when applying dc voltage ($I=V/R$). Slightly more complex behavior emerges upon application of ac voltage signals, however, as a lower frequency exists at which current through the membrane begins to be dictated by the capacitance. This lower corner frequency (*f1* on Figure 6B) is the frequency at which the impedance of the membrane capacitance begins to fall below that of the membrane resistance. A common technique for measuring membrane capacitance involves application of an alternating triangle wave of constant amplitude (A) and frequency (f), and it can be shown that the membrane capacitance (C) results in square wave current amplitude (I) given by

$$I = 4AfC \tag{3}$$

As the frequency of the input ac voltage waveform is continually increased, the impedance of the membrane capacitance drops below the resistance at the electrode-electrolyte interface. At frequencies above this upper corner frequency (*f2* on Figure 6B), the impedance of the bilayer remains constant at $Z = R_{es}$. In combination, the frequency-dependent impedance of the bilayer follows the path of the bold line drawn in Figure 6B. Knowledge of the electrical response of the bilayer proves to be useful in allowing precise measurements of the membrane resistance and the membrane capacitance by applying ac input voltages of an appropriate frequency.

1.3 Droplet-based microfluidics

Droplet-based microfluidics provide precise droplet control and manipulation to generate and package a multi-droplet DIB array. There are numerous techniques

to form and position droplets within a microfluidic device [54, 55]. Droplet formation usually occurs on-chip in an oil-filled channel, and the process can be divided into three main categories based on flow regimes: (1) droplet formation in cross flowing (T-junction) streams of oil and water, (2) droplet formation in flow-focusing streams, and (3) droplet formation in co-flowing oil and water streams [56]. In these approaches, droplet size and production rate are dictated by adjusting the oil and water flow rates and the channel dimensions, which range from 1 μm to several hundred micrometers. Although these techniques have been proven successful for high-throughput droplet generation, it is known that steady state production of mono-disperse droplet sizes is not achieved immediately. This transient results in a need for downstream sorting prior to droplet collection in applications where droplet size is important.

In addition, there are a handful of studies that have demonstrated hydrodynamic, or flow-induced, methods for trapping a single droplet or bead within a microfluidic substrate (Figure 7). Droplet positioning can be guided by intra-channel structural elements that create parallel paths for fluid flow. For example,

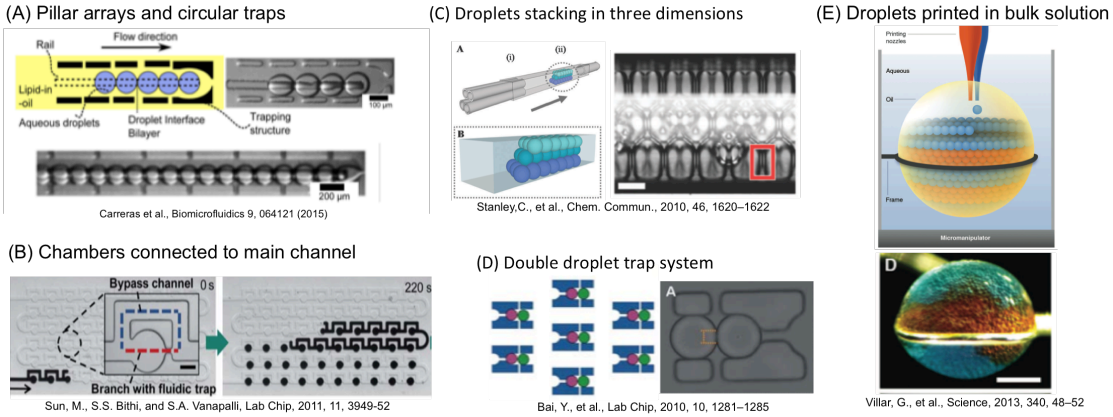

Figure 7. Microfluidic techniques used to form highly packed arrays of surfactant-stabilized droplets or discrete pairs of DIBs include (A) pillar arrays or circular traps, (B) chambers connected to the main channel, (C) stacking droplets in 3D to fill a channel, (D) a double droplet trap system, and (E) droplet printing.

circular traps or pillar arrays enable to position a droplet while maintaining oil flow through the device [57-60]. So far, this approach of hydrodynamic microarrays has been mainly used to capture one individual microsphere or bead per trap. Also, there have been reports of efforts to assemble functional arrays or networks of DIBs as a single unity or discrete pairs. Typically these networks are two-dimensional and have less than four interfaces per droplet [28, 58, 61-63]. More recently, a droplet-on-rail strategy was used to produce parallel droplet bilayer networks up to 20 interfaces [64]. Additionally, higher order three-dimensional DIB arrays can be formed via manual techniques [52, 65] or a microfluidic approach [66, 67].

However, the ability to electrically interrogate specific lipid bilayers in multi-layer droplet arrays, especially those assembled within a microfluidic device, has not been addressed to date. The presence and properties of lipid bilayers are typically quantified using electrical measurements of membrane capacitance and resistance [28, 32, 61, 68]. DIBs formed with large droplets (i.e. >50 nL) allow for wire-type electrodes to be manually inserted into the droplets. However, droplets formed within a microfluidic platform have the potential to be much smaller in size from 2-350 μm [54] and are enclosed within a sealed substrate. While, optical and fluorescence imaging have been employed to obtain qualitative visualization of bilayer presence [57, 69], they do not provide complete characterization of the interface such as resistivity and durability. There has been a successful effort to insert silver wire into a microfluidic system [70]. In that particular system, a single DIB is formed and measured before it is ejected and new droplet(s) occupy the region where electrodes are present.

1.4 Asymmetric lipid membranes

Synthetic lipid bilayers provide models of cell membranes to study biomolecular interactions and signal transduction. However many model membrane studies utilize symmetric, single lipid compositions, which are not as biologically relevant,

while there are limited number of studies using mixtures of two to four components. Therefore, there is still much to be learned about the effects of diverse and complex composition on the properties and functions of membranes and interactions with membrane-active proteins.

In nature, cell membranes are asymmetric where the content on one side of the bilayer is different from the other and the lipids of the membrane itself differ from the inner and outer leaflets (Figure 8). One example is the plasma membranes of eukaryotic cells where aminophospholipids are primarily in the cytosolic leaflet while phosphatidylcholine and sphingomyelin dominate in the outer leaflet [71, 72]. This transbilayer asymmetry is an important aspect of membrane-mediated signaling and cellular functions. It is generally understood that there are families of membrane proteins responsible for “flipping” and “flopping” lipid headgroups from one leaflet to the other. However, the mechanisms that generate and maintain asymmetry phospholipid flip-flop rates have been challenging to obtain

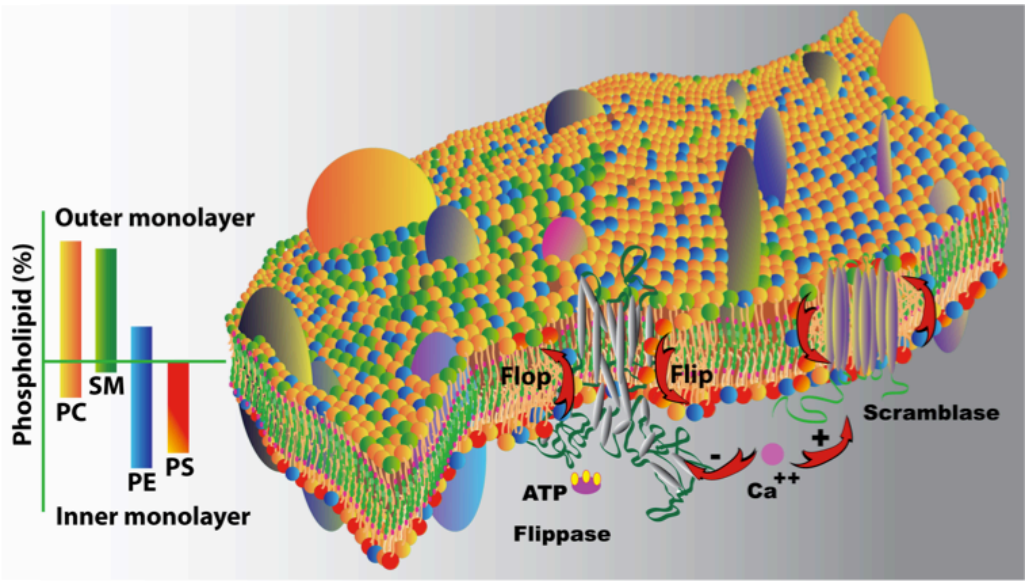

Figure 8. Cell membranes are asymmetric where the content on one side of the bilayer is different from the other and the lipids of the membrane itself differ from the inner and outer leaflets. Reproduced from [72].

and are the subject of ongoing research, along with the influence of composition including the presence of transmembrane proteins on flip-flop rates [73]. While there are several reports addressing the influence of bilayer composition on flip-flop rates, these studies have problems with the method such as use of bulky lipid fluorescence dyes that can alter physical properties of the model membrane formed and discrepancies between studies [23, 73, 74]. However, there are techniques to examine membrane asymmetry not necessarily to determine flip-flop rates. For instance characterization of membrane asymmetry can be evaluated by measuring the asymmetric surface potential via capacitance measurements, which has been performed and investigated by several groups [75-79]. However, utilizing capacitance measurements of asymmetric membranes can be applied over time to determine flip-flop rate. To further understand the complexity of cell membranes, there are studies investigating the effects of membrane asymmetry on the behavior of transmembrane pore and channels with respect to bilayer leaflet compositions [34, 80-84]. In a study by Hall, alamethicin appeared to induce a voltage-dependent lipid exchange between leaflets of a bilayer [81]. Furthermore, Vodyanoy et al. found membrane asymmetry can alter the asymmetry of alamethicin current-voltage curve [83].

Implementing asymmetric lipid bilayers creates a more biological relevant model systems, and it enables the addition of a “sidedness” to the system that can be used to store, convert, and dissipate energy. For example, Zheng et al. developed an asymmetric membrane structure that is highly selective of ionic transport to create a concentration-gradient driven energy harvesting device [85]. Another study used asymmetric pH environments to control ion channel activities [86]. More recently there are studies investigating the effects of membrane asymmetry on the behavior of transmembrane pore and channels with respect to bilayer leaflet compositions [34, 80].

1.5 Microfluidics for protoplast cell study assays

Microfluidic devices are a relatively new method for studying the behavior and activities of cells; gaining popularity due to miniaturization and high-throughput capabilities. Cell-based microfluidics has focused primarily on cell culture growth and morphology [87], protoplast fusion (e.g. electrofusion and chemically-induced fusion) [88], dynamic environments and gradients, strain characterization and high-throughput analysis. For these studies, cells are typically captured in large chambers or flown through wide channels. Further advancements can be made for the single cell capture, analysis, transfection, and gene expression of individual cells, particularly in the field of plant biotechnology.

Plant cell cultures typically require large volumes of media and it is difficult to maintain protoplast cultures. Studies of maintaining cultures in microfluidic devices show that cells remain viable for engineering purposes [87, 88]. In one study of tobacco protoplasts, healthy protoplasts were captured in a microfluidic channel and the culture medium was injected by a syringe pump at 50 to 100 μL/hr [87]. The protoplasts began to divide after 2 days of culture and formed a microcolony at 2 weeks. Cell division was found to occur 3 days earlier in the PDMS channel than in a petri dish due to the easier diffusion of nutrients throughout the channel. Wu et. al. conducted a similar study with tobacco mesophyll protoplasts and found similar results of cell division after 3 days and the formation of small cell masses after 6 days [88]. Following cell mass growth, PEG-fusion of protoplasts required 3-5 min with an efficiency of 28.8%. The success of these attempts illustrates that microfluidic devices provide an excellent platform for a wide range of cell-based studies: including growth and division, high-throughput screening, transformation and gene expression, and biomimicking.

Transformation of plant cells allows for the altering of DNA with the purpose of giving the plant a new and useful trait. There are many methods for introducing the new segment of DNA to be inserted in the plant chromosome, all of which start with transfecting a single cell which can then be regenerated into full plants. Some of the methods for plant cell transformation, including PEG-mediation, can only be done with protoplasts. Transformation of protoplasts has a higher efficiency than cells with intact cell walls due to the lack of the thick barrier; however, the efficiency is still very low in many plant species [89-91]. Traditional methods of protoplast transformation are limited by a difficulty in obtaining high concentrations of viable protoplasts, low transformation efficiency, the necessity for a large quantity of DNA, and inconsistent results across species [89-93].

Microfluidics can help overcome these disadvantages by system miniaturization, enhanced efficiency, and the ability to study single cell transformation. The use of a microfluidic device allows for fewer protoplasts, (one cell per trap instead of $1x10^6$ protoplasts/mL) and DNA, which is often expensive and difficult to produce. By adding traps to the design of the device, individual protoplasts are captured for focused study at the single cell level of transformation. The advantage of being able to study single cell transformation is a closer examination of protein expression and the collection of proteins secreted from the plant protoplasts.

1.6 Gaps and objectives

1.6.1 Scientific gaps

We define the following scientific gaps:

Gap 1. To date, many of the studies involving synthetic lipid bilayers only include a single DIB. The most common DIB assembly method employs manual pipetting of aqueous volumes to form droplets, followed by positioning droplets to

encourage contact-initiated bilayer formation. However, manually dispensing and arranging droplets is best suited for creating DIBs with droplets larger than 100μm in diameter (>~50nL) due to the minimum dispensing volume of a pipette (~50-100nL) and the difficulties in individually manipulating droplets smaller than 100μm. A manual approach can also introduce unwanted variability in droplet size, contact area, and the quality of the lipid monolayer at the surface of a droplet through the use of instruments to position droplets. Therefore there is a technical need for an automated high-throughput droplet generation and arrangement system to create an array of DIBs, which can be electrically interrogated, in an enclosed substrate. With this high-throughput DIB system on hand, it would be straightforward to investigate numerous basic lipid bilayer studies and membrane-mediated processes with greater efficiency and statistical significance.

Gap 2. In order to achieve a more biologically relevant model cell membrane, studies of lipid asymmetry are of high interest. For instance, the influence of bilayer composition on flip-flop rates is not well understood. Also, the effects of peptides on the disruption of asymmetric lipid membranes and intramembrane potential are not well known due to technical challenges in both assembling and characterizing the asymmetry of lipid membranes.

Gap 3. While there are microfluidic devices capable of single cell capture and analysis such as drug screening and cell division, there is currently no efficient approaches to perform and study gene transformation on individual plant protoplast cells. The ability to isolate and transform single cells within an automated microfluidic array would thus greatly improve our ability to study gene transformation on an individual cell basis, with greater spatial and temporal resolution of each cell's response, and enable post-collection of successfully transformed cells to grow whole plants containing specific genes.

1.6.2 Research objectives

The following objectives attempts to address the scientific gaps mentioned above:

Objective 1 (addressing Gap 1). Use an equivalent electrical circuit modeling approach to design a self-contained microfluidic device capable of generating monodisperse lipid-encased droplets and routing the droplets to predetermined locations to form an array of DIBs. The device needs to enable the collection of droplets at every trap in the array, and minimize the hydrodynamic pressure developed across trapped droplets to prevent unwanted droplet release from traps or disrupt the resulting DIB, and be scalable in an array layout.

Objective 2 (addressing Gap 1). Design and fabricate integrated thin-film electrodes within the same droplet generation and trapping microfluidic device fabricated in Objective 1 to permit simultaneous electrical characterization of multiple droplet interface bilayers to improve the efficiency of studying membrane properties and peptide insertion.

Objective 3 (addressing Gap 2). Incorporate a method to generate alternating droplets to form asymmetric DIBS in the microfluidic device from Objective 1&2. Then, electrically characterize the intramembrane potential between bilayers containing asymmetric zwitterionic phospholipid leaflets (i.e. DPhPC and DOPhPC). This *in situ* measurement technique will be applied for the first time on an array of asymmetric DIBs to study lipid asymmetry versus time and in the presence of peptides.

Objective 4 (addressing Gap 3). Design and fabricate a microfluidic system for systematic single cell capture of plant protoplast cells for the purpose of DNA transformation. A similar resistive modeling approach used in Objective 1 will be applied to design traps and array layout, and provide guidelines for device

operation conditions such as flow rates to maintain appropriate pressure throughout the system to minimize cell squeeze through.

CHAPTER 2
EXPERIMENTAL METHODS AND DATA ANALYSIS

This chapter describes experimental methods, as well as methods used in the analysis of data, that are generally applied throughout the work described in this dissertation.

2.1 Materials for lipid bilayer formation

2.1.1 Common materials

The following phospholipids were used in these studies remained in powder form and stored at -20°C until further use: 1,2-diphytanoyl-*sn*-glycero-3-phosphocholine (DPhPC, Avanti Polar Lipids), 1,2-di-O-phytanoyl-sn-glycero-phosphocholine (DOPhPC, Avanti Polar Lipids), glyceryl monooleate (GMO) (Sigma Aldrich). Alamethicin (Alm) from *Trichoderma viride* is obtained in powder form from A.G. Scientific.

Sodium chloride (NaCl), 3-(N-morpholino)propanesulfonic acid (MOPS), sodium hydroxide (NaOH), ethanol, squalene, hexadecane, tetradecane are acquired from Sigma Aldrich. Unless otherwise stated, aqueous buffer is prepared by titrating 1 M NaCl, 10 mM MOPS stock solution with 0.5 M NaOH solution to achieve pH 7.4.

2.1.2 Preparation of liposome and peptides

DIB formation in these studies are performed either lipid-in the aqueous phase or lipid-out in the solvent phase. The placement of lipids is stated for each study. For experiments using lipid-in, the lipids are dissolved to a concentration of 2 mg/mL in aqueous buffer to create stock solutions of multilamellar vesicles. Lyophilized powder is dissolved in aqueous buffer solution followed by five freeze/thaw cycles. Then, aliquots of the prepared stock solution is extruded

through either an Avanti MiniExtruder with Whatman 100 nm polycarbonate filters or 100 nm LipX Extruder (T&T Scientific) to create unilamellar liposome solution that is stored at 4 °C. For lipid-out, lipids are dissolved in the organic phase at a concentration of 2 mg/mL. The oil phase used is stated for each study.

Alamethicin, an antimicrobial peptide from the fungus *Trichoderma viride is* dissolved in ethanol at 10 mg/mL and diluted with aqueous buffer to a final concentration of 2.5 mg/mL to create a stock solution that is stored at −20 °C. For DIB experiments with alamethicin, the stock solution is diluted to 25 µg/mL with buffer and then added to 2 mg/mL unilamellar liposome solution to achieve the desired final alamethicin concentration. All peptide/lipid stock solutions are stored at 4°C and used within 2 weeks.

2.2 Microfluidic device design and fabrication

2.2.1 Microchip fabrication

A single T-junction or two opposing T-junction is used for droplet production. The incoming droplet stream is routed through microchannels and captured using series of hydrodynamic traps branching from the main channel. Each trap has an area designed to capture droplets serially with bleed valves that serve to direct the droplets into the vacant trap without allowing the droplets to escape after capture. Bleed valves are spaced such that the trapped droplets are close enough to connect to form a DIB. The device dimensions are tailored for 125 µm diameter droplets.

The microchips are fabricated using standard photo- and soft-lithography techniques.[94] Briefly, a silicon wafer is spin-coated with photoresist and exposed to UV light through a chrome photomask using a photolithography aligner such that unmasked areas are cross-linked. Then, a deep reactive-ion etching process is employed to further etch the silicon wafer to a depth of 125

μm. After the master wafer is stripped of remaining photoresist and silanized to prevent adhesion during soft-lithography, uncured Sylgard 184 (Dow-Corning) PDMS (10:1 wt-wt ratio of base to curing agent) is poured over the wafer, degassed, and baked for at least 2 hours at 80°C. Cured substrates are sliced and peeled off the master wafer. Inlet and outlet access holes are pierced using a 0.75 mm diameter biopsy punch. The PDMS substrate is bonded to a PDMS coated glass cover slide or a slide with deposited thin-film electrodes after an oxygen plasma treatment. The sealed devices are baked at 80°C for at least 48 hours to create a hydrophobic environment. Figure 9 shows a schematic summary of device fabrication once a master wafer is made.

2.2.2 Thin-film electrode fabrication

Electrodes are placed strategically such that each pad is directly under the trapped droplet. Similar to the microfluidic fabrication, a chrome photomask with the desired electrodes design is developed followed by photolithography with a

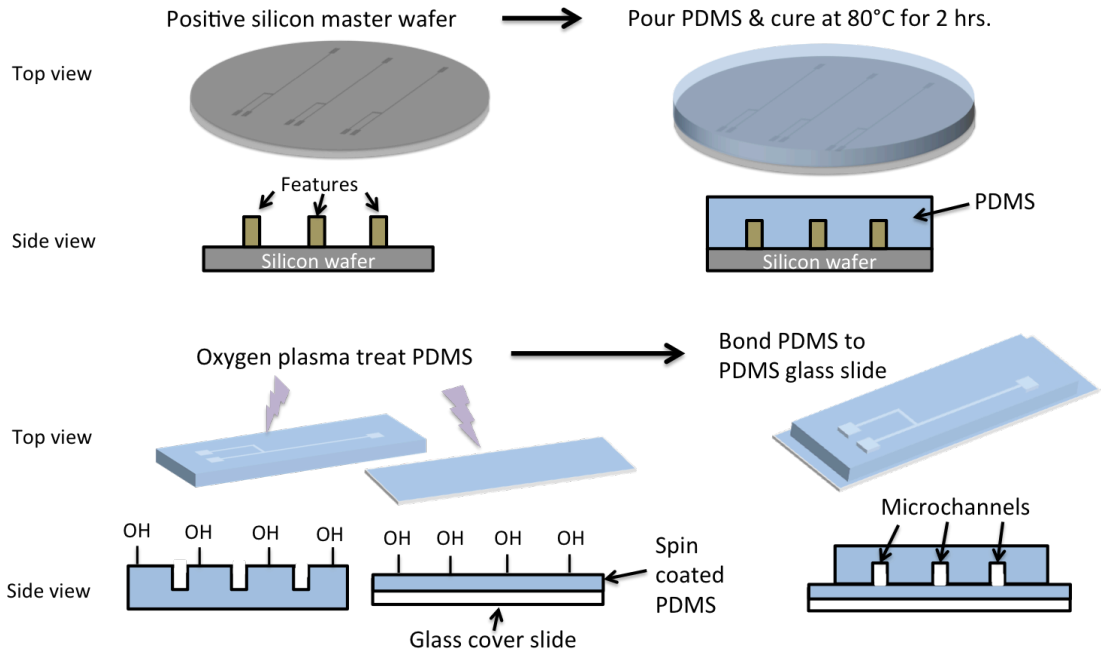

Figure 9. Schematic of microfluidic fabrication.

glass wafer (Borofloat). A single electrode pathway includes a 30x30 µm droplet pad with leads extending in width increments connecting to a large 3x3 mm pad.

A dual gun electron beam evaporation chamber is used to deposit 10 nm adhesive layer of chrome and 300 nm of silver onto the glass wafer. Next, lift-off in acetone and isopropyl alcohol is performed to remove unattached metals. Prior to bonding with PDMS microchannels, bleach is pipetted onto the 30x30 µm electrode pads to form silver-silver chloride reversible electrodes. Chloride exposure is limited to less than 30 seconds to prevent over-bleaching. Then, the electrodes are thoroughly washed with deionized water. Microchips undergo plasma oxidation, bonded to PDMS, and baked at 80°C for at least 48 hours. Then, silver wire is soldered onto the 3x3 mm pads in order to connect to the patch clamp amplifier. Figure 10 shows the summary of the electrode fabrication process.

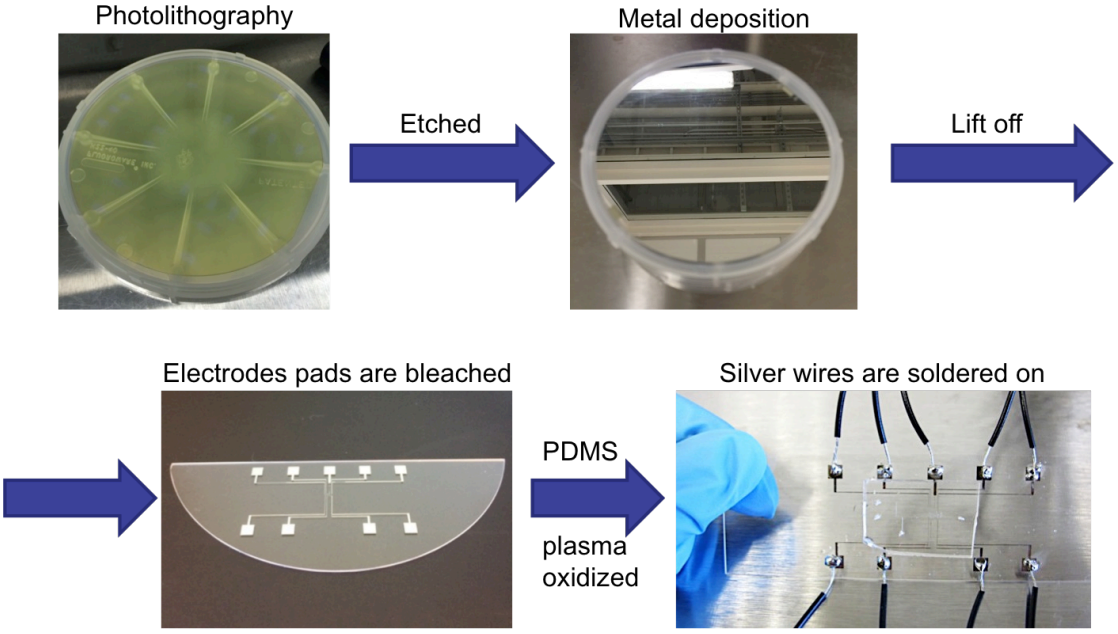

Figure 10. Summary of electrode fabrication for encapsulated DIBs.

2.2.3 Device operations

A dual syringe pump (Gemini 88, KD Scientific) is used to control the flow rates of the oil and water injections. PTFE tubing and 23 gage blunt stainless steel needles are used to connect syringes to inlet ports in microfluidic device. Images are obtained using a CCD camera (QImaging QIClick) connected to an inverted microscope (Olympus IX51). The device is also reusable and can be cleared via simple oil backwashed through the outlet.

2.3 Electrical measurements to monitor bilayer formation, quantify membrane properties, and peptide insertion

2.3.1 Electrical characterization of a bilayer

The equivalent electrical circuit for a single lipid bilayer is a simple RC circuit. As described in Section 1.2.1, the bilayer can be modeled as a resistor and a capacitor in parallel (Figure 11A). Electrical measurements are used to monitor the formation of a DIB on top of thin film electrodes. As a DIB begins to form and approach equilibrium, capacitance of the interface also begins to increase and stabilize. Continuous application of a triangular voltage waveform (Figure 11B) results in a square current waveform whose amplitude is proportional to the area of the bilayer as shown in Section 1.2.1 Equation 3. Thus, square-wave measurements confirm bilayer formation (Figure 11C) and provide a measure of the bilayer area. Bilayer area (A) can be computed using a known value for the membrane specific capacitance (C_M) since $A=C/C_M$.

2.3.2 Electrical recordings

The electrical current of the lipid bilayers are monitored using an 8-channel patch clamp amplifier (Triton, Tecella LLC) and TecellaLab software to digitally control the applied voltage to the sensing electrode and measure the induced currents in the network. Each electrode is connected to a separate measurement channel on the amplifier. A picture of a device connected to the amplifier is shown in Figure

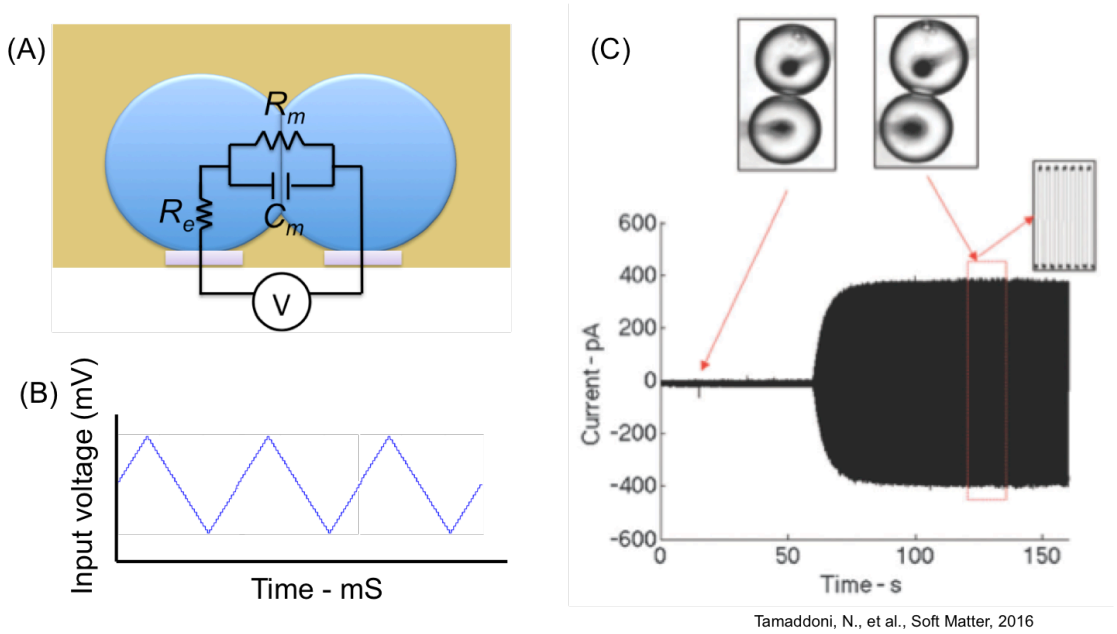

Figure 11. Electrical membrane characterization. (A) Schematic of an equivalent electrical circuit for a DIB on top of thin film electrodes. (B) Schematic of a triangular input voltage waveform. (C) The square wave current waveform used to measure membrane capacitance and area.

12. A triangular voltage waveform (40 mV, 50 Hz) is applied as needed on independent electrodes to monitor bilayer capacitance. Measured current is sampled at 2 kHz or 20 kHz for alamethicin, filtered at 1 kHz using a low-pass filter, and digitized using 16-bit A/D conversion within the Triton. Local shielding with aluminum foil around the wired electrodes attached to the amplifier is used to reduce the noise. The calculated RMS noise in all experiments is less than ±10 pA, and we observe that the noise does not increase when the syringe pump is running and solution is flowing through the channels.

2.3.3 Cyclic voltammetry to measure alamethicin insertion

Alamethicin (Alm) insertion is observed in response to applied transmembrane voltage using electrical measurements of current through the membrane. Alamethicin insertion at the macroscopic level is quantified via cyclic voltammetry (CV), a method that involves linearly ramping the applied voltage while

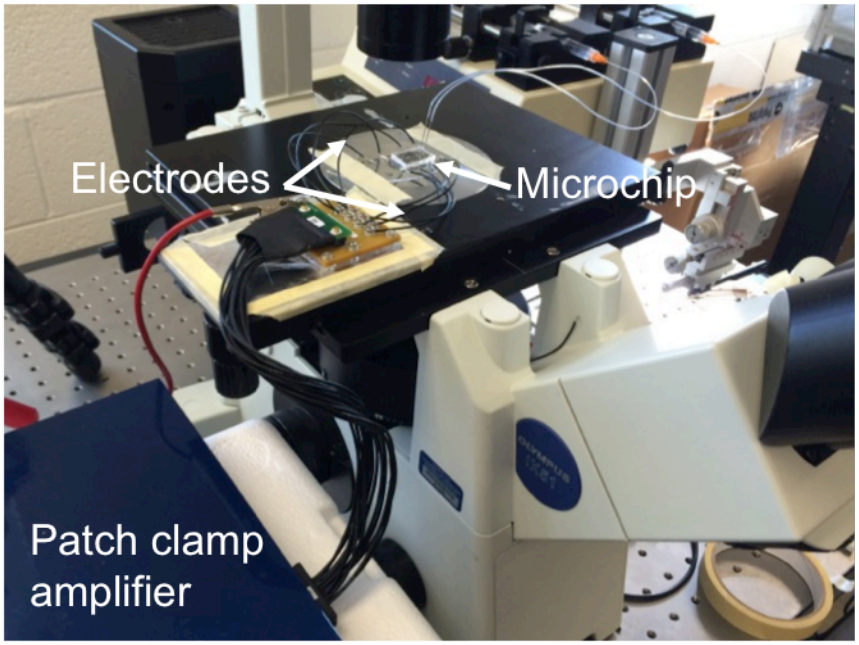

Figure 12. Experimental set-up of microchip with electrodes attached to a patch clamp amplifier.

measuring current. CV waveforms are programmed in TellecaLab, which results in digitization of the voltage sweep. Scans are conducted in a step-wise fashion at an effective rate of 10 mV/sec between +170 mV and -170 mV.

CHAPTER 3
A METHOD FOR ENCAPSULATING AN ARRAY OF DROPLET INTERFACE BILAYERS WITH ELECTRICAL MEASURMENTS

This chapter[1] addresses Objective 1 and 2 aiming towards an automated high-throughput droplet generation and arrangement system to create an array of DIBs, which can be electrically interrogated, in an enclosed substrate. With this high-throughput DIB system on hand, it would be straightforward to investigate numerous basic lipid bilayer studies and membrane-mediated processes with greater efficiency and statistical significance. As part of Objective 1, we used an equivalent electrical circuit modeling approach to design a self-contained microfluidic device capable of generating monodisperse lipid-encased droplets and routing the droplets to predetermined locations to form an array of DIBs. This device is able to collect of droplets at every trap in the array, and minimize the hydrodynamic pressure developed across trapped droplets to prevent unwanted droplet release from traps or disrupt the resulting DIB. Also, we addressed Objective 2 through design and fabricate integrated thin-film electrodes allowing simultaneous electrical characterization of multiple droplet interface bilayers to improve the efficiency of studying membrane properties and peptide insertion.

---

[1] Note: This chapter is reproduced from our published work: Nguyen, M., Srijanto, B., Collier, C.P., Retterer, S.T., Sarles, S.A., Hydrodynamic trapping for rapid assembly and *in situ* electrical characterization of droplet interface bilayer arrays. ***Lab Chip,*** 2016, 16, 3576-3588.

Here, we demonstrate a new, low-volume microfluidic system that automates droplet generation, sorting, and sequential trapping in designated locations to enable the rapid assembly of arrays of DIBs. The channel layout of the device is guided by an equivalent circuit model, which predicts that a serial arrangement of hydrodynamic DIB traps enables sequential droplet placement and minimizes the hydrodynamic pressure developed across filled traps to prevent squeeze-through of trapped droplets. Furthermore, the incorporation of thin-film electrodes fabricated via evaporation metal deposition onto the glass substrate beneath the channels allows for the first time *in situ*, simultaneous electrical interrogation of multiple DIBs within a sealed device. Combining electrical measurements with imaging enables measurements of membrane capacitance and resistance and bilayer area, and our data show that DIBs formed in different trap locations within the device exhibit similar sizes and transport properties. Simultaneous, single channel recordings of ion channel gating in multiple membranes are obtained when alamethicin peptides are incorporated into the captured droplets, qualifying the thin-film electrodes as a means for measuring stimuli-responsive functions of membrane-bound biomolecules. This novel microfluidic-electrophysiology platform provides a reproducible, high throughput method for performing electrical measurements to study transmembrane proteins and biomembranes in low-volume, droplet-based membranes.

3.1 Introduction

There are several methods available for generating and arranging lipid-coated droplets to form DIBs. The most common DIB assembly method employs manual pipetting of aqueous volumes to form droplets, followed by positioning droplets to encourage contact-initiated bilayer formation. Examples of ways to arrange pipetted droplets include the use of micromanipulator(s) to push and pull droplets via wire-type electrodes,[28] rigid, solid substrates containing adjacent wells for droplet positioning,[29, 95] mechanical force to control the compression of a solid substrate and regulate inter-droplet contact,[35] applied electrical fields to slide

droplets across a dielectric surface,[96, 97] and even magnetic fields to lift and place droplets containing magnetic species.[51, 98] While many of these techniques enable precise control over droplet position and even bilayer area,[32, 33, 99, 100] manually dispensing and arranging droplets is best suited for creating DIBs with droplets larger than 100μm in diameter (>~50nL) due to the minimum dispensing volume of a pipette (~50-100nL) and the difficulties in individually manipulating small droplets.

Flowing oil and water through microfluidic junctions provides an alternative means to generate aqueous droplets in oil.[54-56] While there are multiple geometries for microfluidic droplet generators,[54, 55] the droplet formation process is generally based on the relative flow rates of oil and water supplied to the device and on the dimensions of the channel(s), which typically range from 1 μm to several hundred micrometers in width and height. This approach is specifically well suited for generating continuous streams of low-volume (including fL and pL volumes) droplets. Once droplets are formed in a microchannel, hydrodynamic trapping can be employed to capture droplets from a moving stream and place them in stationary locations.[101-103] For instance, circular-shaped traps[57, 62, 70, 104] and pillars/rails arrays[58, 59, 63, 64] have been used to arrange lipid-coated water droplets to form DIBs within microfluidic devices.

Bilayer formation and membrane properties are often confirmed and quantified, respectively, in DIBs (as well as for other model membrane systems) using electrical measurements of membrane capacitance and resistance.[28, 32, 61, 68] Electrophysiology measurements are also standard protocol for recording ion transport through transmembrane peptides and proteins.[28, 105-107] DIBs formed with large droplets (e.g. ~1 mm diameter) allow for wire-type electrodes to be inserted into the droplets for applying voltage and measuring current across the interface. However, droplets formed in a microfluidic platform can be much

smaller in size (e.g. from 2-350 μm diameter[54]) than ones that are manually dispensed and often remain within the sealed device, which complicates electrode access for electrical measurements.[105] As a result, imaging techniques have primarily been used thus far to confirm bilayer formation and quantify mass-transport across membranes for DIBs in microfluidic devices.[57-59, 63, 64, 104]

Integrating electrodes into microfluidic platforms for membrane electrophysiology has received significant attention in recent years. For example, Behrends, et al developed microfluidic, parallel patch-clamp systems with thin-film surface electrodes for enabling simultaneous electrophysiology of multiple cells suctioned at separate locations in the device.[108-110] Separately, thin film electrodes have been used in microfluidic devices to electrically interrogate suspended lipid bilayers (SLBs) formed across the pores of a dividing substrate[111-116] or between the walls of microfluidic channels.[117] While some of these platforms were connected to multi-channel current measurement devices that permit simultaneous measurements of multiple membranes,[113-116, 118, 119] others, including a study of a 2-DIB array using thin film electrodes, were paired with digital switching circuits to cycle a single-channel measurement device across multiple electrode pairs.[97, 112, 117]

Therefore while a few studies have included simultaneous measurements of multiple DIBs,[118, 120] none has demonstrated this capability within a microfluidic device. To address this gap, we present a new microfluidic architecture that is capable of producing and routing low-volume aqueous droplets to predetermined locations for automated DIB formation and which features thin-film surface electrodes located beneath droplet pairs for enabling *in situ* electrical interrogation of multiple DIBs within the sealed device. A circuit-based modeling approach is employed to design and arrange hydrodynamic traps that are used for immobilizing droplets and enabling DIB formation at

predetermined locations. Experiments performed on prototype devices fabricated based on model predictions demonstrate the ability to form multiple sets of DIBs within an enclosed device. By connecting the built-in electrodes to a multi-channel patch clamp amplifier, we show for the first time in a microfluidic device the ability to simultaneously assess bilayer capacitance during successive DIB formations and record stochastic, voltage-dependent ion channel gating in multiple membranes.

3.2 Resistive circuit model for direct trapping and droplet sorting

Our understanding of droplet behavior within a microfluidic device is guided by relating fluidic systems to electrical circuits. Using an electrical circuit analogy, a resistive flow model is developed to determine appropriate dimensions for the fluid channels used for droplet sorting and trapping as well as for designing the layout of a multi-trap array within the encapsulating substrate. In a single-phase laminar flow, the pressure difference along a section of a microchannel is equal to the product of the applied volumetric flow rate, *Q*, and the hydrodynamic resistance of the channel, *R*. The hydrodynamic resistance for Poiseulle flow in a rectangular channel [101] is given by

$$R = \frac{12\mu L}{h^3 w}\left[1 - \frac{192}{\pi^5} \times \frac{h}{w} \times \tanh\left(\frac{\pi w}{2h}\right)\right]^{-1} \quad (4)$$

where *L*, *w*, and *h* are the length, width, and height, respectively, of a particular segment of the channel, and μ is the viscosity of the carrier fluid (i.e. oil for a DIB system). Assuming that the presence of dispersed droplets in the oil does not significantly affect the relationship between pressure and applied flow rate, Equation 4 can be used to design channels of specific dimensions to dictate the flow resistance in regions of a device and thereby affect the course of droplet travel.

We seek to obtain a device that utilizes steady fluid flow to place trains of separated droplets into sequential hydrodynamic traps, which serve to position

adjacent droplets close enough to enable spontaneous bilayer formation. A single hydrodynamic trap can be designed to accommodate two droplets to form one DIB, or it can be configured to host more than two droplets to enable the formation of a linear multi-membrane DIB series. In our device, a trap will consist of a rectangular compartment that resides adjacent to the main flow channel, which carries lipid-coated droplets in a stream of oil. Opposite entry from the main channel, each trap also features narrow exit channels, which we refer to as bleed valves.

The trap design and its ability to collect droplets carried in the main stream are thus based on the hydrodynamic resistance of the trap relative to that of the bypassing main channel. For instance, a droplet will prefer to enter an empty trap that has a hydrodynamic resistance, R_T, less than that of the resistance offered by bypassing the trap and flowing through the main channel, R_M. First, note that we approximate the hydrodynamic resistance of an *n*-droplet trap by dividing the trap into *n*-parallel lanes (from main channel to bleed valve) of equal hydrodynamic resistance (Figure 13A). These lanes represent the contribution to total flow resistance as would be experienced by a droplet as it travels across each lane of the trap from the main chain to a bleed valve. The flow resistance of each lane in a trap is calculated by

$$R_T = R_a + R_b , \tag{5}$$

where R_a is the portion of lane resistance due to the rectangular body of the trap and R_b represents the contribution to lane resistance from the bleed value. In this way, the total resistance for an unfilled, two-droplet trap would be given by $R_T/2$, which is the parallel addition of two equal lane resistances. While a standard trap is designed to house two droplets for 1 DIB, the number of lanes in a trap can be expanded to capture more than two droplets to form multiple interfaces. This expansion affects the total hydrodynamic resistance of the empty trap. For example, the unfilled trap resistance is $R_T/3$ for a three-droplet trap.

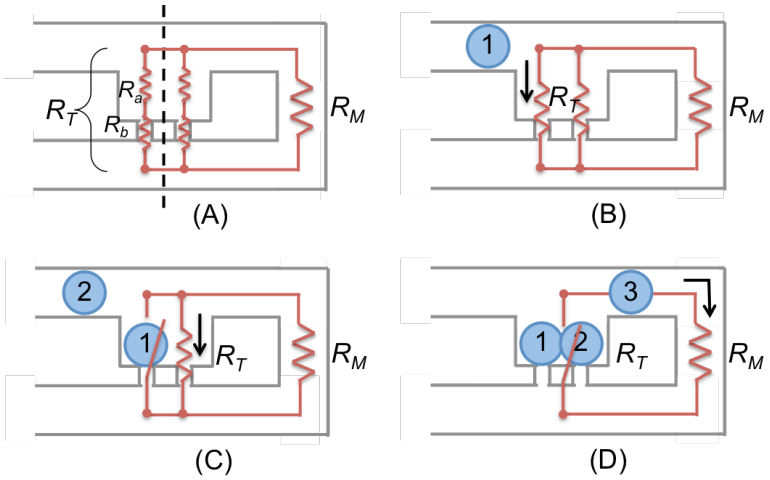

Figure 13. Schematic of hydrodynamic flow resistances in a single, 2-droplet trap. (A) Diagram of an unfilled trap designed for two droplets, where each lane of the unfilled trap has an equivalent resistance of R_a+R_b. (B) Droplet 1 enters the trap when the total trap resistance, R_T, is less than resistance of the main channel, R_M. (C) Droplet 2 enters the open lane of the same trap if R_T through the remaining portion of the trap is still less than R_M. (D) R_T becomes greater than R_M once two droplets are trapped, causing following droplets to bypass the filled trap.

When R_T is less than R_M, the first droplet in an incoming droplet train will divert from the main channel and come to rest in the hydrodynamic trap near one of the bleed valves (Figure 13B). If the total flow resistance through the remaining lane(s) of the trap is still less than that offered by the main channel, a second droplet will also preferentially flow into the open half of the same trap (Figure 13C). The bleed valves halt the droplets within the trap as long as the resulting pressure drop that develops across a droplet blocking a bleed valve does not cause the droplet to squeeze-through and escape. Specifically, the pressure drop across a filled trap must remain less than the Laplace pressure, ΔP_L, across the droplet residing at the entrance of a bleed valve, which can be calculated via

$$\Delta P_L = 2\gamma\left(\frac{1}{w_b} - \frac{1}{w_t}\right), \tag{6}$$

where, γ is interfacial tension of droplet-oil interface and w_b and w_t are widths of the bleed valve and trap, respectively.[101] Once a 2-droplet trap fills, the

presence of droplets at the entry to all bleed valves causes the flow resistance to increase significantly. As a result, the third droplet in the train bypasses the filled trap, preferring to remain in the main channel, which now offers a relatively lower resistance to flow (Figure 13D). Thus, an open trap behaves like a closed switch in an electrical circuit (with low resistance and high flow rate), while a filled trap acts like an open switch (with high resistance and low flow rate). This mechanism for droplet placement is known as direct trapping,[101] because the relatively lower trap resistance enables droplets to directly enter vacant traps and detour filled traps. Indirect trapping is associated with open traps that exhibit a higher relative resistance compared to the main channel.[101] For these, filling of traps occurs when droplets present in a section of the main channel pass the trap momentarily increase its local resistance, thereby redirecting successive droplets into the open trap.

The concept of direct trapping is essential for automatically filling many traps in a device with multiple droplets for DIB array formation. However, because the hydrodynamic resistance offered by both the main channel and a trap depend on the connection of these sections to additional traps or channels located downstream, designing a device to operate in a direct trapping mode must consider the entire fluidic resistance of the device. This information is especially necessary for understanding how to configure arrays of traps such that large networks of DIBs can be efficiently and quickly assembled in a microfluidic device. Thus, we develop a resistive circuit model that enables calculation of fluid flow rates and pressure drops between channel intersections for characterizing the direct trapping performance of a multiple-trap device.

For this analysis, we consider three configurations of trap arrays that include both parallel and serial arrangements of traps within a network (Figure 14A-C). In Model 1, the main channel connects the entrances to successive traps arranged in parallel before looping back to reconnect the outlets of each trap before exiting

the device—we refer to the main channel as “returning” to the traps before exit. The second model is similar to Model 1; however, there is no return path of the main channel. Instead a parallel channel that conducts between the exits of the traps and intersects the main channel at the end of the trap array is used to route excess oil flow away from the traps. Finally, Model 3 showcases a serial trap layout, where each trap has its own return path for excess oil that intersects the main channel prior to the next trap.

To enable sufficient comparisons of these layouts, values of channel resistances used in the modeling analysis are based on identical rectangular traps, each with a total width of 240 μm and a length of 130 μm, and using equal bleed valves that are 35 μm wide and 20 μm long. These dimensions reflect the approximate sizes need to capture a pair of 125 μm diameter droplets in a trap. Sections of main channel are assigned equal widths of 125 μm and all channels have a depth of 125 μm. These dimensions correspond to equivalent resistances of 770 Pa-s/μL and 1.3×10^3 Pa-s/μL for R_T and R_M, respectively.

To evaluate each layout, we write Kirchoff’s Current Law for fluid flow at each channel intersection in an array. This establishes a set of coupled equations as given by

$$[R]P = Q, \tag{7}$$

where [*R*] represents a square coefficient matrix of reciprocal hydrodynamic resistances (i.e. conductance values) between nodes, *P* is a column vector of unknown absolute pressures at each node, and *Q* is a column vector of known applied flow rates. Analysis is performed on arrays of up to 100 traps by developing the appropriate form of Equation 7 for each of the three array types and by applying a fixed input flow rate, Q_1, at the intersection of the main channel and the entry to trap 1. Solving these matrix equations thus allows us to compute the pressure distribution in the array (i.e. analogous to the voltage at each node)

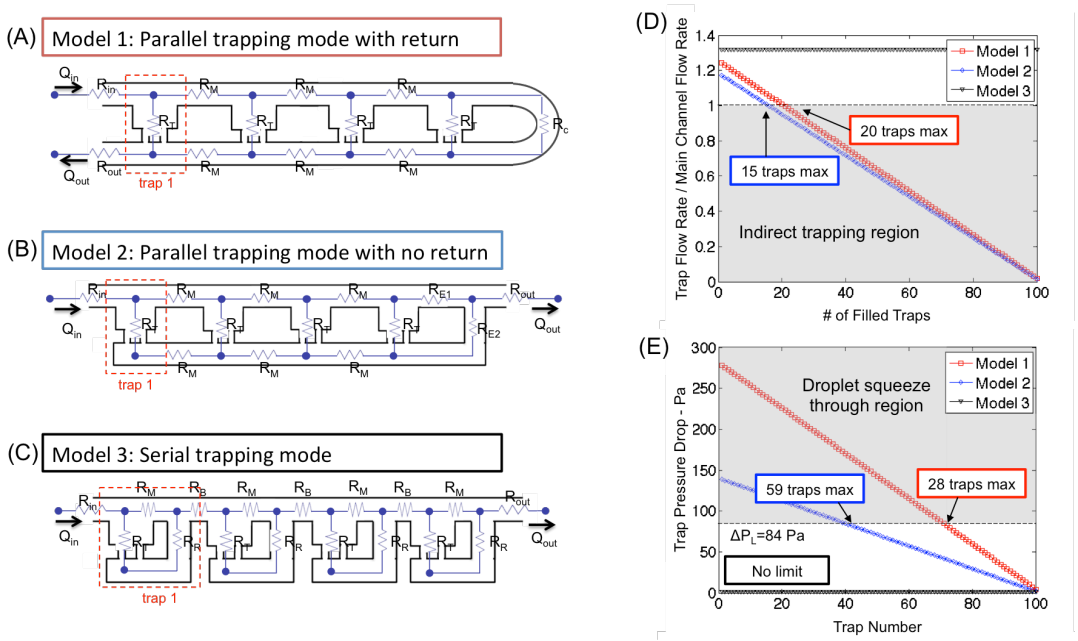

Figure 14. Schematics and equivalent circuits for three trap array layouts: (A) Model 1 includes a main channel that returns to connect every trap's bleed valves; (B) Model 2 features a lower channel that reconnects to the upper main channel at the end of the array; and (C) Model 3 includes an individual return line for each trap. (D) Calculated flow rate ratio through an empty trap versus the main channel as a 100-trap system is being filled. The unshaded region identifies when traps fill via direct trapping, while the shaded region identifies those filled via indirect trapping. (E) Estimated pressure drop within a filled trap versus location in the array, where the shaded region identifies locations in the array where droplets would be squeezed through the bleed valves due to excessive pressure.

and calculate for each trap in an array the ratio of fluid flow entering the trap to that which bypasses the trap, which allows us to determine if direct trapping occurs. These calculations are performed sequentially for a decreasing number of traps in an array to predict how changes in trapping mode and pressure distribution can arise from sequential trap filling. Recall that once a trap is filled, it acts like an open circuit, which thereby eliminates it from the circuit. Additional details regarding the general form of these matrix equations and sample MATLAB scripts for the three models are provided in Section A1 of the Appendix

The flow rate within each section of a multi-trap model is computed by dividing the difference in absolute pressure between nodes by the hydrodynamic resistance of that section. Figure 14D shows the ratio of flow rate entering the first trap of a section of successive unfilled traps to the flow rate bypassing that first trap. This calculation is performed sequentially by varying the number of filled traps in a 100-trap model. Therefore, the flow rate ratio reflects the preference of a droplet approaching the first unfilled trap to either enter the trap or bypass it. A ratio greater than one indicates direct trapping as marked by the unshaded region in Figure 14D. Only Model 3 provides constant direct trapping during complete filling of the 100-trap array. This result is due to the fact that the pathway exiting each trap rejoins the main channel prior to the next trap, which effectively decouples the ratio of R_T to R_M of a trap from the remaining portion of the array. Said differently, only the local channel geometry affects the resistance ratio, which ensures direct trapping is maintained across all traps. Model 1 and Model 2 also exhibit a flow rate ratio greater than one for small numbers of filled traps. However their ratios of flow rates decrease steadily as traps fill, caused by an increase in effective trap resistance that results when the number of unfilled traps in the array decreases (i.e. fewer traps in parallel produces a higher effective resistance of flow through traps). Figure 14D shows that the threshold for transitioning between direct and indirect trapping is 20 and 15 traps, respectively, for these two models.

The pressure drop across each trap is computed by determining the difference in absolute pressure between the entrance and exit nodes of the trap. This calculation is performed for all traps in a filled array to determine if droplet squeeze-through will occur (i.e. during filling of successive traps when the applied flow rate at the inlet is nonzero) for each model (Figure 14E). Arrays of filled traps are considered specifically since this condition represents the highest absolute pressure a system can experience and corresponds to when droplets could be squeezed through the bleed valves. The following comparison is based

on a filled array consisting of 100 equal traps, and the occurrence of squeeze-through is assessed when the pressure drop across a trap is higher than a Laplace pressure of 84 Pa (shown as the shaded region) determined using a droplet surface tension of 2 mN/m and trap and bleed valve widths of 130 μm and 35 μm, respectively.

This analysis shows that successive traps arranged in a parallel scheme (in Models 1 and 2) display linearly decreasing pressure drops with increasing trap number, where the first filled trap in a 100-trap array exhibits the highest pressure drop (275 Pa and 148 Pa, respectively) and the last filled trap exhibits the lowest pressure drop. Identifying where these two regressions cross the critical Laplace pressure of 84 Pa shows the maximum number (counting from the end of the series) of traps that can be configured in that way before squeeze-through occurs. For example, only the last 28 traps in Model 1 will not experience droplet squeeze-through the bleed valve—this result can be interpreted as a maximum of 28 traps arranged in parallel with a return (as shown by Model 1) can be assembled without squeeze-through occurring when all are filled. Model 2 exhibits a lower pressure profile, with the final 59 traps in the array being able to retain the captured droplets. However, in the serial model (Model 3), we find that the pressure drop across each trap in the series is equal (~1.5 Pa), which shows that the pressure across a filled trap is independent of the remaining number of filled traps, and far less than 84 Pa. Thus, while the absolute pressure at the inlet to a serial array does increase with increasing numbers of filled traps, the pressure across each trap is not large enough to cause squeeze-through. Therefore, based on the fact that direct trapping is maintained as traps are successively filled and that the pressure across filled traps will not cause squeeze-through, a microfluidic device with a serial trap layout is chosen to capture droplets and form DIBs in designated traps.

Production of droplets with uniform diameters and intra-droplet spacing is not instantaneous in a microfluidic device, often requiring several minutes of continuous injection to reach a steady state. Heterogeneous droplet production is problematic because hydrodynamic traps downstream can become filled with a variety of sizes and number of droplets, which complicates DIB formation and interrogation. Droplets much larger than the specified trap dimensions can also overfill the trap as well as clog the main channel, which disrupts the dynamics of droplet trapping downstream. Therefore, a pre-trap shunt can be implemented to remove undesired droplets from the array prior to droplet trapping. The shunt is designed such that when the shunt outlet is open, the shunt offers a lower hydrodynamic resistance (R_{Shunt}) than that of the trap array ($R_{TrapArray}$), which causes droplets to exit the device via the shunt instead of filling the trap array (Figure 15). Once droplets of desired size are obtained from the T-junction, the shunt outlet is manually sealed with tape, causing the droplet stream to now bypass the shunt and continue through the main channel to be trapped downstream.

3.3 Resistance based droplet sorting

Aqueous droplets are generated at a T-junction, where the width of the main

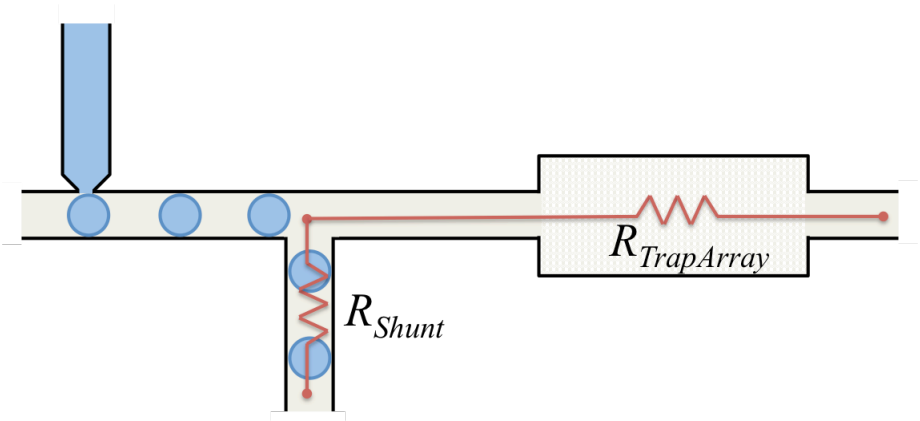

Figure 15. Schematic of droplets entering the shunt when shunt resistance, R_{shunt}, is less than resistance of total trap array, $R_{TrapArray}$, downstream.

channel for the continuous oil phase is 125 μm and the minimum width of the dispersed phase channel (buffer) is 30 μm. All channels in the fabricated device have a depth of 125 μm. With these fixed geometries, we can vary the average droplet diameter produced at the T-junction from 70-125 μm by varying the relative oil and water flow rates (see Figure A2). Flow rates of 0.4-1 μL/min for oil and 0.05-0.5 μL/min for aqueous phase are used to produce 90-125 μm diameter droplets, which is the target droplet size for the trap dimensions. The transient time required for the device to produce stable droplet sizes from the T-junction following a change in the applied flow rates is approximately 5-10 minutes.

From the T-junction, the droplet stream continues through the main channel to a point where droplets can either enter the shunt channel or continue through the main channel to the trap array as shown in Figure 16A. The fabricated shunt is 125 μm wide and 2.5 mm long, which yields a resistance of 4.2×10^3 Pa-s/μL from the intersection to the outlet. This value is an order of magnitude less than that offered by smallest total downstream resistance created by the 16-trap array, which has a value of 4.3×10^4 Pa-s/μL. Large droplets (i.e. slugs) are discarded through the outlet by keeping the shunt outlet open (Figure 16B). The shunt outlet is then sealed with tape to enable trapping droplets that are similar diameter to the width of the main channel (Figure 16C).

3.4 Hydrodynamic traps for droplet positioning and bilayer formation

Following the results of our circuit analysis, we fabricated microchips containing serial arrangements of either 16 or 40 identical hydrodynamic traps (Figure 16D). Like Model 3 in Figure 14C, the fabricated device features individual traps arranged in series, where the return channel for each trap re-enters the main channel at the entrance to the next trap (i.e. the value of R_m between traps is zero). However in the fabricated device, the serially connected traps are arranged in a zig-zag pattern rather than a linear arrangement to position more

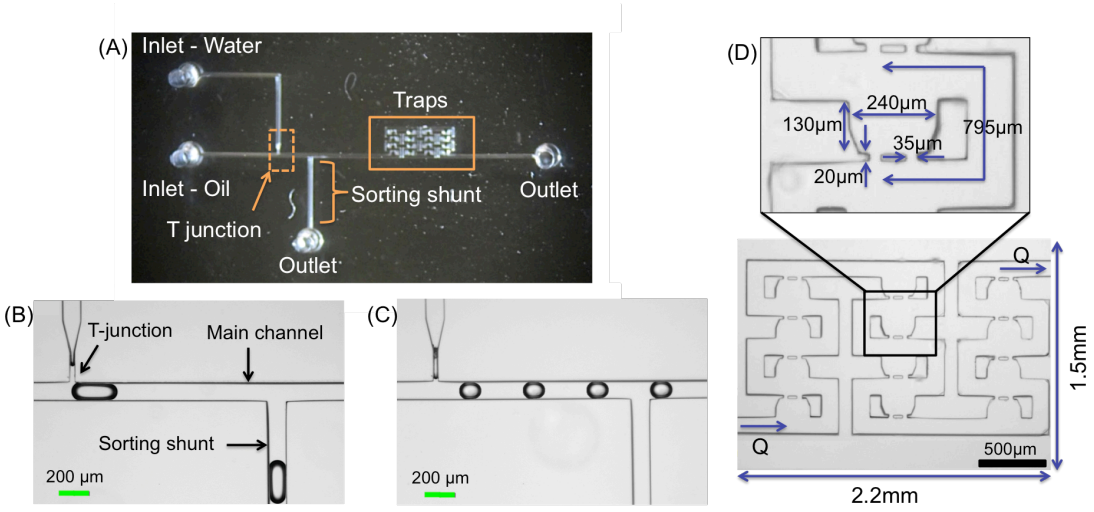

Figure 16. (A) Top view of fabricated microchip. (B) Image of T-junction and droplets entering the shunt channel when outlet is open. (C) Droplets bypass the shunt channel when shunt channel outlet is sealed. (D) Layout of the serial hydrodynamic trap array. Each trap is designed for 125 µm diameter droplets, and the dimensions satisfy the resistance ratio for direct trapping.

traps in the viewing area of our microscope. Based on these trap dimensions, the fluidic resistance of a single lane of an open trap, R_T, is computed to be 770 Pa-s/µL, versus a main channel resistance, R_M, of 1.1x10^3 Pa-s/µL. Since R_T<R_M, the fabricated devices are expected to exhibit direct trapping. Figure 17A-C confirms this behavior in a 16-trap microchip, by showing the sequence of filling events in which droplets enter traps sequentially. Additionally, we observe no droplet squeeze-through in either 16-trap or 40-trap devices, which confirms that the pressure drop across the traps remain less than the critical Laplace pressure of 84 Pa.

Microfluidic DIBs formed in this work are constructed from either glyceryl monooleate (GMO) lipids dissolved in the oil or 1,2-diphytanoyl-*sn*-glycero-3-phosphocholine (DPhPC) lipids incorporated as liposomes within the droplets. Both lipid types were found to yield stable DIB formation when the continuous phase is squalene, indicating that lipid monolayer assembly results in well-

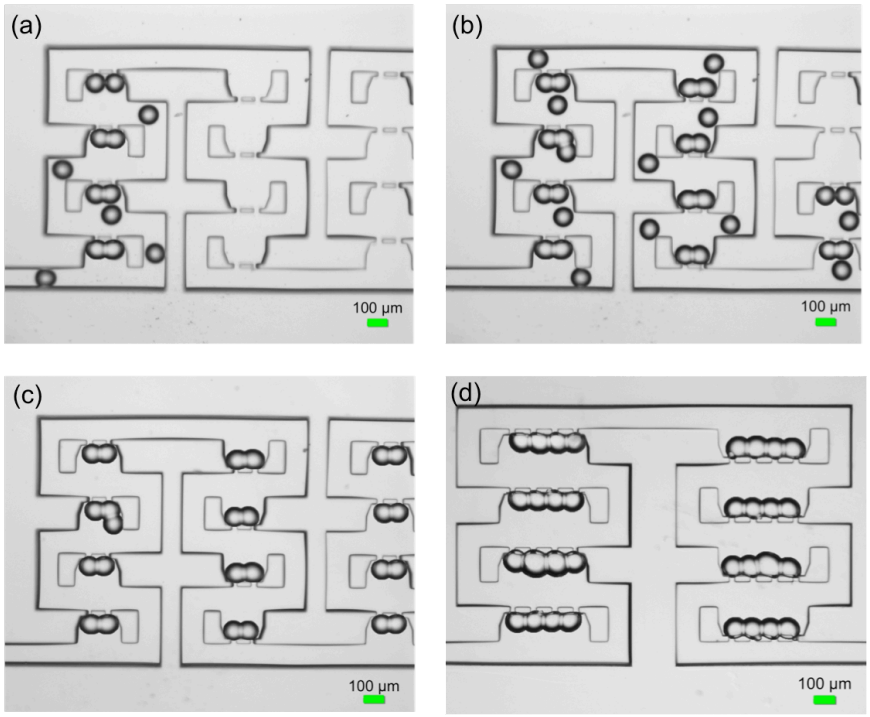

Figure 17. (A-C) Image sequence of GMO-coated droplets being trapped sequentially in designated locations with no droplet squeeze-through. (D) Hydrodynamic traps are expanded hold multi-bilayer networks such as four droplets linearly to form three bilayers.

packed monolayers around the droplets. Spontaneous bilayer formation between neighboring lipid-coated droplets in a trap is identified by the emergence of a bright, planar connection between adhered droplets. For instance, the droplet pairs in the three bottom leftmost traps in Figure 17A appear to have formed GMO bilayers, whereas the pair of droplets in the upper leftmost trap have not yet formed a bilayer since the dark outline of each droplet is still present. Successive images of the filling processing show that a droplet enters a trap every 1-2 seconds and DIBs form within 2-3 seconds of adjacent droplets landing in a trap. The entire capturing process takes less than 2 minutes to fill 16-40 traps. Further, images reveal that captured DIBs are stable within the device for up to 12 hours after assembly, and we observe very low rupture rates during or immediately after trap filling, which indicates that each droplet becomes well

coated with a lipid monolayer prior to entering a trap. Note that while a hydrodynamic pressure develops across each trap due to continued oil flow, this pressure is oriented parallel to the plane of the membrane. As a result, we do not believe continual oil flow to affect the stability of the membrane. However, any residual pressure-driven oil flow through the bleed valves of a filled-trap may also create a localized suction that pulls droplets together. Membrane rupture and droplet coalescence consistently occur after the 12-hour mark as a result of significant droplet shrinkage due to evaporation of water into the oil.[121, 122]

Over the course of 10 droplet trapping and DIB formation experiments on 40-trap devices (*n*=400 total traps analyzed), we observed that sequential droplet and DIB formation is highly reproducible. Specifically, the number of droplets captured in a trap matched the number of bleed valves (e.g. 2 droplets enters a trap with 2 bleed valves) in 95% of traps analyzed. The factors that led to a trap not containing the correct number of droplets include too low of an oil flow rate or too small of a droplet based on the trap dimensions. For instance, a third droplet may enter a two-droplet trap and form an additional bilayer if the oil flow rate is low (<0.4 μL/min) or if droplet diameters are <90 μm as seen in the second from the top, leftmost trap in Figure 17B,C. These conditions, along with a small amount of oil still flowing through the bleed valves of a filled trap, can allow for a successive droplet to “dip” into an occupied trap and potentially form an additional bilayer. Once droplets were captured, successful and stable DIB formation occurred in 94% of traps. The success rate was lower than 100% due to the fact that neighboring droplets occasionally coalesce to form a large single droplet within a trap. When this occurs, the single volume can block only one bleed valve, which allows a new incoming droplet to be filtered out of the stream and captured to form a new membrane interface, or block both bleed valves, such that the trap does not attract a new droplet to form a DIB.

The serial arrangement of hydrodynamic traps maintains direct trapping even as we increase the number of droplets and bilayers in each trap. Figure 17D shows an image of 8 traps in a 16-trap device where each trap has been expanded to capture more than two droplets to form serially connected DIB clusters. In this device, the main channel resistance is approximately $1.3x10^3$ Pa-s/μL compared to a single droplet lane trap resistance of 641 Pa-s/μL. Therefore, droplets entering multi-DIB traps maintain the same direct trapping mechanism as before and are captured sequentially. Also, the pressure drop across a four-droplet trap (~22 Pa) is still less than the critical Laplace pressure required to cause squeeze-through (Table 1).

3.5 Electrical characterization of DIB arrays

Incorporating Ag/AgCl thin-film electrodes onto the glass surface (Figure 18A) beneath the droplets provides a complementary method to imaging for characterizing DIBs and provides a more-efficient alternative to wire-type electrodes inserted into the microchannel.[70] Figure 18B shows the fabricated electrode pattern design where each hydrodynamic trap has two electrode pads, with one designated as the sensing electrode and one connected to ground. A common ground electrode is shared between all eight pairs and is pseudo-colored red in the image. Electrode pad placement is determined from imaging the positions of trapped droplets observed in prior experiments. The total

Table 1. Hydrodynamic resistances and pressures for empty and filled trap of 1 and 3 DIBs.

Scenario	R_T (Pa-s/μL)	R_M (Pa-s/μL)	Q (μL/min)	ΔP (Pa)
Empty trap - 1 DIB	770	$1.1x10^3$	1	7.6
Filled trap - 1 DIB	---	$1.1x10^3$	1	18.4
Empty trap - 3 DIB	641	$1.3x10^3$	1	7.17
Filled trap - 3 DIB	---	$1.3x10^3$	1	22

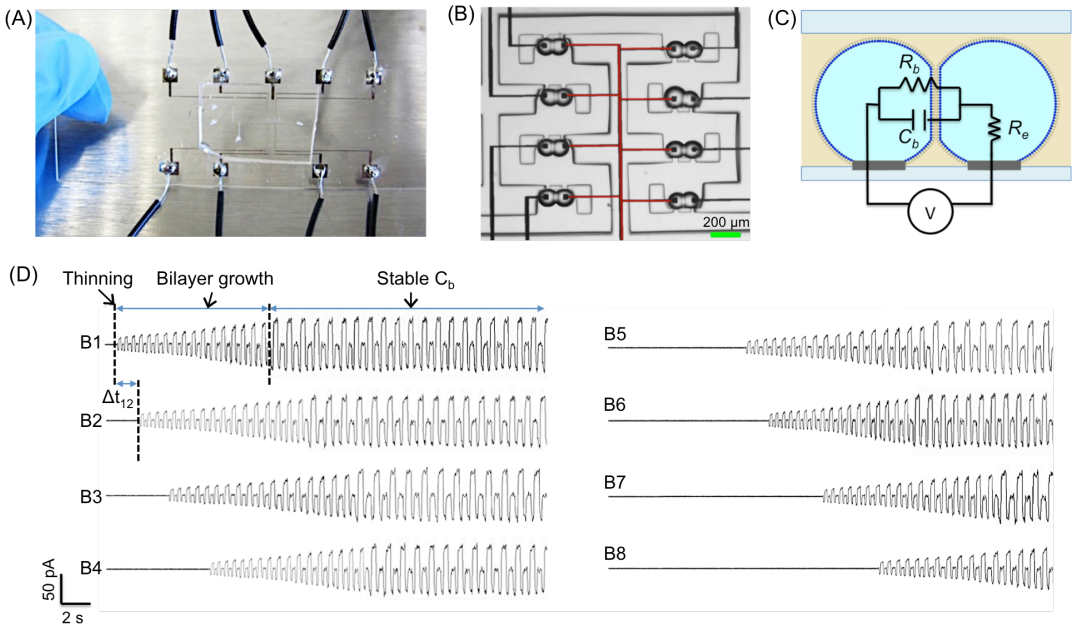

Figure 18. Electrical characterization of microfluidic GMO DIBs: (A) Top view of microchip with thin-film electrodes and soldered wires. (B) Image of DIB residing on top of thin-film electrodes. Sensing electrodes are those on the outer side, while the shared ground electrode in the middle is pseudo colored red. (C) Equivalent electrical circuit of a DIB on top of Ag/AgCl thin-film electrodes. (D) Current measurements of 8 DIBs measured concurrently show increases in current amplitudes that correspond to the growth in bilayer capacitances during DIB formation. Currents are induced by a 40 mV, 50 Hz triangular waveform voltage.

resistance of a single thin film electrode path is approximately 204 Ω from the droplet pad to connector pad where a cooper wire is soldered. In addition, we found the Ag/AgCl thin-film electrodes to be stable during experiments lasting up to 15 hours. During this time, there was no visual degradation when droplets containing 1 M NaCl reside on top of the electrodes.

Electrical measurements of adjoined droplets residing on a pair of electrode pads is used to characterize both the droplet-electrode interfaces as well as the membrane formed between droplets. The passive electrical properties of lipid bilayers are well established;[25, 123] the membrane is represented by a resistor, R_m, in parallel with a capacitor, C_m. An additional series resistance, R_e,

accounts for the electrolyte resistance of the aqueous phases on both side of the membrane (Figure 18C). The resistance of a lipid bilayer is often greater than 1 GΩ, while the electrolyte resistance is typically on the order of 1 kΩ. If the droplet-electrode interface is resistive (i.e. the electrode makes direct contact with the aqueous interior of the droplet), then the equivalent circuit shown in Figure 18C indicates that the dominant electrical impedance between two electrode pads is simply given by R_m and C_m. This condition implies that if the membrane fails (i.e. droplets coalesce), current flow between electrodes would increase significantly due to the lower value of R_e. However, if oil were to remain between the electrode pad and the droplet, then we expect a non-conductive, capacitance to exist at this interface (not shown in Figure 18C). In this case, a dc current would remain low upon coalescence because of the capacitive contact with the droplets. In this study, we find that droplets form resistive connections with the Ag/AgCl electrode pads when n-decane or squalene are used as the oil, which is confirmed by a saturation of measured current when a single aqueous volume spans two electrodes (not shown). However, capacitive connections are established when hexadecane is used as the oil phase. Since electrophysiology of membranes typically requires a resistive connection between the electrodes and the electrolyte, we perform electrical measurements of microfluidic DIBs in squalene. Squalene is also preferred because it is not absorbed by PDMS.

Membrane formation in a DIB array is assessed electrically by simultaneously measuring the currents induced by an equal triangular waveform voltage applied between each electrode pair. When droplets are adjacent but not yet adhered, the presence of oil between them causes the induced current to be less than the background noise. As a bilayer forms, the increase in membrane capacitance causes a square waveform current to appear and then increase in amplitude. This sequence reflects the initial thinning and subsequent areal growth of the bilayer between droplets.[124] Figure 18D shows electrical currents recorded during the spontaneous formation of 8 separate GMO DIBs (B1-B8). The 3-5

second time lag between onsets of successive DIB formation represents the time required for the next trap to fill and then a bilayer to form in that trap. Each membrane reaches a stable capacitance within ~10 seconds of the onset of thinning.

The raw current traces in Figure 18D are used to compute the nominal capacitance and resistance of the bilayer as described elsewhere.[32] In parallel to electrical recordings, DIB area is calculated from the projected length of contact between droplets, which is measured from images of the droplet pair (such as those in Figure 18B) using Image J software. This horizontal length of contact, or DIB lateral length,[33, 125] is assumed to be equal to the circular diameter of the interface. Table 2 shows the steady-state membrane properties obtained from a single experiment for 8 GMO DIBs formed using ~100 μm diameter droplets. Nominal capacitance and membrane resistance for an 8-DIB array are plotted versus time in Section S3 in the SI. From this experiment on 8 DIBs, the average membrane capacitance is 11.0±0.02 pF and the average membrane resistance is 8.3±0.3 GΩ. The image analysis shows that the average length of contact between droplets is 42.7±2.3 μm, yielding an average circular area of 1431±4 μm^2. Specific membrane capacitance is computed for each DIB by dividing C_m by DIB area. The average specific capacitance from the 8 DIBs formed in the microchip is 0.771±0.001 $\mu F/cm^2$, which is within the range of values of 0.75-0.81 $\mu F/cm^2$ found in literature for GMO in squalene.[126] Multiplying R_m by area yields an average membrane resistivity of 0.12±0.01 $M\Omega cm^2$, which is comparable to typical liquid-supported lipid bilayers.[20, 47]

The low standard deviation in membrane capacitance, resistance, and area within a set of 8 DIBs illustrates the uniformity of the droplets produced during a given experiment. However, multiple DIB array formation and electrical characterization experiments reveal that variations in average droplet size from one experiment to another are the primary cause for differences in nominal DIB

properties between separate trials. For example, the average bilayer areas computed from two additional experiments (each using measurements from 8 GMO DIBs) are 2176±4 μm^2 and 1671±9 μm^2, respectively (Table 2). The droplet sizes were ~125 μm and ~110 μm in diameter, respectively. However, the average values of specific capacitance and membrane resistivity for DIBs formed in the three trials shown are very similar, which indicates that DIBs formed in the device exhibit consistent values of thickness and permeability from one experiment to the next. Tables providing individual bilayer properties from these additional trials are presented in section S4 of the Appendix .

3.6 Parallel single channel recordings

Alamethicin peptides, which exhibit concentration- and voltage-dependent pore formation in membranes,[83] are incorporated into the aqueous droplets to demonstrate parallel single-channel recordings in multiple DIBs using the thin-

Table 2. Capacitance, resistance, area, specific capacitance, and normalized resistance for GMO DIBs obtained during three separate trials.

	DIB #	Capacitance final (C_F) – pF	Resistance final (R_F) – GΩ	Area final (A_F) – μm^2	Specific capacitance (C_M) - $\mu F/cm^2$	Normalized resistance (R_N) - $M\Omega \cdot cm^2$
Trial 1	Pair 1	11.0	8.1	1425	0.772	0.12
	Pair 2	11.0	8.8	1432	0.770	0.13
	Pair 3	11.0	8.0	1432	0.771	0.12
	Pair 4	11.0	8.1	1432	0.771	0.12
	Pair 5	11.0	8.1	1432	0.770	0.12
	Pair 6	11.1	8.8	1432	0.772	0.13
	Pair 7	11.0	8.2	1425	0.772	0.12
	Pair 8	11.1	8.1	1438	0.769	0.12
	Averages	11.0±0.02	8.3±0.3	1431±4	0.771±0.001	0.12±0.01
Trial 2	Averages	16.7±0.05	8.1±0.2	2176±4	0.769±0.001	0.18±0.004
Trial 3	Averages	12.9±0.13	8.3±0.4	1671±9	0.773±0.003	0.14±0.01

film electrodes. Voltage-induced gating is recorded with +170 mV applied equally across all 8 DPhPC DIBs; we found this level necessary to elicit pore formation for a final peptide concentration of 1 μM in the droplets. Simultaneous recordings of the resulting currents from all 8 DIBs are shown in Figure 19A. For each membrane, we observe that the current stochastically fluctuates between discrete levels, which signifies transient pore formation and closure caused by peptides in the membrane.[127] Figure 19B,C shows the calculated conductance versus time for one of the measurement channels (i.e. one of the DIBs). The ratios of alamethicin pore conductance relative to the subconductance level are found to be 1, 4.18, 8.73, and 14.07. These values are consistent with previous measurements of alamethicin activity in single DIBs.[47, 68, 128, 129] However, this platform provides for the first time a reproducible and high throughput microfluidic method to simultaneously measure single-channel gating responses in multiple DIBs.

In the lipid-in[130] DIB technique used herein, liposomes contained within the

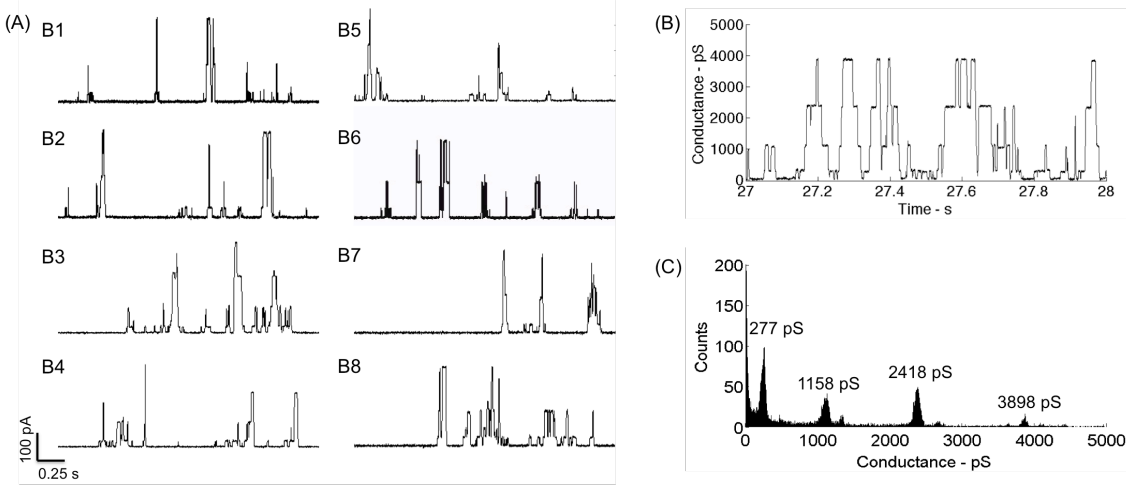

Figure 19. (A) Simultaneous recordings of alamethicin gating activity in 8 DPhPC DIBs at a holding potential of +170 mV. (B) Conductance versus time of a single measurement channel. (C) Histogram of conductance values for alamethicin channels computed from the multiple gating events in (B).

droplets must fuse at the oil-water interface to form a monolayer prior to bilayer formation between droplets. Therefore while vesicle fusion after membrane formation is one way that alamethicin peptides reach the bilayer, it is highly likely that many alamethicin peptides are pre-associated with the monolayers coating the droplets prior to DIB formation. Our experiments with alamethicin consistently show immediate voltage-dependent ion channel formation after bilayer formation, which supports the notion that peptides are present on the membrane surface when the membrane forms.

Nonetheless, our microfluidic system to assemble and interrogate arrays of DIBs is equally well suited for lipid-out DIB formation, in which the lipids are incorporated outside of the droplets in the oil. Placing lipids in the oil ensures that the only bilayer membranes in the system are those that separate adjoined droplets. Further, incorporating the lipids in a separate phase from transmembrane proteins or other water-soluble species provides more control over the interactions between these species and the membrane[131, 132] and enables easier application of osmotic gradients,[133, 134] since the interiors of the droplets do not contain an excess of liposomes or proteoliposomes.

3.7 Chapter summary and conclusions

In this work, we designed and fabricated microfluidic devices developed to generate, sort, and trap droplets to form DIBs in designated traps. Specifically, hydrodynamic traps were designed using an equivalent circuit model to capture two, three, or four droplets to form either single bilayers or serially connected multi-DIB clusters in each trap. Through the circuit modeling analysis, we were able to design multiple-trap arrays that enable sequential droplet trapping and subsequent DIB formation between multiple pairs of droplets in a single device. The chosen serial configuration provides a constant, low-pressure drop across each filled trap, which is far less than the Laplace pressure across a droplet. Therefore, captured droplets are retained and are not pushed through the bleed

valves after trapping. Trapping order will be especially important in future work, where captured droplets of alternating compositions are desired. In contrast, our analysis of multi-trap arrays that feature traps arranged in a parallel fashion did not fulfill the maximum pressure and direct trapping criteria, which placed limits on the number of traps that could be included within a device. Hence, these designs were not fabricated.

We demonstrated the incorporation of thin-film electrodes and *in situ* electrical interrogation of multiple DIBs within an enclosed device. We used these conductive traces to simultaneously apply a voltage stimulus and measure the resulting currents through as many as 8 DIBs. Combined electrical and optical access allowed for measurements of membrane capacitance, resistance, and bilayer area for each DIB, and our experiments revealed that arrays of DIBs formed from a droplet stream exhibit consistent sizes and values of membrane resistivity. Also, parallel single channel recordings of alamethicin peptides were obtained via the thin-film electrodes in 8 DIBs at once. This capability for simultaneous electrical measurement in multiple DIBs supports the use of microfluidics and DIBs for high-throughput, low-volume electrophysiology experiments related to studying proteins, performing biosensing, and conducting drug-screening assays.

CHAPTER 4
ASYMMETRIC DROPLET INTERFACE BILAYERS WITH *IN SITU* ELECTRICAL MEASUREMENTS

In this chapter[2] we address Objective 3 as a step towards understanding the effects of peptides on the disruption of asymmetric lipid membranes and intramembrane potential, which are not well known due to technical challenges in both assembling and characterizing the asymmetry of lipid membranes. Therefore as part of Objective 3, we incorporated a method to generate alternating droplets to form asymmetric DIBS in the microfluidic device from Objective 1&2. Then through thin-film electrodes, we are able to electrically characterize the intramembrane potential between bilayers containing asymmetric zwitterionic phospholipid leaflets (i.e. DPhPC and DOPhPC). This *in situ* measurement technique is applied an array of asymmetric DIBs to study lipid asymmetry versus time and in the presence of peptides.

Here, we present a novel microfluidic platform capable of generating a stream of alternating droplet compositions, i.e. A-B-A-B, and sequentially capturing these droplets in precise locations to enable the spontaneous formation of synthetic lipid bilayers between droplets of different compositions (i.e. A and B) in an enclosed substrate. This platform preserves a key feature of the droplet interface bilayer method, which allows asymmetric conditions within and across the membrane to be prescribed by simply using droplets containing different species.

---

[2] Note: A version of this chapter was originally published by Nguyen, M., and Sarles, S.A., Microfluidic Generation, Encapsulation and Characterization of Asymmetric Droplet Interface Bilayers. ASME Conference Proceedings 2016 – Conference on Smart Materials, Adaptive Structures and Intelligent Systems, Stowe, VT, September 28-30, 2016.

In this work, we demonstrate the ability to assemble bilayers consisting of asymmetric lipid compositions and, separately, show that alternating droplets containing the same lipid type can also be used to control the direction of ion channel insertion. In the first study, A and B droplet types contain liposomes comprised of different lipid types, which are used to establish an asymmetric composition of the leaflets that make up the lipid bilayer. This asymmetry results in a dc, non-zero membrane potential, which we measure via membrane capacitance versus bias voltage. Also, alamethicin peptides are included in only one of the droplet types, which enable voltage-dependent insertion to occur only at one polarity. Cyclic voltammetry measurements are performed to confirm the direction of insertion of alamethicin channels in bilayers. Also, these results show the ability to perform simultaneously electrical measurements on multiple DIB, which increases the experimental capacity and efficiency of a microfluidic approach. The ability to produce alternating droplets in a high throughput manner with electrical access provides a system to investigate the effects of lipid asymmetry on the function of membrane proteins in a controlled model system.

4.1 Introduction

By targeting properties of live cells found in nature, we can continue to improve synthetic material systems. For instance, cell membranes are asymmetric where the content on one side of the bilayer is different from the other and the lipids of the membrane itself differ from the inner and outer leaflets. One example is the plasma membranes of eukaryotic cells where aminophospholipids are primarily in the cytosolic leaflet while phosphatidylcholine and sphingomyelin dominate in the outer leaflet [71]. Implementing asymmetric lipid bilayers creates a more biological relevant model systems, and it enables the addition of a “sidedness” to the system.

So far we have developed a device capable using hydrodynamic trapping method to capture droplets from a moving stream and housed in a precise

location. While efficient, this system lacks the ability to prescribe droplets of different compositions for each DIB, which limits the use of these assemblies for processes that specifically require asymmetric conditions such as transmembrane proteins inserted in only one direction, the presence of a salt concentration difference, or the ability to pump species in one direction.

Here, we integrate opposing T-junction droplet generators [135] to enable the formation and characterization of asymmetric DIBs between droplets of alternating composition. Our revised device utilizes the previously designed hydrodynamic traps to form DIBs and thin-film surface electrodes beneath each trap to measure transmembrane ion currents *in situ* in multi-DIBs [136]. In place of symmetric droplet compositions, we believe utilizing asymmetric compositions of the droplets and leaflets that make up the bilayer will enhance their use for sensing and membrane-mediated processes studies, where the introduction of species on a specific side of the membrane is often required. To confirm the asymmetry of trapped droplets, we use alternating droplet production to produce asymmetric lipid bilayers comprised of different lipids in each leaflet and, separately, we demonstrate the ability to control the direction of insertion of voltage-dependent ion channels formed by alamethicin peptides added to only one droplet in each pair.

4.2 Alternating droplet generation and capture

We fabricated a PDMS microchip featuring two, directly-opposed T-junctions to produce binary streams of aqueous droplets of alternating compositions as shown in Figure 20A. The oil-filled main channel is 125 μm wide and the two T-junctions are 40 μm at their exits. All channels have a depth of 125 μm. The flow rates to produce 90-120 μm diameter droplets and create alternating droplets range from 0.4-1 μL/min for oil and 0.05-0.5 μL/min for the aqueous phases. The flow conditions required to form a steady flow of alternating droplets in a microchannel are characterized as a function of the capillary number, C_a, and

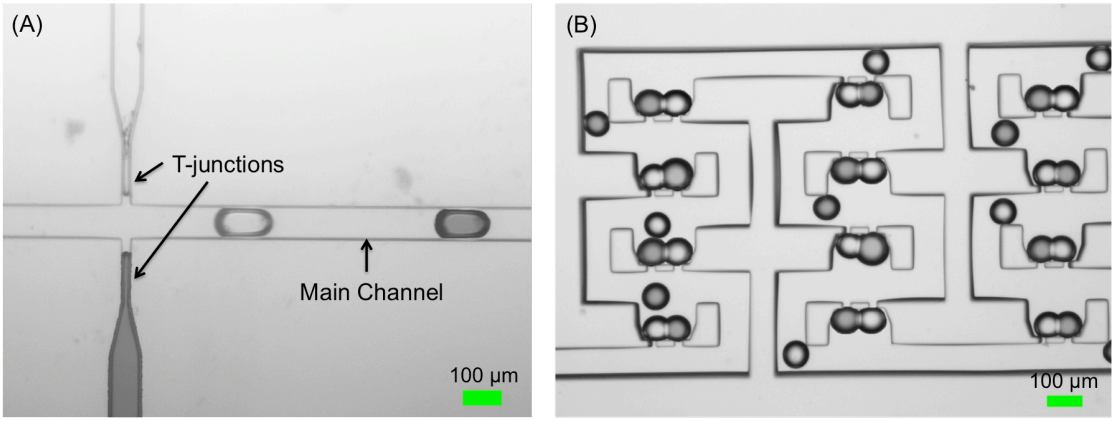

Figure 20. (A) Two opposing T-junctions producing droplet stream of alternating compositions. Food coloring is used to distinguish between to aqueous fluids. (B) Trapped asymmetric DIBs.

water fraction, w_f [135]. The capillary number is a measurement of viscous stress relative to the interfacial tension stress, such that

$$C_a = \frac{U\mu}{\gamma}, \tag{8}$$

where U and μ are the flow velocity and dynamic viscosity, respectively of the oil and γ is the surface tension at the interface between the aqueous droplet and the oil. The water fraction is computed as the ratio of the combined aqueous solutions flow rates to the total flow rate of the oil and aqueous phases, given by

$$w_f = \frac{Q_{Aqueous}}{Q_{Total}}. \tag{9}$$

A continuous stream of alternating droplets is produced from the opposing T-junctions when both C_a and w_f are in appropriate ranges. A prior study demonstrated alternating water droplet production in fluorinated oils for C_a between 0.001 and 0.05 and w_f between 0.2 and 0.8 [135]. Our experiments at varying oil and water flow rates confirm that alternating droplets are produced at C_a values as low as 0.002 and as high as 0.04 and w_f values between 0.4 and 0.8. Using values of 12 cP and 1.2 mN/m, respectively for the viscosity of squalene and the surface tension of a squalene-water interface decorated with

lipids [137], the water and oil flow rates mentioned for generating alternating droplets 90-120 μm in diameter correspond to a C_a value of 0.005 and a w_f value of 0.6.

Within the working range of droplet production, increasing the water fraction of the total fluid increases the droplet size and decreases the distance between adjacent droplets in the stream. Stable alternating droplets are produced at low water fractions (<0.8). When C_a is too low, aqueous volumes are dispensed from the opposing junctions at the same time and they coalesce upon exiting. Conversely, when C_a is too high, the junctions generate continuous streams rather than discrete droplets. Furthermore, when the water fraction is too high (>0.8), it is difficult to form stable alternating droplet regardless of the capillary number due to laminar aqueous flow that results in a single continuous stream.

Alternating droplets are routed to and captured sequentially by a series of hydrodynamic traps. The traps in the device were the same design as previously described above to ensure direct trapping of droplets during the filling of all traps, which is necessary to maintain the alternating arrangements, and to prevent droplets from squeezing through the bleed valves once trapped [136]. Figure 20B shows a DIB formed between two different aqueous droplets in each trap. This result and the observation that the stream of droplets bypassing the traps is alternating in composition confirm that droplet production is alternating and droplet trapping occurs sequentially. While the prototype devices fabricated for this study have 16 traps, our equivalent-circuit model [136] predicts that direct trapping in serial layout of traps can work for any number of traps. Thus, we believe this approach can be applied to generate hundreds to thousands of DIBs in a compact device.

4.3 Asymmetric lipid composition characterization

With the capability of forming asymmetric DIBs on a microfluidic platform, we are able to investigate leaflet asymmetry by incorporating different liposome compositions within each aqueous inlet. Specifically, one aqueous solution contains DPhPC liposomes, while the second aqueous solution contains liposomes consisting of DOPhPC, an ether form of the same synthetic lipid. Captured pairs of alternating droplets containing different liposomes will become encased in their monolayers of different composition and result in asymmetric DIB membranes with different leaflet compositions, as was shown previously with a non-microfluidic approach [34]. Even though both lipids used herein are zwitterionic (i.e. zero net headgroup charge) and have similar chemical structures, they exhibit different values of dipole potential, a quantity that is dependent on the area per lipid molecule in the monolayer. Specifically, Yasmann, et al. showed that DPhPC has a dipole potential of ~350 mV and DOPhPC exhibits a dipole potential of ~200 mV when both the lipids in both monolayers are maximally packed (i.e. minimum area per lipid) [138]. As a result of the difference in dipole potential, an asymmetric membrane exhibits a non-zero potential difference equal to the difference in magnitudes of dipole potential [80]. For the two lipids considered here, an asymmetric DPhPC-DOPhPC membrane should exhibit a +135 mV potential with respect to the leaflet containing DPhPC. To confirm the asymmetry that is established when a DPhPC- coated droplet attaches to a DOPhPC droplet, measurements of membrane capacitance, C, versus DC bias, V, are performed to quantify the net membrane potential, V_r, as given by the following relationship [139]:

$$C = C_0(1 + \alpha(V + V_r)^2) \quad (10)$$

In this expression, C_0 represents the membrane capacitance at $V = 0$, and α is the fractional increase in capacitance per square volt due to electrowetting [140, 141]. Equation 10 shows that membrane capacitance is a quadratic function of the applied voltage, which reaches a minimum at $V = -V_r$.

Here, asymmetric DPhPC-DOPhPC lipid bilayers are formed using the alternating droplet generation technique and capture methods described above to form 16 asymmetric DPhPC-DOPhPC lipid bilayers in a device. Due to limitations in the number of independent current measurement channels offered by the 8-channel Tecella amplifier, electrical interrogation is performed on the 8 DIBs residing on surface electrodes (Figure 21). The electrodes are patterned such that each hydrodynamic trap has two electrode pads, one connected to the sensing input of a channel on the amplifier and the other to signal ground. A common ground electrode is shared between all eight pairs and is pseudo-colored red in the image. After the droplets land in each trap and a bilayer spontaneously forms between them, a 40 mV, 50 Hz triangular waveform voltage is applied to record the capacitive current induced by the formation of the membrane [32, 136]. To determine the membrane potential for an asymmetric DIB, an applied dc offset is added to the triangle wave voltage and it is increased in a step-wise fashion at a rate of 10 mV at every 20 seconds until the bias reaches 290 mV. The procedure enables membrane capacitance at each dc

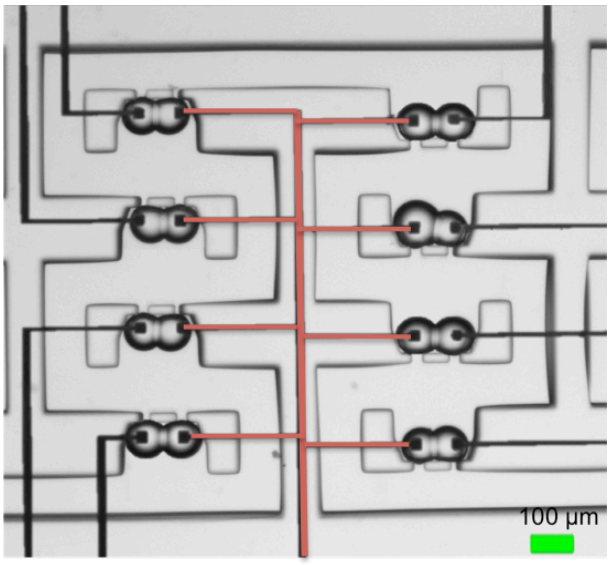

Figure 21. Captured asymmetric DIBs on top of thin-film electrodes. Sensing electrodes are on the outer side while the ground is in the middle pseudo colored red.

voltage step to be calculated from the induced square wave current [32].

Representative capacitance data for two of the eight asymmetric DIBs are plotted in Figure 22 to illustrate the offset of the location of minimum capacitance due to membrane asymmetry resulting from binary droplet compositions. In comparison, measurements of capacitance versus voltage for a symmetric DPhPC DIB obtained using manual methods for droplet formation and positioning are also shown. Unlike a symmetric DIB that exhibits a zero membrane potential, our measurements confirm that DIBs constructed from monolayers of different lipid types result in a non-zero membrane potential. Specifically, we find that there is a ~137 mV difference for asymmetric DIB membranes formed with DPhPC and DOPhPC, which is consistent with other reported experimental values [80, 138]

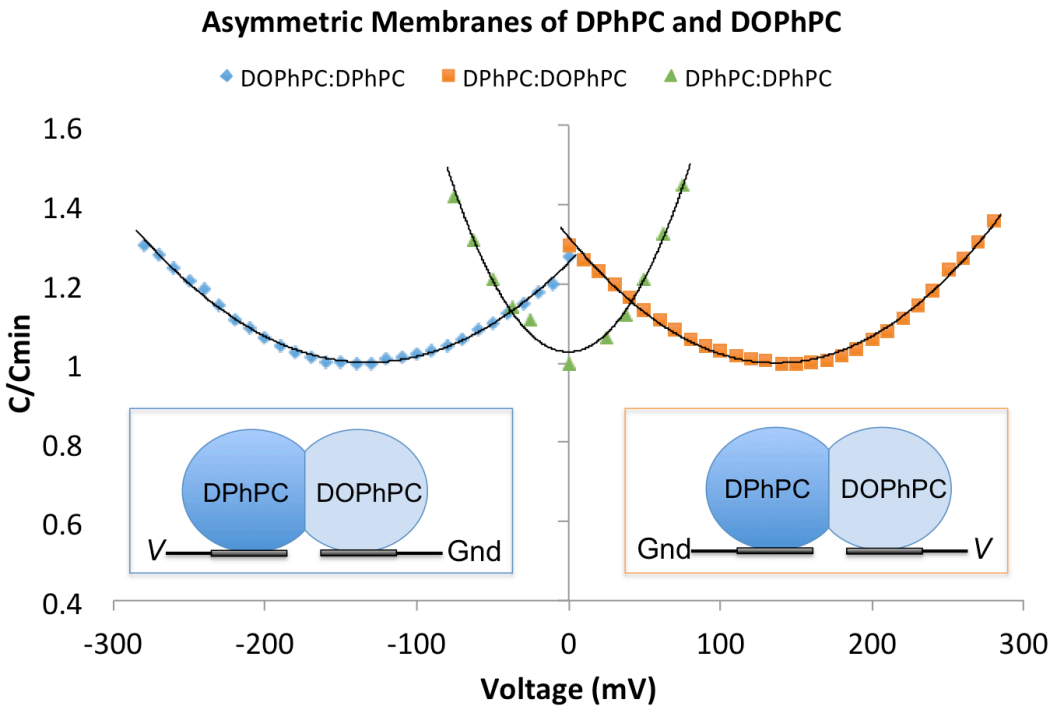

Figure 22. Current plotted for two different pairs of DIBs as a function of voltage for asymmetric membranes of DPhPC and DOPhPC. Inset schematics illustrate the location of the lipids based on the transmembrane potential offset. A symmetric DPhPC case is included for comparison.

and close to the dipole potential difference. Table 3 summarizes the transmembrane potentials measured for each of the eight DIB pairs interrogated simultaneously during the same experiment.

In addition to determining the magnitude of each membrane's potential, we are also able to determine which lipid is on which side of a particular DIB by considering the polarity of the voltage where minimum capacitance occurs relative to the position of the sensing and ground electrodes in the device. For example, a positive transmembrane potential (i.e. which corresponds to minimum capacitance at a negative voltage of each magnitude) suggests that the droplet resting on the ground electrode contains DOPhPC liposomes, while the droplet on the sensing electrode contains DPhPC liposomes (shown in the left inset in Figure 22). Since the polarity of the membrane potential alternates, these results of an 8 DIB array in Table 3 also illustrate that in our device, the arrangements of DIBs formed between alternating droplets alternate with respect to the sensing and ground electrodes. In summary, these results showcase that a microfluidic approach can be used to increasing the experimental output and efficiency for studying asymmetric membranes formed with alternating droplet compositions.

Table 3. Calculated transmembrane potentials for eight DIBs and locations of the lipids.

Pair #	Transmembrane potential (mV)	Lipid on ground electrode	Lipid on sensing electrode
DIB 1	+137	DOPhPC	DPhPC
DIB 2	-137	DPhPC	DOPhPC
DIB 3	+137	DOPhPC	DPhPC
DIB 4	-137	DPhPC	DOPhPC
DIB 5	+137	DOPhPC	DPhPC
DIB 6	-137	DPhPC	DOPhPC
DIB 7	+137	DOPhPC	DPhPC
DIB 8	-137	DPhPC	DOPhPC

4.4 Asymmetric transduction measurements in symmetric DIBs

Alamethicin peptides are incorporated into one of the aqueous channels such that symmetric DPhPC DIBs are formed between one droplet with peptides and one without. This alternating placement of peptides should lead to one-side interactions between the membrane and the peptides. In particular, alamethicin peptides induce voltage-dependent current upon directional pore formation in the bilayer at transmembrane voltages greater than ~+70 mV with respect to the side of insertion [142]. Thus, we expect that pore-formation will only occur at a single polarity in each membrane, the sign of which depends on the position of the droplet containing peptides on the sensing and ground electrodes.

Figure 23 shows simultaneous current measurements for four of the eight membrane containing alamethicin. In each trace, the current signal stochastically fluctuates between discrete levels signifying pore formation and closure [127]. Here, these gating events occur at +170 mV due to the fact that the droplets containing alamethicin in each of these DIBs are residing on sensing electrodes. While not shown, channel formation activity is only observed at -170 mV for the other four DIBs, where alamethicin is contained in the droplet resting on the ground electrode.

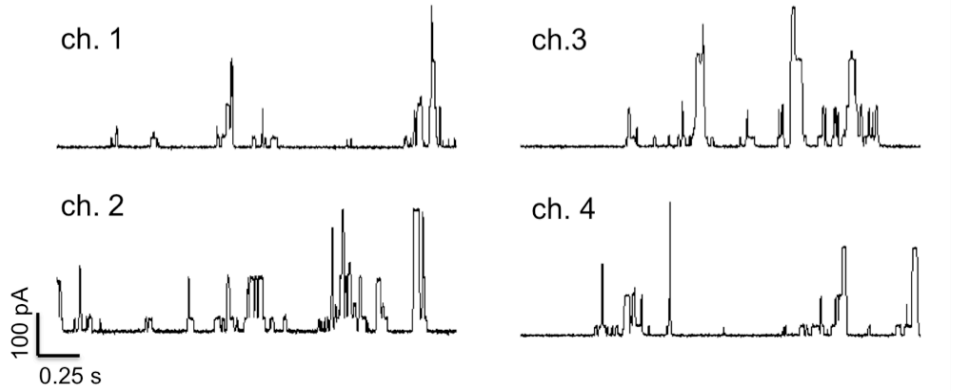

Figure 23. Simultaneous recording of alamethicin ion channel activity in 4 different DIBs with a holding potential at +170 mV.

The sided-ness of alamethicin pore formation is also demonstrated through cyclic voltammetry (CV) measurements as shown in Figure 24. During this measurement, the current through the membrane is recorded as the voltage is cycled across a range of values. The voltage in this CV sweep begins at 0 mV, increases at a constant rate of 10 mV/sec to +170 mV then decreases at the same rate to -170 mV, ending back at 0 mV. The measurement plotted in Figure 5b shows that the current exhibits an exponential increase at positive voltages above ~100 mV, which confirms that that alamethicin inserts in the bilayer only from one side of the membrane and suggests that the droplet residing on the sensing electrode contains alamethicin. Because there is no current activity during the negative voltages of the CV sweep, we can assume there is no alamethicin present in other droplet. Similar to the alternating values of membrane potential for asymmetric DIBs, increases in membrane current at the opposite polarity are observed when the position of the alamethicin droplet is switched to the ground electrode. For instance when droplets with alamethicin is on the ground electrode, there is gating activity at negative voltages and no current present at positive voltages. This further demonstrates the traps captured

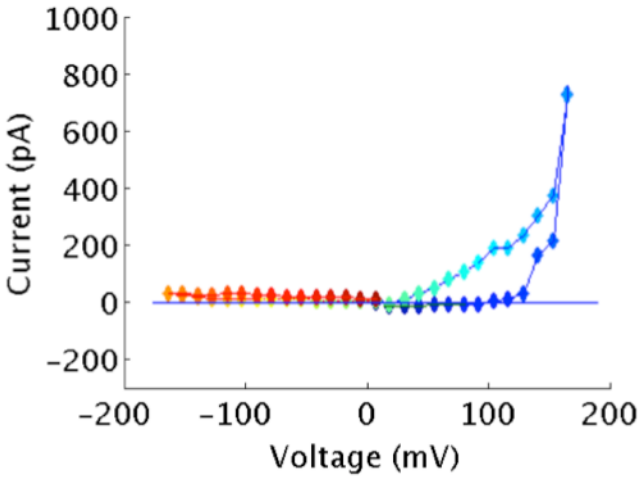

Figure 24. Current voltage sweep response when DC step routine is applied for one DIB pair. The color shows the order of the cycle beginning with the blue and ending with red. The connecting line is included to identify the trend.

asymmetric DIBs.

4.5 Asymmetric membrane with alamethicin

In this study we monitored the intramembrane potential over a period of hours. Figure 25 shows the summary of different combinations of phospholipid leaflet compositions and alamethicin exposure. For the case of DPhPC-DOPhPC asymmetric membranes without alamethicin, we observed no change in the measured membrane potential of 137±1 mV over the course of 15 hours. Where as for symmetric membranes of DPhPC, the bilayer exhibits 0 mV. In experiments with alamethicin in asymmetric bilayers, the initial intramembrane potential after bilayer formation is the same as if there was no alamethicin present, exhibiting a 137±2 mV potential difference. However, the membrane

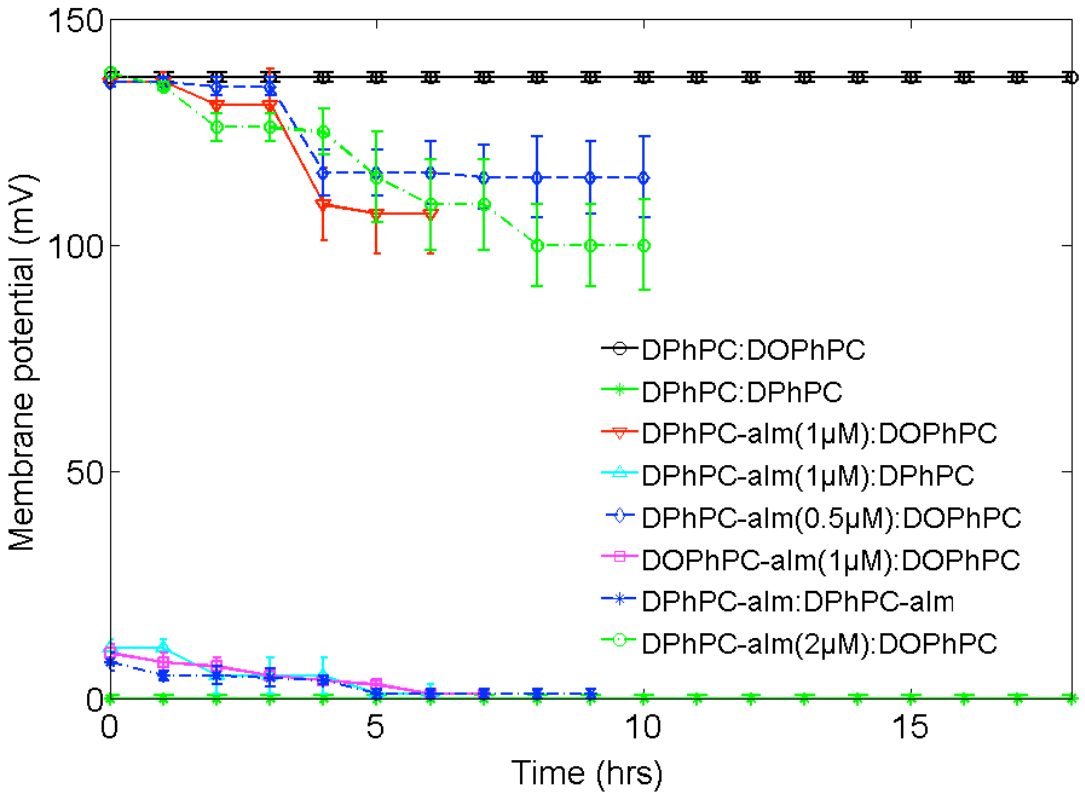

Figure 25. Average membrane potential versus time. Error bars represent the standard deviation of 40 DIBS between 5 trials of 8 DIBs.

potential begins to decrease after the first hour. This decrease shows that the difference in dipole potential for the two leaflets is reduced—possibly by lipid translocation. Our measurements also show that the concentration of alamethicin affects the membrane potential over time. When there is 2 μM of alamethicin on the DPhPC side of the membrane, the potential difference is approximately 100±10 mV after 10 hours. In the same scenario with 500 nM of alamethicin, the membrane exhibits approximately 115±9 mV after 10 hours. In addition, we examined symmetric phospholipid leaflet bilayers exposed to alamethicin. The symmetric bilayer experienced a membrane potential of approximately 8±2 mV in the first hour. However over time, the potential equilibrates to 1±1 mV after 5 hours. The symmetric bilayer measurement with alamethicin suggests that the peptide disrupts the membrane initially.

A series of CV measurements were performed to determine the threshold voltage needed to drive alamethicin insertion [129] in symmetric and asymmetric DIBs. CV scans enable repeatable and reliable measurements of V^*, which can then be

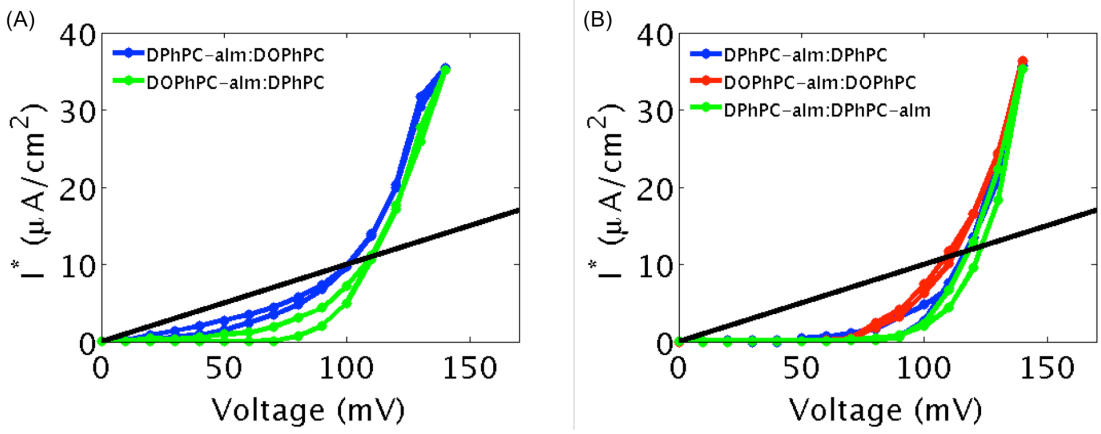

Figure 26. Cyclic voltammetry curves. The current response is normalized by membrane area for each scan and plotted versus voltage (mV). (A) Normalized current for asymmetric leaflet of DPhPC and DOPhPC with alamethicin on one the sensing side of the membrane. (B) Normalized current for symmetric DPhPC membranes with alamethicin and symmetric DOPhPC bilayers with alamethicin. The black line is the selected specific conductance of 100 μS/cm^2.

further analyzed to determine parameters influencing peptide insertion. Figure 26 shows representative current-voltage (I-V) curves from DIBs exposed to 1 μM of alamethicin. Note that current is normalized by membrane area. As voltage increase during a CV sweep – during a given DIB composition – current remains close to zero until the increasing voltage approaches *V**. Once the voltage exceeds the threshold for peptide insertion, the current increases exponentially with respect to voltage as the membrane is populated by peptide-stabilized pores. The shifting of an *I-V* curve to the left in Figure 26 indicates that peptide insertion is more favorable since it occurs at a lower voltage. Figure 26A and Figure 26B are separated based on asymmetric and symmetric leaflet, respectively. Table 4 shows the voltage threshold values based on a specific conductance of 100 μS/cm^2, which corresponds to the intersection point of the black line and the I-V curve. Overall, symmetric DPhPC DIBs with alamethicin on both sides of the bilayer exhibits the highest voltage threshold of 123 mV. Asymmetric DIBs with alamethicin on the DPhPC side have the lowest voltage threshold of 101 mV, a difference of 22 mV. This shows that less voltage needs to be applied for alamethicin to insert and gate. The low voltage threshold indicates that the membrane potential of asymmetric DIBs participates in peptide insertion.

4.5.1 Discussion of alamethicin on symmetric and asymmetric membranes

For both DPhPC and DOPhPC symmetric bilayers, there is a non-zero and time

Table 4: Voltage thresholds for symmetric and asymmetric membranes with alamethicin.

DIB composition	Voltage threshold (mv) @ 100 μS/cm^2	Relative voltage difference (mV) to DPhPC-alm:DPhPC-alm
DPhPC-alm:DPhPC-alm	123	0
DPhPC-alm:DPhPC	117	-6
DOPhPC-alm: DOPhPC	111	-12
DPhPC-alm: DOPhPC	101	-22
DOPhPC-alm: DPhPC	110	-13

dependent intramembrane potential (Figure 25) seemingly due to the presence of alamethicin. These results suggest that alamethicin affects either dipole or surface potential, or both. Also, we observe the voltage threshold for alamethicin insertion into symmetric bilayers is lower for leaflets comprised of DOPhPC (~110 mV) than for DPhPC membranes. The smaller voltage threshold suggests that there is a lower energy barrier for peptide insertion with DOPhPC lipids. Additionally, current measurements of alamethicin insertion into DPhPC membranes reveals that the voltage threshold is lower when alamethicin is introduced on only one side of the bilayer (~117 mV) compared to an equal concentation of peptide added to both sides (123 mV).

For asymmetric membranes, the voltage threshold for insertion of alamethicin is dependent on the lipid composition of the leaflet side to which the peptide is introduced (i.e. the *cis* leaflet). For instance, when alamethicin is added to the DPhPC (*cis*) side, which creates a positive intramembrane potential with respect to the *trans* side, insertion and channel formation occurs at a lower voltage than when the *cis* leaflet is comprised of DOPhPC lipids, which creates a negative intramembrane potential with respect to the *trans* DPhPC side. This result is consistent with the notion that DPhPC (*cis*) :DOPhPC (*trans*) presents a lower energy barrier for insertion into the *cis* side due to the net positive intramembrane potential caused by a difference in leaflet dipole potentials (Figure 27) [80, 81, 143]. Likewise, reversing the side of peptide incorporation presents a higher energy barrier to alamethicin insertion due to the negative electric field acting from *cis* to *trans*. Nonetheless, the values of voltage threshold for alamethicin insertion in asymmetric bilayers are not significantly different from those measured for symmetric membranes comprised of either lipid. This implies that the total voltage difference felt by peptides at an asymmetric membrane is not simply the sum of applied, surface and dipole potentials.

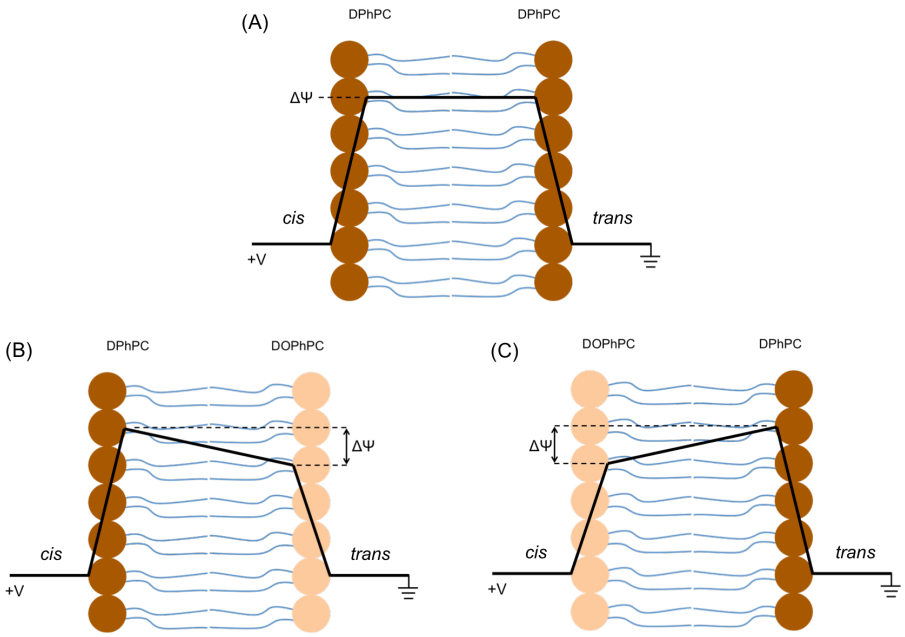

Figure 27. Schematics of membrane profiles. (A) Symmetric bilayer showing a zero intramembrane potential (ΔΨ). (B) Asymmetric membrane with DOPhPC on the ground side with the intramembrane potential being the difference in height between the dipole potential from DPhPC and DOPhPC. (C) Asymmetric membrane reversed with DPhPC on the ground side.

In addition, the data suggest that the changes in intramembrane potential over time are due to changes in dipole potential of the leaflets rather than surface potential. This conclusion is in part inferred by the fact that the accumulation of surface-bound alamethicin, which is negatively charged, would act to continue to lower the potential of the *cis* leaflet, thereby increasing the barrier to alamethicin insertion in either leaflet composition. In contrast, our measurements of asymmetric membranes exposed to alamethicin show opposite trends over a 5-hour period of study: alamethicin added to a DPhPC leaflet increases the voltage threshold (i.e. the energy barrier to insertion has been raised), while alamethicin added to a DOPhPC leaflet decreases the voltage threshold (i.e. the energy barrier has been lowered) (Figure 28).

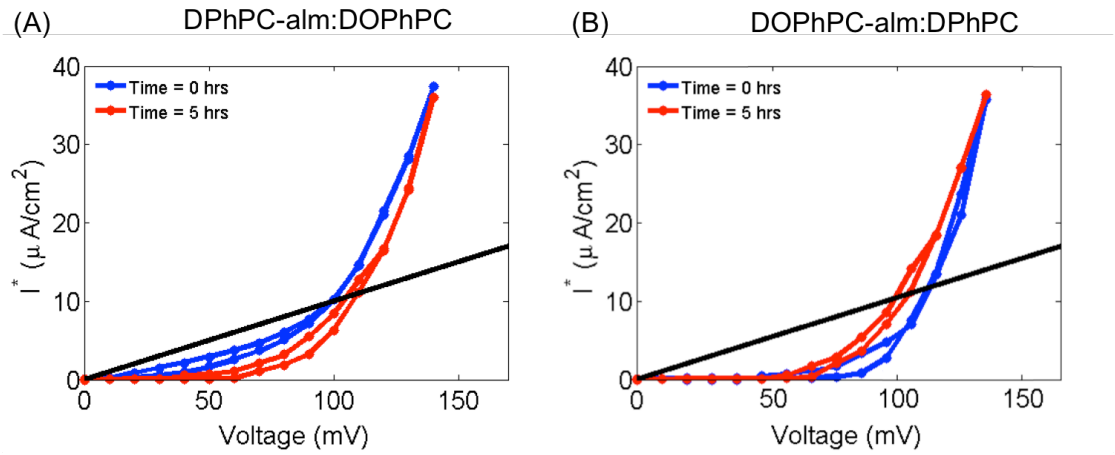

Figure 28. Cyclic voltammetry curves at different times. The current response is normalized by membrane area for each scan and plotted versus voltage (mV). Normalized current for asymmetric DIB of (A) DPhPC-alm:DOPhPC and (B) DOPhPC-alm:DPhPC. The black line is the selected specific conductance of 100 μS/cm^2.

Changes in the dipole potentials of the leaflets are either caused by lipid flip-flop or peptide rearrangement/translocation. We consider the placement of alamethicin because this molecule is known to have a dipole moment of 65 mD [81, 144] and our measurements are conducted at relatively high molar peptide/lipid ratios of 1/1.2-1/2.4. In Figure 29, we do not observe an increase in the magnitude of negative current at negative applied potentials even after 5 hours from formation. This indicates that complete translocation of peptides through the bilayer, which would enable voltage-dependent channel formation in the membrane at negative applied potentials, is not occurring. Hall observed peptide translocation, but only in conditions where an applied voltage above the insertion threshold is maintained for many minutes [81]. In contrast, our measurements are conducted intermittently, between periods of zero applied potential. Therefore, we interpret the measured decreases in intramembrane potential versus time for asymmetric membranes due to lipid translocation or peptide rearrangement within the same leaflet. Also since the magnitude of

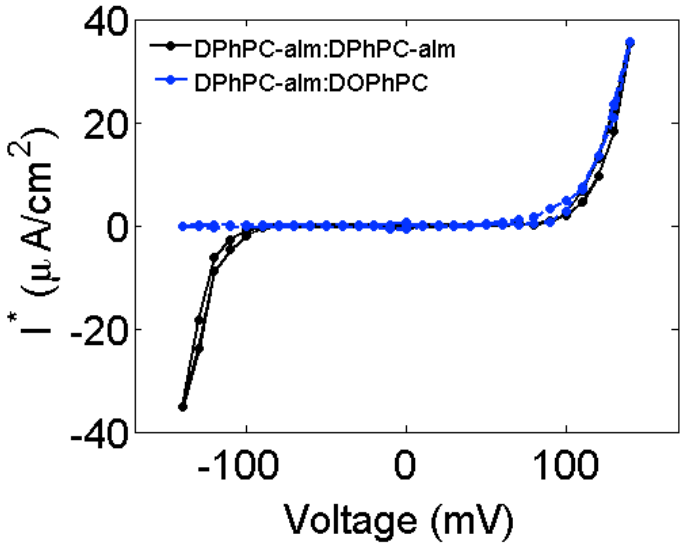

Figure 29. Current versus voltage curve for symmetric DIB with alamethicin on both sides (black line) compared to asymmetric DIB with alamethicin on the applied voltage side (blue line). Measurements were taken after 5 hours.

change in intramembrane potential is affected by peptide concentration further identifies alamethicin as the cause for the change in dipole potential.

Not only does the intramembrane potential change over time (Figure 25), voltage thresholds for asymmetric membranes also shift in time. The I-V curve shows that voltage threshold increases for DPhPC-alm:DOPhPC (Figure 28A). This shift to the right suggests that the energy barrier for peptide insertion has increased over time. Lipid flip-flop in either direction could cause the dipole potential difference to decrease, thereby increasing the voltage needed for alamethicin insertion. This is also consistent with the opposite result found for DOPhPC-alm:DPhPC, where the voltage threshold decreases over time indicating a lower insertion energy barrier (Figure 28B).

While our results provide strong evidence that alamethicin induces a change in the intramembrane potential in asymmetric membranes, there are remaining gaps and questions that need to be addressed. For instance, does the dipole

potential of alamethicin-doped leaflet in a symmetric membrane change over time? We observed a nonzero and time dependent intramembrane potential in a symmetric, suggesting that alamethicin affects dipole and/or surface potential and changes with time. However, this magnitude is only 8-10 mV whereas in asymmetric membranes, the change in total intramembrane potential is ~40 mV. While this larger magnitude difference suggests lipid flip-flop is the major role in the change to intramembrane potential, we have not yet measured changes in voltage threshold for symmetric membranes exposed on one leaflet to alamethicin. This experiment would determine if the effective concentration of alamethicin in the membrane changes with time, as well as if and how the dipole and/or surface potential changes with time. Another remaining question is why the voltage threshold for DOPhPC-alm:DPhPC is similar to that for DOPhPC-alm:DOPhPC, for which we would expect a lower energy barrier for insertion due to less negative difference in dipole potential. Further cv experiments with symmetric alamethicin with asymmetric leaflets can help determine the magnitude of influence of surface and/or dipole potential of the lipids by creating a baseline measurements when exposed to peptides on both sides.

4.6 Summary and future work

This work examined a method to create streams of alternating droplet compositions, i.e. A-B-A-B, via two opposing T-junctions within a microfluidic device. In the same device, the droplets were sequentially captured in predetermined locations to enable the spontaneous formation of synthetic lipid bilayers between droplets of different compositions. Contrasting our prior work demonstrating microfluidic DIB formation, this revised system maintains a key component of the DIB technique by allowing bilayer formation to occur between droplets of differing compositions, which allow asymmetric conditions within and across the membrane to be prescribed.

Using this system, we then demonstrated the assembly and interrogation of asymmetric DIBs consisting of different lipid compositions in each leaflet of the bilayer. The asymmetric DPhPC-DOPhPC bilayers formed resulted in a dc, non-zero membrane potential of |137mV| across each membrane due to the difference in dipole potentials of the two lipid types. Furthermore based on the measured polarity of this potential, we were able to determine which droplet contains DPhPC and DOPhPC. The observed alternating polarity of membrane potentials within the 8 DIB array illustrates that the arrangements of sequential DIBs formed between alternating droplets reverse with respect to the sensing and ground electrodes.

In the second study, alamethicin peptides were included in only one of two droplets in each DIB pair, which enabled voltage-dependent insertion to occur only at one polarity. Cyclic voltammetry measurements confirmed the direction of insertion of alamethicin channels in bilayers. Because peptide insertion and gating occurred at a single polarity in each membrane, the sign of the voltage again determined the position with respect to the electrodes of the droplet containing the peptides. Also, these results showcase the ability to simultaneously perform electrical measurements on multiple DIBs, which motivates the use of a microfluidic approach to increase the efficiency of membrane studies.

In the third study, intramembrane potential was monitored over a period of hours. For asymmetric DPhPC-DOPhPC bilayers, the intramembrane potential remained steady over the course of 15 hours. However when alamethicin is added to asymmetric DIBs, the membrane potential begins to decrease after the first hour. This decrease suggests that the difference in dipole potential for the two leaflets is reduced possibly by lipid translocation. In addition, a series of CV measurements were performed to determine the difference in threshold voltage needed to drive alamethicin insertion between symmetric and asymmetric DIBs.

Overall, symmetric DPhPC DIBs with alamethicin on both sides of the bilayer exhibits the highest voltage threshold. While asymmetric DPhPC-DOPhPC DIBs with alamethicin on the DPhPC side have the lowest voltage threshold. The low voltage threshold indicates that the membrane potential of asymmetric DIBs participates in peptide insertion. Additional experiments are still needed to fully understand the dynamics of alamethicin in asymmetric membranes. Single channel recording of alamethicin activity at a set dc voltage needs to be performed to compare conductance states between symmetric and asymmetric bilayers. This will help understand if the difference in membrane potential increases the conductance values.

CHAPTER 5
MICROFLUIDIC DEVICE FOR SINGLE CELL CAPTURE

While there are microfluidic devices capable of single cell capture and analysis such as drug screening and cell division, there is currently no efficient approaches to perform and study gene transformation on individual plant protoplast cells. The work described herein aims to address Objective 4. Here we designed and fabricated a microfluidic system for systematic single cell capture of plant protoplast cells for the purpose of DNA transformation. Specifically, a similar resistive modeling approach used in Chapter 3 is applied to design traps and array layout, and provide guidelines for device operation conditions such as flow rates to maintain appropriate pressure throughout the system to minimize cell squeeze through. The results in this chapter is a step towards improving the ability to study gene transformation on an individual cell basis, with greater spatial and temporal resolution of each cell's response, and enable post-collection of successfully transformed cells to grow whole plants containing specific genes.

5.1 Introduction

Transformation of plant cells allows for the altering of DNA with the purpose of giving the plant a new and useful trait. There are many methods for introducing the new segment of DNA to be inserted in the plant chromosome, all of which start with transfecting a single cell which are then regenerated into full plants. Some of the methods for plant cell transformation, Methods for plant transformation such as PEG-mediated and electroporation involve creating pores in the cell membrane so that DNA can enter the cell, and can only be done with protoplasts (plant cells where the cell wall has been digested) [89-93]. While transformation of protoplasts has a higher efficiency due to the lack of the thick cell wall barrier, the efficiency of *in vitro* transformation is still very low in many

plant species [89-91]. Traditional methods of protoplast transformation are limited by a difficulty in obtaining high concentrations of viable protoplasts, low transformation efficiency, the necessity for a large quantity of DNA, and inconsistent results across species.

Microfluidics can help overcome these disadvantages by system miniaturization, enhanced efficiency, and the ability to study single cell transformation. The use of a microfluidic device allows for fewer protoplasts, (one cell per trap instead of 1×10^6 protoplasts/mL) and amount of DNA. Captured individual protoplasts allow studies at the single cell level of transformation. The advantage of being able to study single cell transformation is a closer examination of protein expression and the collection of proteins secreted from the plant protoplasts, enabling a bio-production system for medically relevant compounds as well as identifying stressors in plants (i.e. drought).

We seek to fabricate a device that utilizes steady fluid flow to place a stream of protoplasts into sequential hydrodynamic traps. The device needs to enable the collection of cells at every trap in the array, and minimize the hydrodynamic pressure developed across trapped cells to prevent unwanted release from traps, and be scalable in an array layout. A circuit-based modeling approach is employed to design and arrange arrays of hydrodynamic traps.

5.2 Resistive flow modeling for single cell trapping

Similar to the device used to capture DIBs in the Chapter 3, a series of hydrodynamic traps branching from the main channel are designed such that each trap captures a single protoplast in a serially manner. We utilized the same electrical circuit analogy, to developed a resistive flow model to determine appropriate dimensions for the fluid channels used for cell trapping as well as for designing the layout of a multi-trap array within the encapsulating substrate.

Recall, in a single-phase laminar flow, the pressure difference along a section of a microchannel is equal to the product of the applied volumetric flow rate, *Q*, and the hydrodynamic resistance of the channel, *R*. The hydrodynamic resistance for Poiseulle flow in a rectangular channel [101] is given by

$$R = \frac{12\mu L}{h^3 w}\left[1 - \frac{192}{\pi^5} \times \frac{h}{w} \times \tanh\left(\frac{\pi w}{2h}\right)\right]^{-1} \quad (11)$$

where *L*, *w*, and *h* are the length, width, and height, respectively, of a particular segment of the channel, and μ is the viscosity of the carrier fluid (i.e. oil for a DIB system). Equation 11 can be used to design channels of specific dimensions to dictate the flow resistance in regions of a device and thereby affect the course of droplet travel.

A single hydrodynamic trap is designed to accommodate a single cell. In our device, a trap will consist of a square compartment that resides adjacent to the main flow channel. Opposite entry from the main channel, each trap also features a narrow exit channel, which we refer to as bleed valves. The trap design and its ability to collect cells carried in the main stream are thus based on the hydrodynamic resistance of the trap relative to that of the bypassing main channel. For instance, a cell will prefer to enter an empty trap that has a hydrodynamic resistance, R_T, less than that of the resistance offered by bypassing the trap and flowing through the main channel, R_M. The flow resistance of each lane in a trap is calculated by

$$R_T = R_a + R_b \,, \quad (12)$$

where R_a is the resistance due to the square portion of the trap and R_b represents the contribution to the resistance from the bleed value (Figure 30A).

When R_T is less than R_M, the first protoplast cell in the stream will divert from the main channel and come to rest in the hydrodynamic trap near the bleed valves (Figure 30B). The bleed valve halts the protoplasts within the trap as long as the

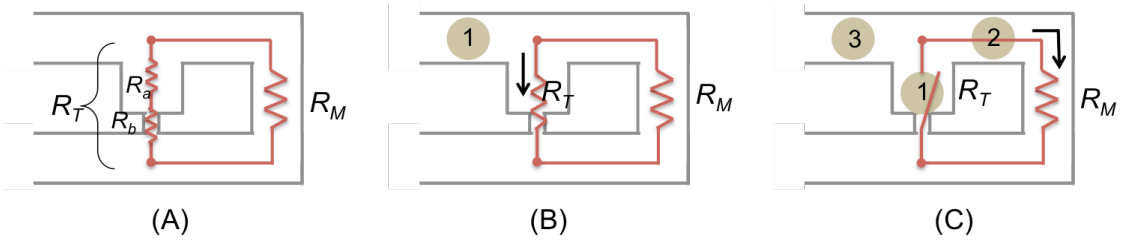

Figure 30. Schematic of flow resistances, *R*, in a single trap. (A) Diagram of a trap where the trap resistance R_T equals R_a +R_b such that total trap resistance R_T is the sum of the parallel resistors. (B) A protoplast will enter the trap when trap resistance, R_T, is less than resistance of the main channel, R_M. (C) Once a cell is trapped, R_T becomes greater than R_M, guiding following protoplasts to bypass filled trap.

resulting pressure drop that develops across a cell blocking the bleed valve does not cause the cell to squeeze-through and escape. Specifically, the pressure drop across a filled trap must remain less than the Laplace pressure, ΔP_L, across the protoplast residing at the entrance of a bleed valve, which can be calculated via

$$\Delta P_L = 2\gamma\left(\frac{1}{w_b} - \frac{1}{w_t}\right), \tag{3}$$

where, γ is the resting tension of a protoplast cell and w_b and w_t are widths of the bleed valve and trap, respectively.[101] Once a trap fills, the presence of a cell at the entry to the bleed valve causes the flow resistance to increase significantly. As a result, the second cell in the stream bypasses the filled trap, preferring to remain in the main channel, which now offers a relatively lower resistance to flow (Figure 30C). Thus, an open trap behaves like a closed switch in an electrical circuit (with low resistance and high flow rate), while a filled trap acts like an open switch (with high resistance and low flow rate).

Because the hydrodynamic resistance offered by both the main channel and a trap depends on the connection of these sections to additional traps or channels located downstream, one must consider the entire fluidic resistance of the

device. This information is especially necessary for understanding how to configure arrays of traps such that large networks of cells can be efficiently and quickly captured in a microfluidic device. Thus, we used a similar resistive circuit model from Chapter 3 to enable calculation of fluid flow rates and pressure drops between channel intersections for characterizing the trapping performance of a multiple-trap device.

For this analysis, the values of channel resistance used are based on a square traps dimensions of 55 μm x 55 μm and using a bleed valve that is 15 μm wide and 10 μm long. These dimensions reflect the sizes to capture 50 μm diameter protoplast cell. The main channel sections are 60 μm wide and all channels have a depth of 60 μm. These dimensions correspond to equivalent resistances of 739 Pa-s/μL and 1.2×10^3 Pa-s/μL for R_T and R_M, respectively.

To evaluate the serial layout for single cell isolation, we use Kirchoff's Current Law (KCL) for fluid flow at each channel intersection as in Chapter 3. Using the same matrixes for serial trapping mode, we are able to compute the pressure distribution in the array and calculate for each trap in an array the ratio of fluid flow entering the trap to that which bypasses the trap, which enables us to determine if direct trapping occurs. The flow rate within each section of a multi-trap model is computed by dividing the difference in absolute pressure between nodes by the hydrodynamic resistance of that section. Figure 31A shows the ratio of flow rate entering the first trap of successive unfilled traps to the flow rate bypassing that first trap. This calculation is performed sequentially by varying the number of filled traps in a 60-trap model. Therefore, the flow rate ratio reflects the preference of a droplet approaching the first unfilled trap to either enter the trap or bypass it. A ratio greater than one indicates direct trapping as marked by the unshaded region in Figure 31A. The results confirm constant direct trapping during complete filling of the array.

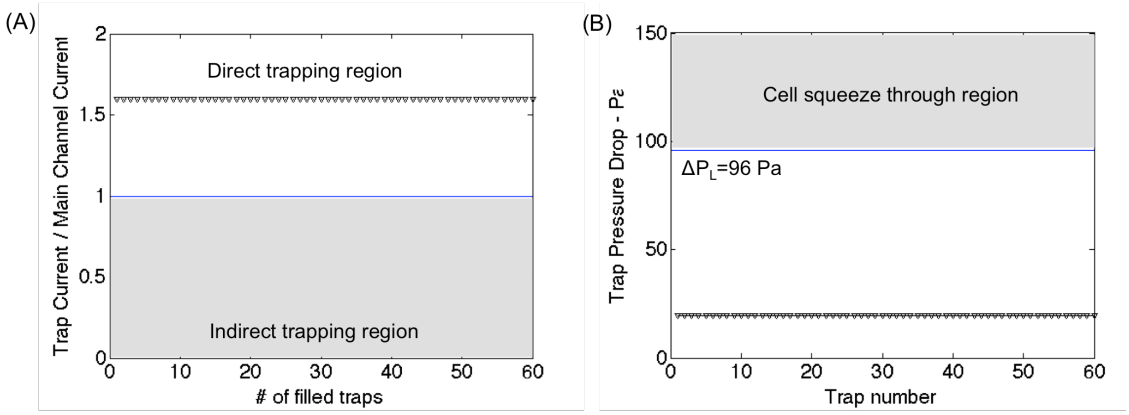

Figure 31. (A) Calculated flow rate ratio through an empty trap versus the main channel as a 60-trap system is being filled. Because all traps are in the unshaded region means the entire array fills via direct trapping. (B) Estimated pressure drop within a filled trap versus location in the array. The pressure drop is constant and does not exceed the Laplace pressure (ΔP_L) to cause squeeze through.

The expected pressure drop across each trap is computed by determining the difference in absolute pressure between the entrance and exit nodes of the trap. This calculation is performed for a filled array to determine if cells will squeeze-through the bleed valve. An array of filled traps is considered specifically since this condition represents the highest absolute pressure a system can experience and corresponds to when cells could be squeezed through the bleed valves. The occurrence of squeeze-through is assessed when the pressure drop across a trap is higher than a Laplace pressure of 96 Pa (shown as the shaded region in Figure 28B) determined using a membrane tension of 1 mN/m [145] and trap and bleed valve widths of 55 μm and 15 μm, respectively. The analysis shows the trap pressure drop (~20 Pa) is much lower than the Laplace pressure (Figure 31B).

5.3 Device operation

The experimental realization of protoplast capture and on-chip transformation, requires the subsequent injection of three different aqueous solutions. Therefore,

a 5-way manual valve with four distinct inlets and one common outlet is used to accommodate switching between solutions for the injection protocol.

First, all PTFE tubing lines from the syringe to the valve and from the valve to the microfluidic device are primed before the process begins to avoid air bubbles entering the chip. Protoplasts suspended in MMg solution (0.4 M mannitol, 15 mM $MgCl_2$, 4 mM MES), are injected into the device at a flow rate of 0.5 µL/min. Once the protoplasts are captured in the traps as seen in Figure 32, a 20% PEG solution is introduced also at a flow rate of 0.5 µL/min. After 30 minutes, the injected solution is switched to a wash buffer (0.8 M mannitol, 4 mM MES, 4 mM KCl) at a flow rate of 0.5 µL/min to remove any remaining PEG solution. After an additional 30 minutes, the flow rate of the wash buffer is reduced to 0.05 µL/min for overnight to monitor protoplast viability. In the near future the wash buffer will contain DNA for transformation.

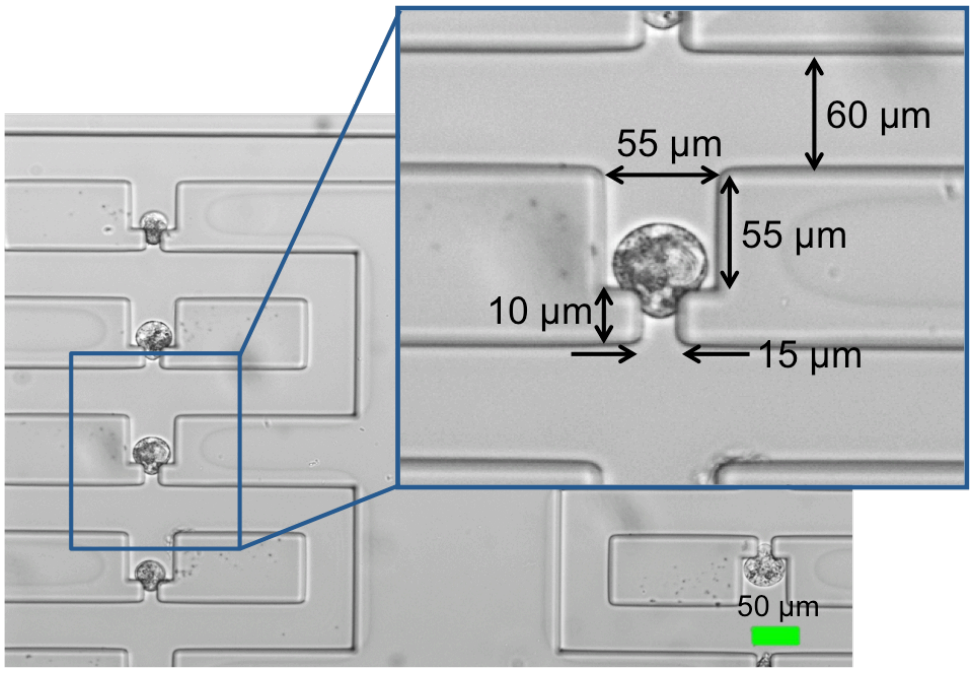

Figure 32. Captured soybean protoplast cells in hydrodynamic traps. Inset shows channel dimensions. Depth is 60 µm.

5.4 Hydrodynamic traps for single cell capture

Based on the analysis a microfluidic device is fabricated with 60 traps for capturing 50 μm diameter protoplast cells. The dimension for the main channel is 60 μm wide. For each trap, the width is 55 μm and length is also 55 μm. A bleed valve is placed in the center of each trap and has a length of 10 μm and width of 15 μm. All channels in the fabricated device have a depth of 60 μm. Based on these trap dimensions, the computed fluidic resistance of an open trap, R_T, is computed to be 739 Pa-s/μL, versus a main channel resistance, R_M, of 1.2×10^3 Pa-s/μL. The resistances are based on a viscosity of 1×10^{-3} Pa.s for the MMg solution, where the protoplasts are suspended. Since $R_T < R_M$, the fabricated devices is expected to exhibit direct trapping.

In our experiments we observed the cells did not bypass open traps, confirming the array maintain direct trapping. The trapping efficiency is 100% as long as there is no debris blocking the traps. Debris from the solution can enter empty traps and block the bleed valve causing the trap resistance to increase and directing subsequent protoplasts to bypass the trap. Debris can be reduced through filtration of the protoplast solutions. In addition, we did notice that the protoplasts are smaller than predicted, with diameters closer to 30-40 μm. Therefore, there are instances when multiple cells can occupy a single trap. A revised device with smaller trap dimensions will be needed to address this issue. Nonetheless, we observe no cell squeeze-through in the devices during all solutions, which confirms that the pressure drop across the traps remain less than the critical Laplace pressure of 96 Pa. Table 5 summaries the flow rates, viscosities, and corresponding trap pressure of the solutions used.

5.5 Protoplast viability within a microfluidic device

Once protoplasts are trapped in the microfluidic, the cells are monitored for 24 hours to confirm cell viability at the timescale necessary for transformation. Cell viability staining was conducted with fluorescein diacetate (FDA) and propidium

Table 5. Viscosity, flow rate, and trap pressure for solutions used for transformation.

Solution	Viscosity (Pa.s)	Flow rate (μL/min)	ΔP (Pa)
MMg	$1x10^{-3}$	0.5	9.8
20% PEG	0.0073	0.5	71.6
Wash buffer	$1x10^{-3}$	0.5	9.8

iodide (PI). FDA is taken up by cells, which convert the non-fluorescent FDA into the green fluorescent metabolite fluorescein [146]. The measured signal serves as indicator for viable cells. In contrast, the nuclei staining dye PI cannot pass through a viable cell membrane. It reaches the nucleus by passing through disordered areas of dead cell membranes therefore only staining dead cells or broken parts of cells [146].

Once protoplasts are trapped, which takes less than a minute, a wash buffer solution containing FDA and PI is injected into the microchip at a rate of 0.05μL/min for 24 hours. Figure 33A shows green fluorescent protoplasts indicating these cells remained alive after 24 hours. In this set of protoplasts there is one dead (cell in upper most trap) as shown in Figure 33B since it is the only cell that has a fluorescent red color while the remaining cells are non fluorescent, signifying the PI could not penetrate the membrane. Over the course of 5 trials with 60 captured protoplasts in each trial, there is a 90% viability rate for 24 hours. A cause for cell death can be due to prolonged exposure to the PEG solution. Some protoplasts are less resilient than others and cannot recover from pores created by PEG in the cell membrane.

5.6 Nucleus staining for proof of concept of DNA transformation

In this study, captured protoplasts are successively exposed to: 1) FDA to confirm viability; 2) PI to confirm PEG has permeated the membrane; and 3)

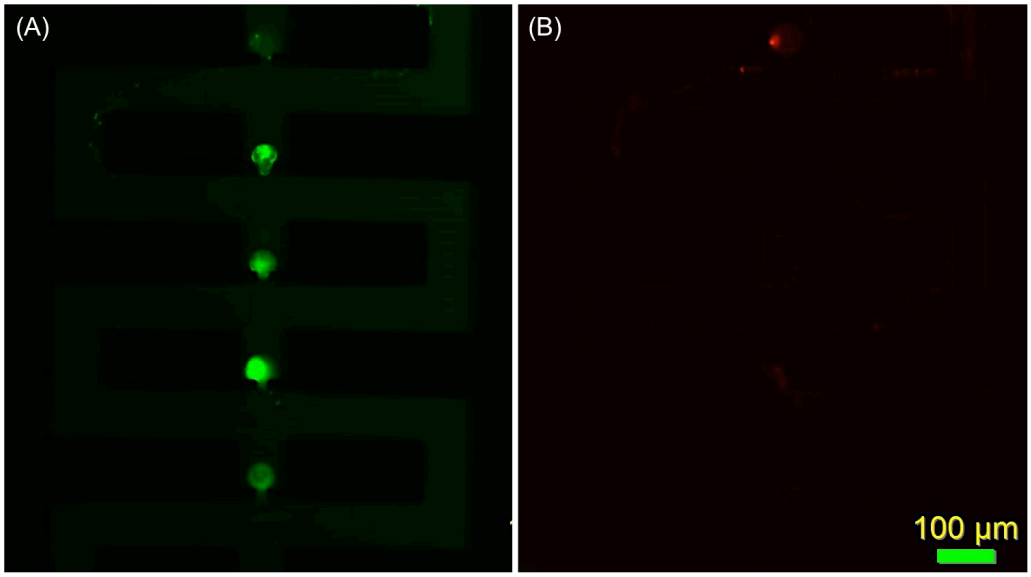

Figure 33. (A) Image of FDA stained protoplasts verifying that 4 of the 5 trapped protoplasts within view are alive. (B) PI's red fluorescence indicates cell death in 1 of 5 trapped protoplasts; seen in top trap.

DAPI (4′,6-diamidino-2-phenylindole) which is a blue-fluorescent DNA stain to show proof of concept for transformation and specifically location of DNA. First the solution with protoplasts and FDA are loaded into the chip (Figure 34A). Figure 34B confirms the capture protoplast is alive, since FDA only fluoresces when metabolized by the cell. Next, the solution containing 20% PEG and PI is injected. Even though PI is typically used to indicate dead cells, the stain is injected here to determine if PEG has permeated the membrane. Figure 34C shows a red stained nucleus suggesting PEG has caused defeats in the membrane for the PI to enter the cell. The final solution contains a wash buffer with DAPI. The blue stained nucleus in Figure 34D indicates DAPI was able to enter through the cell illustrating that when DNA is placed in the solution, transformation should occur on all live cells.

5.7 Summary and future direction

In summary, we used a resistive modeling approach to develop and fabricate a microfluidic device capable of direct trapping of plant protoplast cells while

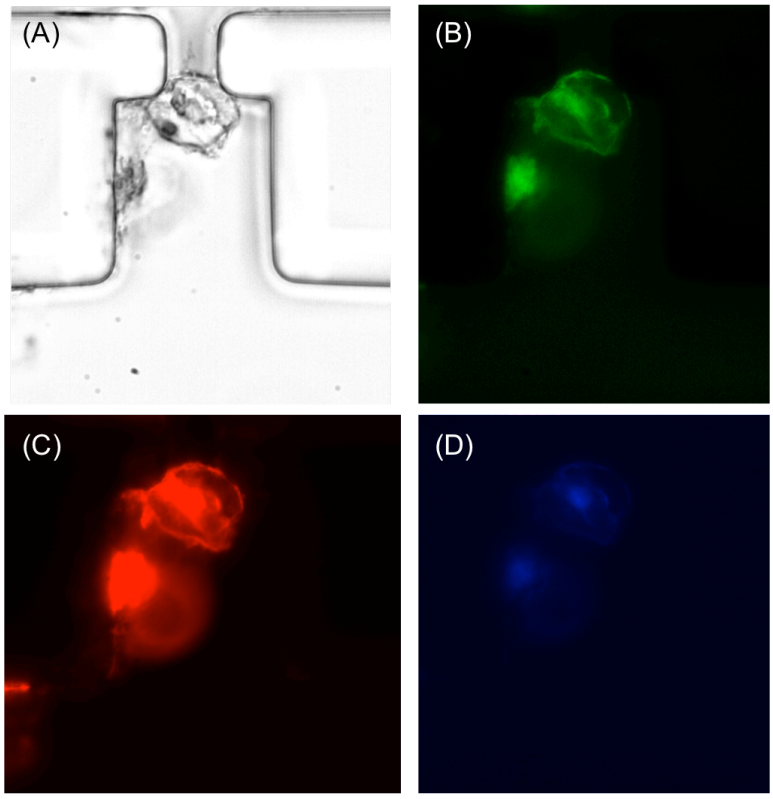

Figure 34. Images of two captured protoplast in (A) brightfield, (B) FDA stain, (C) PI stain, and (D) DAPI stain.

restricting the pressure across each to be less than the Laplace pressure to ensure the captured protoplasts remain in the traps. Also we showed proof of concept for DNA transformation by using fluorescent dyes to qualitatively analyze each step of the process.

There are changes that need to be made to the current microfluidic design. A sorting shunt will be implemented to discard debris and small, unwanted protoplasts. Also to reduce the likelihood of capturing multiple protoplasts in one trap, the depth, trap and main channel dimensions will be reduced. In addition, we want to lower the overall resistance to reduce the pressure in the system. In order to do so, the bleed valve and bypass channel can be shorten and the trap length can be shorter.

In addition we need to consider how to eventually harvest the captured transfected protoplast cells. For instance the resistances of the channels will need to be evaluated when the fluid flow is reversed. Also, concerns of protoplasts being trapped or stuck at the bleed valves exists during black flow needs to be addressed. The necessary flow rates for successful black flow will need to be determined to redirect the captured protoplasts into the main channel with minimal disruption to the cells' viability.

CHAPTER 6
SUMMARY AND CONCLUSION

6.1 Research overview

The overarching goal of this work is to develop a high throughput microfluidic system in order to investigate numerous basic lipid bilayer studies and membrane-mediated processes with greater efficiency and statistical significance. Specifically, develop an automated high-throughput droplet generation and arrangement system to create an array of DIBs, which can be electrically interrogated, in an enclosed substrate. Chapter 3 presents an equivalent electrical circuit modeling approach to design a self-contained microfluidic device capable of generating monodisperse lipid-encased droplets and routing the droplets to predetermined locations to form an array of DIBs. The microfluidic device is able to collect of droplets at every trap in the array, and minimize the hydrodynamic pressure developed across trapped droplets to prevent unwanted squeeze-through. Also, integrated thin-film electrodes allow simultaneous electrical characterization of multiple droplet interface bilayers to improve the efficiency of studying membrane properties and peptide insertion. Chapter 4 builds on the development of Chapter 3, by incorporating a method to generate alternating droplets to form asymmetric DIBS in the microfluidic device. Chapter continues with investigating intramembrane potential between bilayers containing asymmetric zwitterionic phospholipid leaflets (i.e. DPhPC and DOPhPC). *In situ* measurement technique is applied on an array of asymmetric DIBs to study lipid asymmetry versus time and in the presence of peptides. This is a step towards understanding the effects of peptides on the disruption of asymmetric lipid membranes and intramembrane potential, which are not well known. In Chapter 5, goal of developing an automated microfluidic array is applied to isolate and transform single cells. This would greatly improve the ability to study gene transformation on an individual cell basis, with greater

spatial and temporal resolution of each cell's response, and enable post-collection of successfully transformed cells to grow whole plants containing specific genes.

6.2 Contributions and conclusions

This section presents contributions from each research objective, which aimed to address the scientific gaps identified in Chapter 1 (objectives are restated here again for reference).

6.2.1 Objective 1 (addressing Gap 1)

Use an equivalent electrical circuit modeling approach to design a self-contained microfluidic device capable of generating monodisperse lipid-encased droplets and routing the droplets to predetermined locations to form an array of DIBs. The device needs to enable the collection of droplets at every trap in the array, and minimize the hydrodynamic pressure developed across trapped droplets to prevent unwanted droplet release from traps or disrupt the resulting DIB, and be scalable in an array layout.

The key contributions of this research include:

- Development and analysis of resistance-based model for designing scalable microfluidic devices that produce, route, and capture for DIB formation monodisperse aqueous droplets in oil.
- Experimental validation that a serial arrangement (Model C in Figure 14) of droplet traps operates in direct trapping upon filling of all traps and maintains a low-pressure drop across each filled trap, so that captured droplets are retained and do not experience droplet squeeze-through the bleed valves. We demonstrated that these conditions enable large arrays of two-, three-, and four-droplet DIBs to be rapidly assembled at separate locations within a single device.

6.2.2 Objective 2 (addressing Gap 1)

Design and fabricate integrated thin-film electrodes within the same droplet generation and trapping microfluidic device fabricated in Objective 1 to permit simultaneous electrical characterization of multiple droplet interface bilayers to improve the efficiency of studying membrane properties and peptide insertion.

The primary contribution of this effort includes:

- Implementation of thin film electrodes for *in situ* electrical characterization of multi-DIB arrays, which enables simultaneous single channel measurements of ion channels and measurements of bilayer conductance and capacitance over time for multiple DIBs. For the first time, this capability enables efficient characterization of many DIBs at once, which has immediate applications in creating functional material systems for energy conversion or sensing as well as understanding how chemical species and nanomaterials interact with models of biological membranes.

6.2.3 Objective 3 (addressing Gap 2)

Incorporate a method to generate alternating droplets to form asymmetric DIBS in the microfluidic device from Objective 1&2. Then, electrically characterize the intramembrane potential between bilayers containing asymmetric zwitterionic phospholipid leaflets (i.e. DPhPC and DOPhPC). This *in situ* measurement technique will be applied for the first time on an array of asymmetric DIBs to study lipid asymmetry versus time and in the presence of peptides.

Technical and scientific contributions of this research include:

- Demonstration that the use two, opposing T-junctions for droplet dispensing can be integrated into the microfluidic device to enable assembly of asymmetric DIBs.
- Measurements via thin-film electrodes are able to record changes in intramembrane potential in asymmetric membranes are due to lipid flip-flop because the shifts in voltage threshold indicate a dipole change not a surface potential change. Also because we do not see the peptide

translocating in the cv scan also supports the notion that lipids are moving from one side to the other.

6.2.4 Objective 4 (addressing Gap 3)

Design and fabricate a microfluidic system for systematic single cell capture of plant protoplast cells for the purpose of DNA transformation. A similar resistive modeling approach used in Objective 1 will be applied to design traps and array layout, and provide guidelines for device operation conditions such as flow rates to maintain appropriate pressure throughout the system to minimize cell squeeze through.

Contribution to the field includes:

- Model-based design and successful demonstration of a scalable cell capturing microfluidic device for enabling single cell analyses of plant protoplasts, such as gene transformation.

Together this research contributes to a high-throughput microfluidic system for synthetic membranes and live-cell studies. An encapsulated device with embedded functionality can be a platform for numerous membrane bases applications.

REFERENCES

1. Alberts, B., et al., *Molecular Biology of the Cell, 4th edition*. 2002, New York: Garland Science.
2. Son, A. *Animal Cell Structure*. Available from: http://apbiology-cells.weebly.com/animal-cells.html.
3. BS, D., et al., *Glomerular basement membrane: in vitro studies of water and protein permeability.* Am J Physiol. , 1992 **262**(6): p. F919-F926.
4. Sato, K. and R.L. Dobson, *Enzymatic Basis For The Active Transport Of Sodium In The Duct And Secretory Portion Of The Eccrine Sweat Gland.* Journal of Investigative Dermatology, 1970. **55**(1): p. 53-56.
5. Yeagle, P.L., *Cholesterol and the cell membrane.* Biochimica et Biophysica Acta (BBA) - Reviews on Biomembranes, 1985. **822**(3): p. 267-287.
6. Hille, B., *Ionic channels in excitable membranes. Current problems and biophysical approaches.* Biophysical Journal, 1978. **22**(2): p. 283-294.
7. WR., L., *Junctional intercellular communication: the cell-to-cell membrane channel.* Physiol Rev., 1981. **61**(4): p. 829-913.
8. Simons, K. and W.L. Vaz, *Model systems, lipid rafts, and cell membranes.* Annu Rev Biophys Biomol Struct, 2004. **33**: p. 269-95.
9. Lodish, H., et al., *Molecular Cell Biology, 4th edition*. 2000, New York: W. H. Freeman.
10. Almén, M.S., et al., *Mapping the human membrane proteome: a majority of the human membrane proteins can be classified according to function and evolutionary origin.* BMC Biology, 2009. **7**(1): p. 50.
11. R, L. and A. O, *Voltage-dependent channels in planar lipid bilayer membranes.* Physiol Rev., 1981. **61**(1): p. 77-150.
12. Tien, H.T. and A. Ottova, *The bilayer lipid membrane (BLM) under electrical fields.* IEEE Transactions, 2003. **10**(5): p. 717-727.
13. Needham, D. and R.S. Nunn, *Elastic deformation and failure of lipid bilayer membranes containing cholesterol.* Biophysical Journal, 1990. **58**(4): p. 997-1009.
14. Lindahl, E. and M.S.P. Sansom, *Membrane proteins: molecular dynamics simulations.* Current Opinion in Structural Biology, 2008. **18**(4): p. 425-431.
15. Baumann, G. and P. Mueller, *A molecular model of membrane excitability.* Journal of Supramolecular Structure, 1974. **2**(5-6): p. 538-557.
16. Kagan, B.L., et al., *Antimicrobial defensin peptides form voltage-dependent ion-permeable channels in planar lipid bilayer membranes.* Proceedings of the National Academy of Sciences, 1990. **87**(1): p. 210-214.
17. DW., D. and B. J., *Permeability of lipid bilayers to water and ionic solutes.* Chem Phys Lipids, 1986. **40**(2): p. 167-188.

18. Walter, A. and J. Gutknecht, *Permeability of small nonelectrolytes through lipid bilayer membranes.* The Journal of Membrane Biology, 1986. **90**(3): p. 207-217.
19. Abiror, I.G., et al., *246 - Electric breakdown of bilayer lipid membranes I. The main experimental facts and their qualitative discussion.* Bioelectrochemistry and Bioenergetics, 1979. **6**(1): p. 37-52.
20. Bayley, H., et al., *Droplet interface bilayers.* Mol Biosyst, 2008. **4**(12): p. 1191-208.
21. Henn, F.A. and T.E. Thompson, *Synthetic Lipid Bilayer Membranes.* Annual Review of Biochemistry, 1969. **38**(1): p. 241-262.
22. Szoka, F. and D. Papahadjopoulos, *Comparative Properties and Methods of Preparation of Lipid Vesicles (Liposomes).* Annual Review of Biophysics and Bioengineering, 1980. **9**(1): p. 467-508.
23. Kornberg, R.D. and H.M. McConnell, *Lateral Diffusion of Phospholipids in a Vesicle Membrane.* Proceedings of the National Academy of Sciences of the United States of America, 1971. **68**(10): p. 2564-2568.
24. Eisenberg, M., J.E. Hall, and C.A. Mead, *The nature of the voltage-dependent conductance induced by alamethicin in black lipid membranes.* The Journal of Membrane Biology, 1973. **14**(1): p. 143-176.
25. Wiegand, G., et al., *Electrical Properties of Supported Lipid Bilayer Membranes.* The Journal of Physical Chemistry B, 2002. **106**(16): p. 4245-4254.
26. Naumann, R., et al., *Incorporation of Membrane Proteins in Solid-Supported Lipid Layers.* Angewandte Chemie International Edition in English, 1995. **34**(18): p. 2056-2058.
27. Cornell, B.A., et al., *Tethered-bilayer lipid membranes as a support for membrane-active peptides.* Biochemical Society Transactions, 2001. **29**(4): p. 613.
28. Holden, M.A., D. Needham, and H. Bayley, *Functional Bionetworks from Nanoliter Water Droplets.* J. Am. Chem. Soc., 2007. **129**(27): p. 8650-8655.
29. Funakoshi, K., H. Suzuki, and S. Takeuchi, *Lipid Bilayer Formation by Contacting Monolayers in a Microfluidic Device for Membrane Protein Analysis.* Anal. Chem., 2006. **78**(24): p. 8169-8174.
30. Poulin, P. and J. Bibette, *Adhesion of Water Droplets in Organic Solvent.* Langmuir, 1998. **14**(22): p. 6341-6343.
31. Dixit, S.S., et al., *Light-driven formation and rupture of droplet bilayers.* Langmuir, 2010. **26**(9): p. 6193-200.
32. Gross, L.C.M., et al., *Determining Membrane Capacitance by Dynamic Control of Droplet Interface Bilayer Area.* Langmuir, 2011. **27**(23): p. 14335-14342.
33. Taylor, G.J., et al., *Direct in situ measurement of specific capacitance, monolayer tension, and bilayer tension in a droplet interface bilayer.* Soft Matter, 2015. **11**(38): p. 7592-7605.

34. Hwang, W.L., et al., *Asymmetric Droplet Interface Bilayers.* J. Am. Chem. Soc., 2008. **130**: p. 5878–5879.
35. Sarles, S.A. and D.J. Leo, *Regulated Attachment Method for Reconstituting Lipid Bilayers of Prescribed Size within Flexible Substrates.* Analytical Chemistry, 2010. **82**(3): p. 959–966.
36. Sarles, S.A., J.D.W. Madden, and D.J. Leo, *Hair cell inspired mechanotransduction with a gel-supported, artificial lipid membrane.* Soft Matter, 2011. **7**(10): p. 4644.
37. Bayley, H. and P.S. Cremer, *Stochastic sensors inspired by biology.* Nature, 2001. **413**: p. 226-230.
38. Sackmann, E., *Supported Membranes: Scientific and Practical Applications.* Science, 1996. **271**: p. 43-48.
39. Sundaresan, V.B., et al., *Biological transport processes for microhydraulic actuation.* Sensors and Actuators B: Chemical, 2007. **123**(2): p. 685-695.
40. Xu, J., T.K. Vanderlick, and D.A. LaVan, *Energy Conversion in Protocells with Natural Nanoconductors.* International Journal of Photoenergy, 2012. **2012**: p. 1-10.
41. Xu, J., F.J. Sigworth, and D.A. LaVan, *Synthetic protocells to mimic and test cell function.* Adv Mater, 2010. **22**(1): p. 120-7.
42. Xia, F. and L. Jiang, *Bio-Inspired, Smart, Multiscale Interfacial Materials.* Advanced Materials, 2008. **20**(15): p. 2842-2858.
43. McConney, M.E., et al., *Bioinspired Material Approaches to Sensing.* Advanced Functional Materials, 2009. **19**(16): p. 2527-2544.
44. Hirano-Iwata, A., et al., *Stable Lipid Bilayers Based on Micro- and Nano-Fabrication.* Analytical Sciences, 2012. **28**: p. 1049-1057.
45. Reimhult, E. and K. Kumar, *Membrane biosensor platforms using nano- and microporous supports.* Trends Biotechnol, 2008. **26**(2): p. 82-9.
46. Sarles, S.A. and D.J. Leo, *Membrane-based biomolecular smart materials.* Smart Materials and Structures, 2011. **20**(9): p. 094018.
47. Sarles, S.A. and D.J. Leo, *Physical encapsulation of droplet interface bilayers for durable, portable biomolecular networks.* Lab Chip, 2010. **10**(6): p. 710-7.
48. Poulos, J.L., et al., *Electrowetting on dielectric-based microfluidics for integrated lipid bilayer formation and measurement.* Applied Physics Letters, 2009. **95**(1): p. 013706.
49. Aghdaei, S., et al., *Formation of artificial lipid bilayers using droplet dielectrophoresis.* Lab Chip, 2008. **8**(10): p. 1617-20.
50. Dixit, S.S., et al., *Light-Driven Formation and Rupture of Droplet Bilayers.* Langmuir, 2010. **26**(9): p. 6193-6200.
51. Wauer, T., et al., *Construction and Manipulation of Functional Three-Dimensional Droplet Networks.* ACS Nano, 2013. **8**(1): p. 771-779.
52. Villar, G., A.D. Graham, and H. Bayley, *A Tissue-Like Printed Material.* Science, 2013. **340**(6128): p. 48-52.

53. Sarles, S.A., *Physical encapsulation of interface bilayers*, in *Virginia Polytechnic Institute and State University*2010.
54. Seemann, R., et al., *Droplet based microfluidics.* Rep Prog Phys, 2012. **75**(1): p. 016601.
55. Teh, S.Y., et al., *Droplet microfluidics.* Lab Chip, 2008. **8**(2): p. 198-220.
56. Christopher, G.F. and S.L. Anna, *Microfluidic methods for generating continuous droplet streams.* Journal of Physics D: Applied Physics, 2007. **40**(19): p. R319-R336.
57. Bai, Y., et al., *A double droplet trap system for studying mass transport across a droplet-droplet interface.* Lab Chip, 2010. **10**(10): p. 1281-5.
58. King, P.H., et al., *Interdroplet bilayer arrays in millifluidic droplet traps from 3D-printed moulds.* Lab Chip, 2014. **14**(4): p. 722-9.
59. Zagnoni, M. and J.M. Cooper, *A microdroplet-based shift register.* Lab Chip, 2010. **10**(22): p. 3069-73.
60. Xu, X., et al., *Optimization of microfluidic microsphere-trap arrays.* Biomicrofluidics, 2013. **7**(1): p. 14112.
61. Hwang, W.L., et al., *Electrical Behavior of Droplet Interface Bilayer Networks- Experimental Analysis and Modeling.* J. Am. Chem. Soc., 2007. **129**: p. 11854-11864.
62. Nguyen, M.-A. and S.A. Sarles, *Micro-Encapsultation and Tuning of Biomolecular Unit Cell Networks* in *ASME 2014 Smart Materials, Adaptive Structures and Intelligent Systems*2014: Newport, RI.
63. Nisisako, T., S.A. Portonovo, and J.J. Schmidt, *Microfluidic passive permeability assay using nanoliter droplet interface lipid bilayers.* Analyst, 2013. **138**(22): p. 6793-800.
64. Carreras, P., et al., *A microfluidic platform for size-dependent generation of droplet interface bilayer networks on rails.* Biomicrofluidics, 2015. **9**(6): p. 064121.
65. Wauer, T., et al., *Construction and Manipulation of Functional Three-Dimensional Droplet Networks.* ACS Nano, 2014. **8**: p. 771-779.
66. Stanley, C.E., et al., *A microfluidic approach for high-throughput droplet interface bilayer (DIB) formation.* Chem Commun (Camb), 2010. **46**(10): p. 1620-2.
67. Elani, Y., et al., *Novel technologies for the formation of 2-D and 3-D droplet interface bilayer networks.* Lab Chip, 2012. **12**(18): p. 3514-20.
68. Sarles, S.A. and D.J. Leo, *Tailored Current--Voltage Relationships of Droplet-Interface Bilayers Using Biomolecules and External Feedback Control.* Journal of Intelligent Material Systems and Structures, 2009. **20**(10): p. 1233-1247.
69. Villar, G., A.J. Heron, and H. Bayley, *Formation of droplet networks that function in aqueous environments.* Nature Nanotechnology, 2011. **6**: p. 803-808.

70. Czekalska, M.A., et al., *A droplet microfluidic system for sequential generation of lipid bilayers and transmembrane electrical recordings.* Lab Chip, 2015. **15**(2): p. 541-8.
71. Devaux, P.F. and R. Morris, *Transmembrane Asymmetry and Lateral Domains in Biological Membranes.* Traffic, 2004. **5**: p. 241-246.
72. Oakland, C.s.H.C. *The red cell membrane bilayer*. Available from: http://www.rbclab.com/Pages/500/520/520.html.
73. Marquardt, D., B. Geier, and G. Pabst, *Asymmetric lipid membranes: towards more realistic model systems.* Membranes (Basel), 2015. **5**(2): p. 180-96.
74. John, K., et al., *Transbilayer movement of phospholipids at the main phase transition of lipid membranes: implications for rapid flip-flop in biological membranes.* Biophysical Journal, 2002. **83**(6): p. 3315-3323.
75. Alvarez, O. and R. Latorre, *Voltage-dependent capacitance in lipid bilayers made from monolayers.* Biophysical Journal, 1978. **21**(1): p. 1-17.
76. Schoch, P., D.F. Sargent, and R. Schwyzer, *Capacitance and conductance as tools for the measurement of asymmetric surface potentials and energy barriers of lipid bilayer membranes.* The Journal of Membrane Biology, 1979. **46**(1): p. 71-89.
77. Cherny, V.V., V.S. Sokolov, and I.G. Abidor, *Determination of surface charge of bilayer lipid membranes.* Journal of Electroanalytical Chemistry and Interfacial Electrochemistry, 1980. **116**: p. 413-420.
78. Toyama, S., A. Nakamura, and F. Toda, *Measurement of voltage dependence of capacitance of planar bilayer lipid membrane with a patch clamp amplifier.* Biophysical Journal, 1991. **59**(4): p. 939-944.
79. Gawrisch, K., et al., *Membrane dipole potentials, hydration forces, and the ordering of water at membrane surfaces.* Biophysical Journal, 1992. **61**(5): p. 1213-1223.
80. Freeman, E.C., et al., *The mechanoelectrical response of droplet interface bilayer membranes.* Soft Matter, 2016. **12**: p. 3021-3021.
81. Hall, J.E., *Voltage-dependent lipid flip-flop induced by alamethicin.* Biophysical Journal, 1981. **33**(3): p. 373-381.
82. Hall, J.E. and M.D. Cahalan, *Calcium-induced inactivation of alamethicin in asymmetric lipid bilayers.* The Journal of General Physiology, 1982. **79**(3): p. 387-409.
83. Vodyanoy, I., J.E. Hall, and T.M. Balasubramanian, *Alamethicin-induced current-voltage curve asymmetry in lipid bilayers.* Biophysical Journal, 1983. **42**: p. 71-82.
84. Usai, C., et al., *Capacitance—voltage relationship in phospholipid bilayers containing gangliosides.* FEBS Letters, 1983. **153**(2): p. 315-319.
85. Zhang, Z., et al., *Engineered Asymmetric Heterogeneous Membrane: A Concentration-Gradient-Driven Energy Harvesting Device.* J Am Chem Soc, 2015. **137**(46): p. 14765-72.

86. Zhang, H., et al., *Bioinspired artificial single ion pump.* J Am Chem Soc, 2013. **135**(43): p. 16102-10.
87. Ko, J.-M., et al., *Tobacco protoplast culture in a polydimethylsiloxane-based microfluidic channel.* Protoplasma, 2006. **227**(2-4): p. 237-240.
88. Wu, H., et al., *Culture and chemical-induced fusion of tobacco mesophyll protoplasts in a microfluidic device.* Microfluidics and Nanofluidics, 2011. **10**(4): p. 867-876.
89. Sun, G., et al., *Dextran hydrogel scaffolds enhance angiogenic responses and promote complete skin regeneration during burn wound healing.* Proceedings of the National Academy of Sciences, 2011.
90. Abel, S. and A. Theologis, *Transient transformation of Arabidopsis leaf protoplasts: a versatile experimental system to study gene expression.* The Plant Journal, 1994. **5**(3): p. 421-427.
91. An, G., *High Efficiency Transformation of Cultured Tobacco Cells.* Plant Physiology, 1985. **79**(2): p. 568-570.
92. Burris, K.P., et al., *Development of a rapid, low-cost protoplast transfection system for switchgrass (Panicum virgatum L.).* Plant cell reports, 2016. **35**(3): p. 693-704.
93. Sheen, J., *Signal transduction in maize and Arabidopsis mesophyll protoplasts.* Plant Physiology, 2001. **127**(4): p. 1466-1475.
94. McDonald, J.C. and G.M. Whitesides, *Poly(dimethylsiloxane) as a Material for Fabricating Microfluidic Devices.* Accounts of Chemical Research, 2002. **35**(7): p. 491-499.
95. Sarles, S.A. and D.J. Leo, *Physical encapsulation of droplet interface bilayers for durable, portable biomolecular networks.* Lab on a Chip, 2010. **10**(6): p. 710-717.
96. Aghdaei, S., et al., *Formation of artificial lipid bilayers using droplet dielectrophoresis.* Lab on a Chip, 2008. **8**(10): p. 1617-1620.
97. Poulos, J.L., et al., *Electrowetting on dielectric-based microfluidics for integrated lipid bilayer formation and measurement.* Applied Physics Letters, 2009. **95**(1): p. 013706-3.
98. Brahmbhatt, K., et al. *Magnetically Responsive Droplet Interface Bilayer Networks*. in *ASME 2015 Conference on Smart Materials, Adaptive Structures and Intelligent Systems*. 2015. American Society of Mechanical Engineers.
99. Gross, L.C.M., O.K. Castell, and M.I. Wallace, *Dynamic and Reversible Control of 2D Membrane Protein Concentration in a Droplet Interface Bilayer.* Nano Letters, 2011. **11**(8): p. 3324-3328.
100. Sarles, S.A. and D.J. Leo, *Regulated Attachment Method for Reconstituting Lipid Bilayers of Prescribed Size within Flexible Substrates.* Analytical Chemistry, 2010. **82**(3): p. 959-966.
101. Bithi, S.S. and S.A. Vanapalli, *Behavior of a train of droplets in a fluidic network with hydrodynamic traps.* Biomicrofluidics, 2010. **4**(4): p. 44110.

102. Labrot, V., et al., *Extracting the hydrodynamic resistance of droplets from their behavior in microchannel networks.* Biomicrofluidics, 2009. **3**(1): p. 12804.
103. Tan, W.H. and S. Takeuchi, *A trap-and-release integrated microfluidic system for dynamic microarray applications.* Proc Natl Acad Sci U S A, 2007. **104**(4): p. 1146-51.
104. Teshima, T., et al., *A dynamic microarray device for paired bead-based analysis.* Lab Chip, 2010. **10**: p. 2443-2448.
105. Czekalska, M.A., et al., *A droplet microfluidic system for sequential generation of lipid bilayers and transmembrane electrical recordings.* Lab on a Chip, 2015. **15**(2): p. 541-548.
106. Bayley, H., et al., *Droplet interface bilayers.* Molecular BioSystems, 2008. **4**(12): p. 1191-1208.
107. Taylor, G.J. and S.A. Sarles, *Heating-Enabled Formation of Droplet Interface Bilayers Using Escherichia coli Total Lipid Extract.* Langmuir, 2015. **31**(1): p. 325-337.
108. Fertig, N., R.H. Blick, and J.C. Behrends, *Whole cell patch clamp recording performed on a planar glass chip.* Biophysical journal, 2002. **82**(6): p. 3056-3062.
109. Fertig, N., et al., *Activity of single ion channel proteins detected with a planar microstructure.* Applied Physics Letters, 2002. **81**(25): p. 4865-4867.
110. Brüggemann, A., et al., *Microchip technology for automated and parallel patch−clamp recording.* small, 2006. **2**(7): p. 840-846.
111. Le Pioufle, B., et al., *Lipid Bilayer Microarray for Parallel Recording of Transmembrane Ion Currents.* Analytical Chemistry, 2008. **80**(1): p. 328-332.
112. Zagnoni, M., M.E. Sandison, and H. Morgan, *Microfluidic array platform for simultaneous lipid bilayer membrane formation.* Biosensors and Bioelectronics, 2009. **24**(5): p. 1235-1240.
113. Hirano-Iwata, A., et al., *Lipid bilayer array for simultaneous recording of ion channel activities.* Applied Physics Letters, 2012. **101**(2): p. 023702.
114. Saha, S.C., et al., *Scalable micro-cavity bilayer lipid membrane arrays for parallel ion channel recording.* Sensors and Actuators B: Chemical, 2014. **199**: p. 76-82.
115. Saha, S.C., et al., *Characterization of the Prokaryotic Sodium Channel Na_vSp Pore with a Microfluidic Bilayer Platform.* PLoS ONE, 2015. **10**(7): p. e0131286.
116. Baaken, G., et al., *Nanopore-Based Single-Molecule Mass Spectrometry on a Lipid Membrane Microarray.* ACS Nano, 2011. **5**(10): p. 8080-8088.
117. Shim, J.S., et al., *Formation of lipid bilayers inside microfluidic channel array for monitoring membrane-embedded nanopores of phi29 DNA packaging nanomotor.* Biomedical Microdevices, 2012. **14**(5): p. 921-928.

118. Kawano, R., et al., *Automated Parallel Recordings of Topologically Identified Single Ion Channels.* Scientific Reports, 2013. **3**: p. 1995.
119. Tsuji, Y., et al. *Split-and-contact device to form planar lipid bilayers*. in *Micro Electro Mechanical Systems (MEMS), 2013 IEEE 26th International Conference on*. 2013.
120. Tsuji, Y., et al., *Droplet split-and-contact method for high-throughput transmembrane electrical recording.* Anal Chem, 2013. **85**(22): p. 10913-9.
121. Mruetusatorn, P., et al., *Dynamic morphologies of microscale droplet interface bilayers.* Soft Matter, 2014. **10**(15): p. 2530-2538.
122. Boreyko, J.B., et al., *Evaporation-Induced Buckling and Fission of Microscale Droplet Interface Bilayers.* Journal of the American Chemical Society, 2013. **135**(15): p. 5545-5548.
123. Montal, M. and P. Mueller, *Formation of Bimolecular Membranes from Lipid Monolayers and a Study of Their Electrical Properties.* Proceedings of the National Academy of Sciences, 1972. **69**(12): p. 3561-3566.
124. Tamaddoni, N., et al., *Reversible, voltage-activated formation of biomimetic membranes between triblock copolymer-coated aqueous droplets in good solvents.* Soft Matter, 2016. **12**(23): p. 5096-5109.
125. Punnamaraju, S. and A.J. Steckl, *Voltage control of droplet interface bilayer lipid membrane dimensions.* Langmuir, 2011. **27**(2): p. 618-26.
126. White, S.H., *Formation of "Solvent-free" Black Lipid Bilayer Membranes from Glyceryl Monooleate Dispersed in Squalene.* Biophysical Journal, 1978. **23**: p. 337-347.
127. Gordon, L.G. and D.A. Haydon, *Kinetics and stability of alamethicin conducting channels in lipid bilayers.* Biochimica et biophysica acta, 1976. **436**(3): p. 541-556.
128. Boreyko, J.B., et al., *Air-stable droplet interface bilayers on oil-infused surfaces.* Proceedings of the National Academy of Sciences, 2014. **111**(21): p. 7588–7593.
129. Taylor, G.J. and S.A. Sarles, *Heating-enabled formation of droplet interface bilayers using Escherichia coli total lipid extract.* Langmuir, 2015. **31**(1): p. 325-37.
130. Hwang, W.L., et al., *Asymmetric Droplet Interface Bilayers.* J. Am. Chem. Soc., 2008. **130**(18): p. 5878-5879.
131. Nisisako, T., S.A. Portonovo, and J.J. Schmidt, *Microfluidic passive permeability assay using nanoliter droplet interface lipid bilayers.* Analyst, 2013. **138**(22): p. 6793-6800.
132. Fischer, A., et al., *Ultrasensitive detection of protein translocated through toxin pores in droplet-interface bilayers.* Proceedings of the National Academy of Sciences, 2011. **108**(40): p. 16577-16581.
133. Michalak, Z., et al., *Tunable crystallization via osmosis-driven transport across a droplet interface bilayer.* CrystEngComm, 2012. **14**(23): p. 7865-7868.

134. Michalak, Z., et al., *Effect of Monoglyceride Structure and Cholesterol Content on Water Permeability of the Droplet Bilayer.* Langmuir, 2013. **29**(51): p. 15919-15925.
135. Zheng, B., J.D. Tice, and R.F. Ismagilov, *Formation of Droplets of Alternating Composition in Microfluidic Channels and Applications to Indexing of Concentrations in Droplet-Based Assays.* Anal Chem, 2004. **76**: p. 4977-4982.
136. Nguyen, M.-A., et al., *Hydrodynamic trapping for rapid assembly and in situ electrical characterization of droplet interface bilayer arrays.* Lab Chip, 2016. **16**: p. 3576-3588.
137. Venkatesan, G.A., et al., *Adsorption Kinetics Dictate Monolayer Self-Assembly for Both Lipid-In and Lipid-Out Approaches to Droplet Interface Bilayer Formation.* Langmuir, 2015. **31**(47): p. 12883-93.
138. Yasmann, A. and S. Sukharev, *Properties of diphytanoyl phospholipids at the air-water interface.* Langmuir, 2015. **31**(1): p. 350-7.
139. Genco, I., et al., *Electroporation in symmetric and asymmetric membranes.* Biochimica et Biophysica Acta, 1993. **1149**: p. 10-18.
140. Alvarez, O. and R. Latorre, *Voltage-dependent capacitance in lipid bilayers made from monolayers.* Biophysical Journal, 1978. **21**: p. 1-17.
141. Mosgaard, L.D., K.A. Zecchi, and T. Heimburg, *Mechano-capacitive properties of polarized membranes.* Soft Matter, 2015. **11**: p. 7899-7910.
142. Mottamal, M. and T. Lazaridis, *Voltage-dependent energetics of alamethicin monomers in the membrane.* Biophys Chem, 2006. **122**(1): p. 50-7.
143. Mereuta, L., A. Asandei, and T. Luchian, *Meet me on the other side: trans-bilayer modulation of a model voltage-gated ion channel activity by membrane electrostatics asymmetry.* PLoS One, 2011. **6**(9): p. e25276.
144. Mathew, M.K. and P. Balaram, *A helix dipole model for alamethicin and related transmembrane channels.* FEBS Letters, 1983. **157**(1): p. 1-5.
145. Dowgert, M.F. and P.L. Steponkus, *Behavior of the Plasma Membrane of Isolated Protoplasts during a Freeze-Thaw Cycle.* Plant Physiology, 1984. **75**(4): p. 1139-1151.
146. ibidi. *Live/dead staining with FDA and PI*. Available from: http://ibidi.com/fileadmin/support/application_notes/AN33_Live_Dead_staining_with_FDA_and_PI.pdf.

APPENDIX

A1. Derivation of network models for trap arrays

Figure A1 shows an electrical circuit model for a 3-trap Model 1 array, which will be used to demonstrate the process for developing a system of equations as given in Chapter 3.

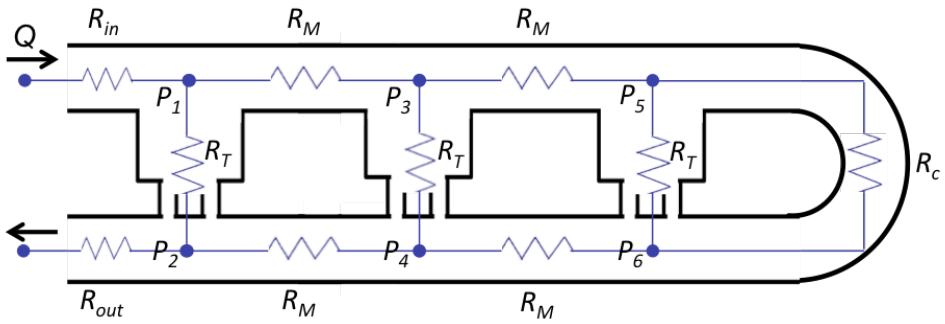

Figure A1: Electrical circuit layout of a three-trap, Model 1 array with parallel traps and a return channel. Q is the total input fluid flow rate, R_i is resistance of the i^{th} channel section, and P_i is the absolute pressure at the i^{th} node.

Using Kirchoff's Current Law (KCL) for fluid flow at each channel intersection, a matrix of equations is developed to describe the relationship between absolute node pressure, channel resistances, and input fluid flow rate. For example, applying KCL at nodes 1 and 2 yield:

$$\frac{P_1 - P_2}{R_T} + \frac{P_1 - P_3}{R_M} = Q$$

$$\frac{P_1 - P_2}{R_T} + \frac{P_4 - P_2}{R_M} - \frac{P_2}{R_{Out}} = 0$$

Following the same procedure for the remaining 4 nodes within this 3-trap array yields a total of 6 linear equations in terms of the 6 unknown pressures at all nodes. These equations can be rewritten in matrix form as follows:

$$\begin{bmatrix} \frac{1}{R_T}+\frac{1}{R_M} & \frac{-1}{R_T} & \frac{-1}{R_M} & 0 & 0 & 0 \\ \frac{-1}{R_T} & \frac{1}{R_T}+\frac{1}{R_M}+\frac{1}{R_{Out}} & 0 & \frac{-1}{R_M} & 0 & 0 \\ \frac{-1}{R_M} & 0 & \frac{1}{R_T}+\frac{2}{R_M} & \frac{-1}{R_T} & \frac{-1}{R_M} & 0 \\ 0 & \frac{-1}{R_M} & \frac{-1}{R_T} & \frac{1}{R_T}+\frac{2}{R_M} & 0 & \frac{-1}{R_M} \\ 0 & 0 & \frac{-1}{R_M} & 0 & \frac{1}{R_T}+\frac{1}{R_M}+\frac{1}{R_C} & \frac{-1}{R_T}-\frac{1}{R_C} \\ 0 & 0 & 0 & \frac{-1}{R_M} & \frac{-1}{R_T}-\frac{1}{R_C} & \frac{1}{R_T}+\frac{1}{R_M}+\frac{1}{R_C} \end{bmatrix}.$$

The same KCL procedure is also applied for 3-trap arrays in the form of both Model 2 and Model 3 as shown in Figure 2B,C, respectively. For Model 2, this process yields are a total of 7 linear equations as written in the following matrix form:

$$\begin{bmatrix} \frac{1}{R_T}+\frac{1}{R_M} & \frac{-1}{R_T} & \frac{-1}{R_M} & 0 & 0 & 0 & 0 \\ \frac{-1}{R_T} & \frac{1}{R_T}+\frac{1}{R_M} & 0 & \frac{-1}{R_M} & 0 & 0 & 0 \\ \frac{-1}{R_M} & 0 & \frac{1}{R_T}+\frac{2}{R_M} & \frac{-1}{R_T} & \frac{-1}{R_M} & 0 & 0 \\ 0 & \frac{-1}{R_M} & \frac{-1}{R_T} & \frac{1}{R_T}+\frac{2}{R_M} & 0 & \frac{-1}{R_M} & 0 \\ 0 & 0 & \frac{-1}{R_M} & 0 & \frac{1}{R_M}+\frac{1}{R_T}+\frac{1}{R_{E1}} & \frac{-1}{R_T} & \frac{-1}{R_{E1}} \\ 0 & 0 & 0 & \frac{-1}{R_M} & \frac{-1}{R_T} & \frac{1}{R_M}+\frac{1}{R_T}+\frac{1}{R_{E2}} & \frac{-1}{R_{E2}} \\ 0 & 0 & 0 & 0 & \frac{-1}{R_{E1}} & \frac{-1}{R_{E2}} & \frac{1}{R_{E1}}+\frac{1}{R_{E2}}+\frac{1}{R_{Out}} \end{bmatrix} \begin{Bmatrix} P_1 \\ P_2 \\ P_3 \\ P_4 \\ P_5 \\ P_6 \\ P_7 \end{Bmatrix} = \begin{Bmatrix} Q \\ 0 \\ 0 \\ 0 \\ 0 \\ 0 \\ 0 \end{Bmatrix}.$$

Finally, a 3-trap version of Model 3 with 9 pressure nodes yields a total of 9 linear equations, which can be written in the following matrix form

$$\begin{bmatrix} \frac{1}{R_M}+\frac{1}{R_T} & \frac{-1}{R_T} & \frac{-1}{R_M} & 0 & 0 & 0 & 0 & 0 & 0 \\ \frac{-1}{R_T} & \frac{1}{R_T}+\frac{1}{R_R} & \frac{-1}{R_R} & 0 & 0 & 0 & 0 & 0 & 0 \\ \frac{-1}{R_M} & \frac{-1}{R_R} & \frac{1}{R_M}+\frac{1}{R_R}+\frac{1}{R_B} & \frac{-1}{R_B} & 0 & 0 & 0 & 0 & 0 \\ 0 & 0 & \frac{-1}{R_B} & \frac{1}{R_M}+\frac{1}{R_T}+\frac{1}{R_B} & \frac{-1}{R_T} & \frac{-1}{R_M} & 0 & 0 & 0 \\ 0 & 0 & 0 & \frac{-1}{R_T} & \frac{1}{R_T}+\frac{1}{R_R} & \frac{-1}{R_R} & 0 & 0 & 0 \\ 0 & 0 & 0 & \frac{-1}{R_M} & \frac{-1}{R_R} & \frac{1}{R_M}+\frac{1}{R_R}+\frac{1}{R_B} & \frac{-1}{R_B} & 0 & 0 \\ 0 & 0 & 0 & 0 & 0 & \frac{-1}{R_B} & \frac{1}{R_M}+\frac{1}{R_T}+\frac{1}{R_B} & \frac{-1}{R_T} & \frac{-1}{R_M} \\ 0 & 0 & 0 & 0 & 0 & 0 & \frac{-1}{R_T} & \frac{1}{R_T}+\frac{1}{R_R} & \frac{-1}{R_R} \\ 0 & 0 & 0 & 0 & 0 & 0 & \frac{-1}{R_M} & \frac{-1}{R_R} & \frac{1}{R_M}+\frac{1}{R_R}+\frac{1}{R_{Out}} \end{bmatrix} \begin{Bmatrix} P_1 \\ P_2 \\ P_3 \\ P_4 \\ P_5 \\ P_6 \\ P_7 \\ P_8 \\ P_9 \end{Bmatrix} = \begin{Bmatrix} Q \\ 0 \\ 0 \\ 0 \\ 0 \\ 0 \\ 0 \\ 0 \\ 0 \end{Bmatrix}$$

.

These matrix expressions can be solved numerically in MATLAB to determine the values of absolute pressures at all nodes, which can then be used to evaluate relative flow rates in traps versus the main channel (Figure 3D) or compute the pressure drop across all traps in a filled array (Figure 3E).

A2. Droplet size based on flow rates of aqueous buffer and oil

A series of experiments varying the flow rates of the oil and the aqueous buffer was performed to determine the range of the droplet sizes the device can produce and to identify the flow rates required to generate ~100 μm diameter droplets used in the trapping experiments. Figure A2 shows the corresponding droplet diameters based on the flow rate ratio of buffer to oil. Note, the same flow rate ratios can give different sizes since different flow rates of oil and buffer can produce the same ratios.

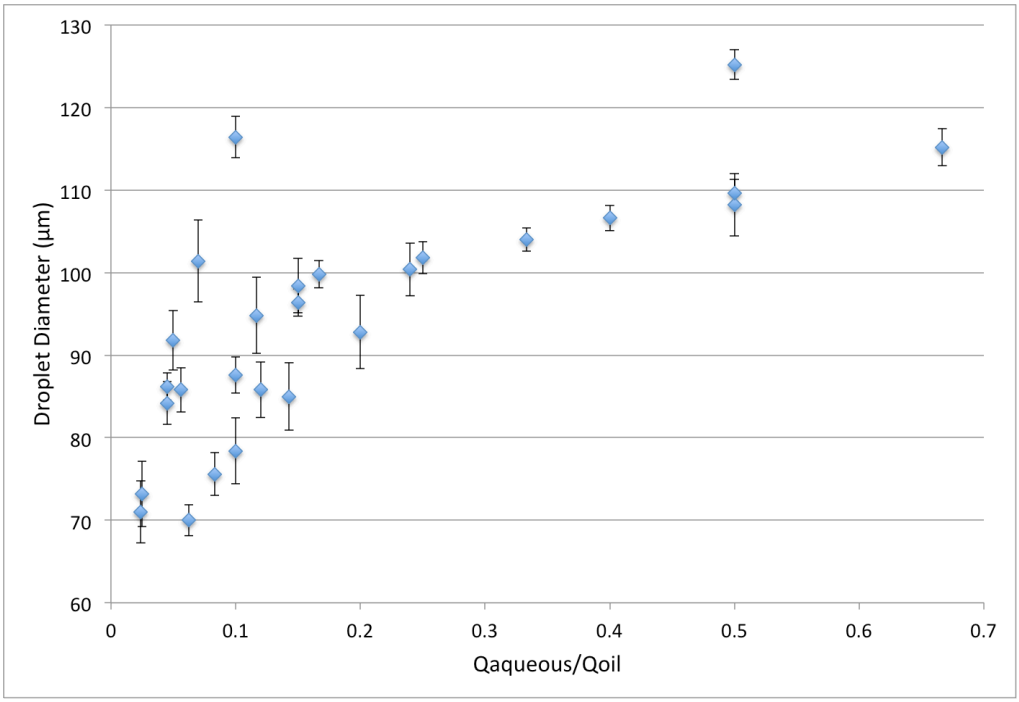

Figure A2: Average droplet diameter versus the aqueous buffer/oil flow rate ratio.

A3. Nominal capacitance and membrane resistance determined for an 8-DIB array

Raw current measurements as shown in Figure 7C is used to calculate bilayer capacitance, which is then plotted against time in Figure A3A The capacitances of all 8 pairs correspond to the growing membrane area. Furthermore, the resistivity is plotted in Figure S2B using the interface area and resistance of the membrane, which is calculated from the slope of the current at the peaks of the square-like waveform.

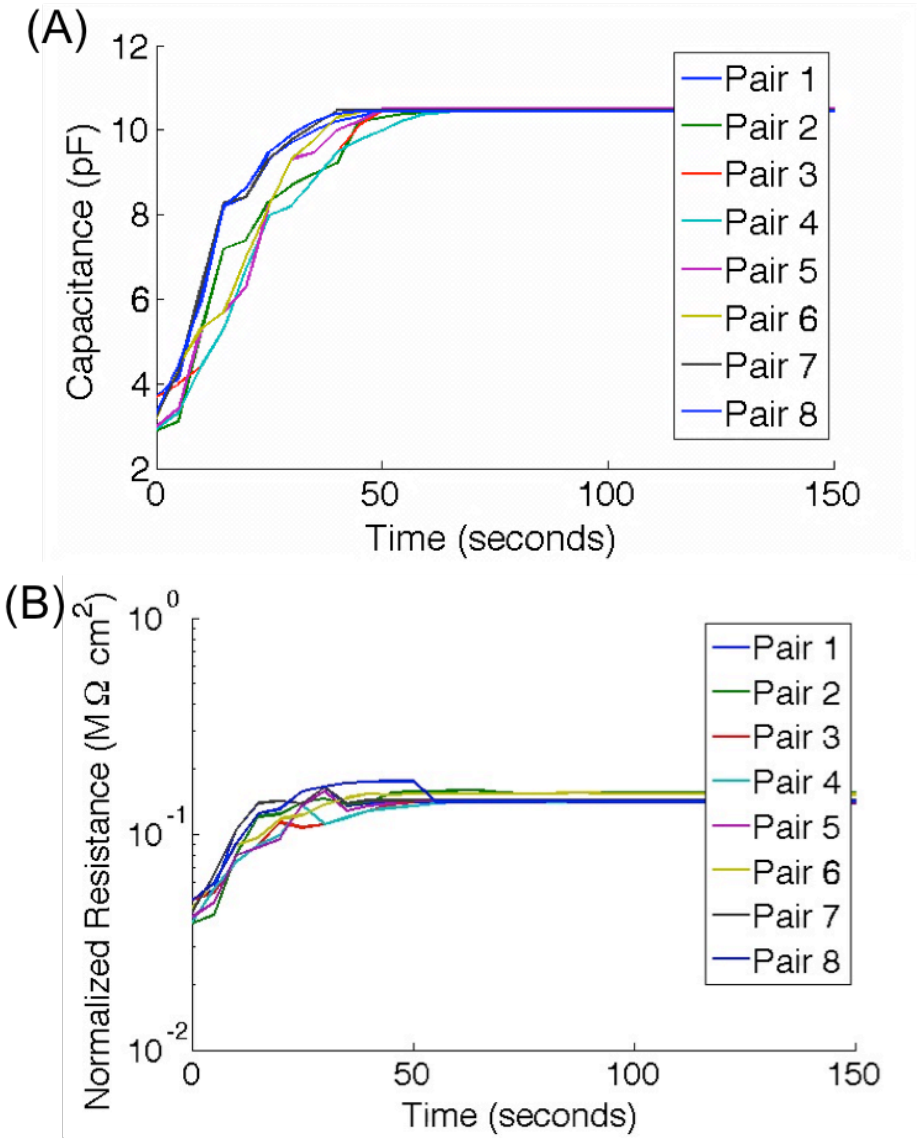

Figure A3: (A) Membrane capacitance increases upon DIB formation, corresponding to a growing membrane area, while (B) normalized resistances does not change significantly for all eight pairs of DIBs. Note start time is relative to each DIB pair.

A4. Electrical measurements from 2 additional trials

Below are tabulated results from two separate experiments using electrical measurements to simultaneously characterize a set of 8 GMO DIBs.

Table A1: Capacitance, resistance, area, specific capacitance, and normalized resistance for GMO DIBs obtained during Trial 2.

DIB #	Capacitance final (C_F) – pF	Resistance final (R_F) – GΩ	Area final (A_F) – μm^2	Specific capacitance (C_M) - $\mu F/cm^2$	Normalized resistance (R_N) - $M\Omega \cdot cm^2$
Pair 1	16.7	8.0	2173	0.769	0.17
Pair 2	16.8	8.5	2181	0.770	0.19
Pair 3	16.8	8.0	2181	0.770	0.17
Pair 4	16.7	8.1	2181	0.766	0.18
Pair 5	16.7	8.1	2173	0.769	0.18
Pair 6	16.7	8.0	2173	0.769	0.17
Pair 7	16.7	8.1	2173	0.769	0.18
Pair 8	16.7	8.1	2173	0.769	0.18
Averages	16.7±0.05	8.1±0.2	2176±4	0.769±0.001	0.18±0.004

Table A2: Capacitance, resistance, area, specific capacitance, and normalized resistance for GMO DIBs obtained during Trial 3.

DIB #	Capacitance final (C_F) – pF	Resistance final (R_F) – GΩ	Area final (A_F) – μm^2	Specific capacitance (C_M) - $\mu F/cm^2$	Normalized resistance (R_N) - $M\Omega \cdot cm^2$
Pair 1	12.8	8.1	1662	0.770	0.13
Pair 2	12.8	8.8	1662	0.770	0.15
Pair 3	13.1	8.0	1684	0.778	0.14
Pair 4	13.1	8.1	1684	0.778	0.14
Pair 5	12.8	8.1	1662	0.770	0.13
Pair 6	12.9	8.8	1669	0.773	0.15
Pair 7	13.0	8.2	1676	0.775	0.14
Pair 8	12.9	8.1	1669	0.773	0.13
Averages	12.9±0.13	8.3±0.4	1671±9	0.773±0.003	0.14±0.01

VITA

Mary-Anne K. Nguyen was born in Baton Rouge, Louisiana and is the third child out of four siblings. She received her B.S. in Biological Engineering at Louisiana State University in May 2012 and is currently set to graduate in Spring 2017 with a Ph.D. in Biomedical Engineering at University of Tennessee, Knoxville.

While at LSU, she participated in the LA-STEM scholars program. Mary-Anne did her undergraduate research in the Biological Engineering department studying photocleavable cage oligonucleotides. Throughout her undergraduate career, Mary-Anne served as a mentor through the College of Engineering and Office of Strategic Initiatives. She also is a recipient of the LSU Distinguished Communicator award.

As a graduate student, Mary-Anne's work mainly centered on the field of synthetic biology particularly the use of droplet interface bilayers and microfluidics. Her research has resulted in several conference proceedings and presentations. Also, she has published a first-author paper with two more papers in preparation.

When she is not in lab at the microscope, Mary-Anne enjoys spending her time baking, sewing, and drinking coffee.